Low-Temperature Physical Properties of Topological Semimetals

by

Yinying Zhang

A dissertation submitted in partial fulfillment
of the requirements for the degree of
Doctor of Philosophy
(Physics)
in the University of Michigan
2024

Doctoral Committee:

Professor Ctirad Uher, Chair
Professor Cagliyan Kurdak
Professor Lu Li
Professor Pierre Ferdinand Poudeu Poudeu
Professor Kai Sun

Yinying Zhang

yinyingz@umich.edu

ORCID iD: 0000-0001-9696-1348

Dedication

I dedicate this work to those I love.

Acknowledgements

First of all, I would like to express my gratitude to my academic advisor, Prof. Ctirad Uher, for taking me as his graduate student and funding my research. Prof. Uher is a very open advisor. He provided me with complete freedom to choose my doctoral projects and was always happy to support me try things I wanted. I am also thankful for his patience in carefully reviewing my manuscripts and for providing me with valuable feedback and suggestions pertaining to both physics and English writing.

For the past four years, I have been the only student in Prof. Uher's group. As a result, I am deeply grateful for the assistance of colleagues and friends in other groups. Without their support, my achievements to date would have been impossible.

I would like to express my appreciation to Dr. Kuan-Wen Chen, a postdoctoral researcher in Prof. Lu Li's group, for his invaluable support in training me to use the PPMS, which is the most important equipment for my research. Kuan-Wen has been a great mentor to me over the last three years, providing me with expert guidance on collecting reliable data from the PPMS. I also wish to thank Kuan-Wen and Prof. Li for their assistance in refining my manuscript on the $Ni_3In_2S_2$ project, which resulted in significant improvement.

I would like to express my gratitude to my collaborator, Dr. Zhongrui Li, the research faculty at the Electron Microbeam Analysis Laboratory (EMAL). Zhongrui offered computational information about the materials I studied, such as band structure, density of states, Fermi surface,

etc., which are essential to understanding the underlying physics of magnetic and transport properties of the materials.

I would like to thank my friend, Mr. Zhixiong Yin, a graduate student in Prof. Pierre Poudeu's group, for his efforts in growing $NiTe_2$ single crystals. Although those crystals were imperfect, measurements done on them provided me with valuable insights into the properties of $NiTe_2$, which was crucial in the early stages of my project.

I am thankful to collaborators, Prof. Qiang Li and Dr. Genda Gu, at the Brookhaven National Lab, for providing the $NiTe_2$ single crystal. This high-quality single crystal enabled me to continue the project and acquire the necessary data.

I would also like to thank those amazing staff members of the technical and student services teams I have met these years: Dr. Owen Neill, Roy Wentz, Dave Carter, Paul Thurmond, Heather Wolfe, Lauren Segall, Grace Johnson, Cory Steiner, Sarah Bargardi, and Tammy Kennedy.

Aside from everything physics-related, I want to thank Mr. ZhouShen. His music has continuously instilled hope and vigor within me, even in the toughest times. He is like a beacon of light during darkness or the sun on a wintery day. Mr. ZhouShen's words of encouragement inspire me to stay positive in both my professional and personal life and to prioritize self-care and self-love.

Lastly, I want to express my deepest gratitude to my parents for their unwavering commitment to my upbringing and their unconditional love and support. Their invaluable contributions have played an essential role in shaping me into the person I am today. Without them, I would be nothing.

Table of Contents

List of Tables

List of Figures

List of Abbreviations

AHE anomalous Hall effect

ARPES angle-resolved photoemission spectroscopy

BZ Brillouin zone

CPA coherent potential approximation

DOS density of states

EDS energy dispersive X-ray spectroscopy

ETO Electrical Transport Option

FC field-cooled

FFT fast Fourier transform

IS inversion symmetry

MR magnetoresistance

NLSM nodal-line semimetal

PDOS element-specific partial DOS

PPMS Physical Property Measurement System

PXRD powder X-ray diffraction

SOC spin-orbit coupling

TI topological insulator

TRS time-reversal symmetry

TSM topological semimetal

TTO Thermal Transport Option

VSM Vibrating Sample Magnetometer

XRD powder X-ray diffraction

ZFC zero-field-cooled

Abstract

In recent years, the study of topological materials has been a hot topic in condensed matter physics. These materials have attracted considerable attention due to their intriguing physical properties and potential functional applications. This thesis first reviews the background knowledge of topological semimetals and then presents investigations of the low-temperature physical properties of three different topological semimetals.

The first discussed is shandite $Co_3Sn_2S_2$, which is a Weyl semimetal. The study focuses on the effect of Fe-doping on the magnetic and transport properties of polycrystalline $Co_3Sn_2S_2$. Fe-doping suppresses the sample's magnetic order and lowers the Curie temperature. Moreover, Fe-doping results in the Kondo effect in the temperature-dependent resistivity and the skew-scattering contribution to the anomalous Hall effect. In addition, a hysteresis behavior of the low-magnetic field magnetoresistance in both pure and Fe-doped $Co_3Sn_2S_2$ is observed. At last, the Seebeck coefficient and thermal conductivity are discussed.

The next material discussed is the single crystalline $Ni_3In_2S_2$, which is also a semimetal from the shandite family like $Co_3Sn_2S_2$. $Ni_3In_2S_2$ displays an extremely large transverse magnetoresistance and a magnetic field-induced resistivity upturn behavior at low temperatures. Below 50 K, the magnetoresistance curves show a linear magnetic field dependence under high magnetic fields. Along with magnetotransport measurements, quantum oscillations and computation results indicate that it is the linearly dispersive bands that cause the high mobility and quantum linear magnetoresistance, thus leading to the extreme magnetoresistance in $Ni_3In_2S_2$.

The last presented is the study on the type-II Dirac semimetal $NiTe_2$ single crystal. $NiTe_2$ exhibits a large magnetoresistance at low temperatures, of which the value and the magnetic-field dependence are sensitive to the field strength and the angle between the applied magnetic field and the current, showing the anisotropic feature of its magnetoresistance. The quantum oscillation results reveal the small effective mass and the nontrivial Berry phase originating from the Dirac point. The temperature-dependent Lorenz number deduced from the thermal conductivity significantly deviates from the Sommerfeld value, indicating the breakdown of the Wiedemann-Franz law.

Overall, this thesis focuses on the low-temperature properties of topological semimetals, especially the analyses of transport properties, which may serve as a reference for future research on topological materials.

Chapter 1 Introduction

In the 1980s, the discovery and subsequent topological understanding of quantum integer and fractional Hall effects in high-mobility two-dimensional electron gases led to the emergence of a new research field in condensed matter physics: topological states of matter [1-4]. In the past decades, significant efforts have been dedicated to searching for, fabricating, and characterizing topological materials.

The first experimentally realized topological material was a topological insulator (TI), the $Bi_{1-x}Sb_x$ alloy, characterized by strong spin-orbit coupling (SOC) gapped bulk bands and symmetry protected gapless surface states [5-8]. Soon after that, topological semimetal (TSM), which has a small density of states (DOS) induced by the valence and conduction band crossings in the three-dimensional Brillouin zone (BZ), has been predicted and realized, boarding the field of topological materials [9, 10]. Such band crossings can be related to a topological invariant, which distinguishes TSMs from other semimetals [11]. TSMs can be categorized into three groups based on the dimensionality of band crossings. The first group of TSMs are those with zero-dimensional band crossings, which are referred to as nodes or nodal points. The most studied Dirac semimetals (DSMs) and Weyl semimetals (WSMs) belong to this group, which are identified by the fourfold Dirac points and twofold Weyl points, respectively. The low-energy excitations around these points act like the Dirac and Weyl fermions in high-energy physics, offering platforms to study their characteristics, such as the chiral anomaly effect. The second group of TSMs are called topological nodal-line semimetals (NLSMs). They have band crossings that occur along one-dimensional lines in the momentum space. Such one-dimensional lines may be closed

loops inside the BZ or lines running across the BZ. The third group of TSMs are named as topological nodal-surface semimetals, which have band crossings preserved in a two-dimensional surface in the BZ [11].

TSMs exhibit tremendous intriguing physical properties. Topologically protected surface states, such as Fermi arcs, have been detected by angle-resolved photoemission spectroscopy (ARPES) [12]. The Weyl orbits induced by the Fermi arcs have been observed by quantum oscillation measurements [13]. The chiral anomaly effect of Weyl and Dirac fermions is manifested by the negative longitudinal magnetoresistance and/or the planar Hall effect [14, 15]. The diverging Berry curvatures near the Weyl nodes result in a large intrinsic anomalous Hall effect (AHE) and an anomalous Nernst effect [16, 17]. The linear dispersions and low-energy excitations around band crossings lead to high carrier mobility and, thus, large positive magnetoresistance (MR) [18]. Furthermore, thinning three-dimensional TSMs into two-dimensional forms, quantum spin and anomalous Hall effects may be achieved [19, 20]. The studies on TSMs not only advance fundamental science but also pave the way for the development of novel electronic and energy-harvesting devices. Consequently, there has been a growing interest among researchers to dedicate their efforts to this captivating field.

This thesis presents investigations of the physical properties of topological semimetals at low temperatures. It is structured as follows. Chapter 2 provides a brief overview of DSMs, WSMs, and NLSMs. Chapter 3 summarizes the background knowledge of transport properties, including magnetoresistance, the Hall effect, and quantum oscillations. In Chapter 4, I discuss the effects of Fe-doping on the magnetic and transport properties of polycrystalline WSM $Co_3Sn_2S_2$. Chapter 5 reports on the extremely large low-temperature transverse MR in a $Ni_3In_2S_2$ single crystal, which is an isostructural compound of $Co_3Sn_2S_2$, and explains the origin of such a large MR. Chapter 6

displays the electric and thermal transport properties and quantum oscillation results of single crystalline type-II DSM $NiTe_2$. Finally, in Chapter 7, I present a summary of this thesis and an outlook for future work.

Chapter 2 Three-Dimensional Topological Semimetals

In this chapter, I will briefly overview the background of topological semimetals, focusing on the Dirac and Weyl equations. Additionally, I will introduce three types of topological semimetals known as Dirac semimetals, Weyl semimetals, and nodal-line semimetals, along with their distinct electronic band structures.

2.1 Dirac and Weyl Equations

In the field of solid-state physics, the well-known Schrödinger equation provides a successful description of nearly free quasiparticles. The low-energy excitations described by the Hamiltonian $H = \boldsymbol{p}^2/2m^*$, where $\boldsymbol{p}$ represents the momentum and m^* denotes the effective mass, are referred to as Schrödinger fermions. However, the Schrödinger equation is not applicable in all cases. For instance, it has been found that quasiparticles in graphene can be described by the relativistic Dirac equation rather than the Schrödinger equation [21].

In solids, the Dirac Hamiltonian takes the form of

$$H_D = v_F \alpha \cdot \boldsymbol{k} + \beta m v_F^2 = \begin{pmatrix} v_F \boldsymbol{\sigma} \cdot \boldsymbol{k} & m v_F^2 \\ m v_F^2 & -v_F \boldsymbol{\sigma} \cdot \boldsymbol{k} \end{pmatrix} \tag{2.1}$$

where $\boldsymbol{k} = (k_x, k_y, k_z)$ is the momentum, $\boldsymbol{\sigma} = (\sigma_x, \sigma_y, \sigma_z)$ is the vector of 2×2 Pauli matrices, m is the effective mass, and v_F is the Fermi velocity. The Dirac fermions follow the energy-momentum relation:$E_\pm = \pm\sqrt{m^2 v_F^4 + k^2 v_F^2}$, with a band gap of $\Delta = 2mv_F^2$ at $k = 0$, as shown in Figure 2.1 [11]. In the case of vanishing effective mass, the Dirac Hamiltonian becomes diagonal, i.e.,

$$H_D^{m=0} = \begin{pmatrix} v_F\boldsymbol{\sigma}\cdot\boldsymbol{k} & 0 \\ 0 & -v_F\boldsymbol{\sigma}\cdot\boldsymbol{k} \end{pmatrix} \tag{2.2}$$

Consequently, a fourfold-degenerate Dirac point with linear dispersions in all directions appears at $k = 0$ instead of the gap in the massive case. The low-energy excitations near the Dirac point are known as massless Dirac fermions, and materials that have such Dirac points near the Fermi level (E_F) are referred to as DSMs.

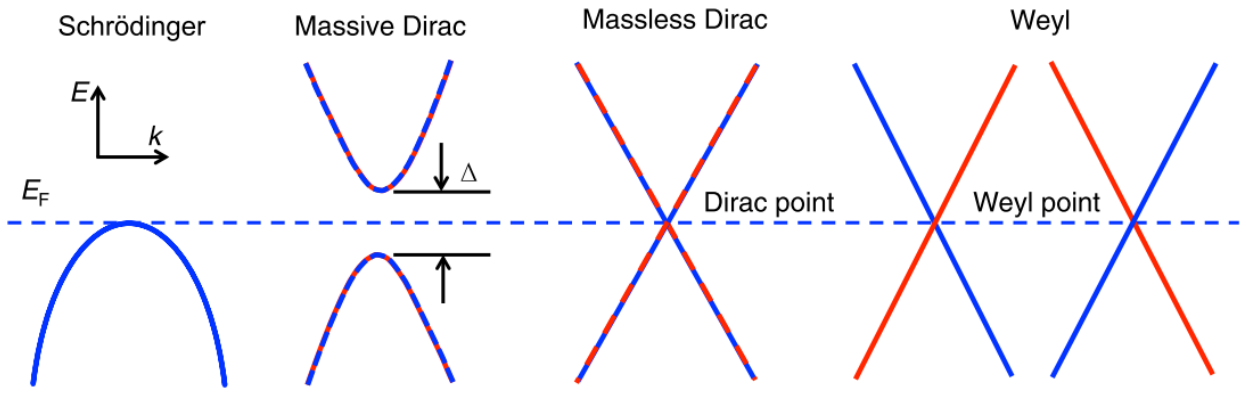

Figure 2.1: Schematic plots of the band structures of Schrödinger, massive Dirac, massless Dirac, and Weyl fermions. The curves with mixed and uniform colors represent doubly degenerate and nondegenerate bands, respectively. Taken from reference [11] with permission from the American Physical Society.

When $m = 0$, the diagonal H_D can be expressed in a simpler form:

$$H_{\pm} = \pm v_F\boldsymbol{\sigma}\cdot\boldsymbol{k} \tag{2.3}$$

which is called the Weyl Hamiltonian, and $\pm$ represents different chirality of the massless Weyl fermions. Both H_+ and H_- have two eigenvalues, i.e., $E = \pm v_F|k|$. Therefore, the spectrum of the Weyl Hamiltonian is comprised of two linear and non-degenerate bands crossing at a twofold-degenerate point at $k = 0$, and this point is denoted as the Weyl point. A fourfold-degenerate Dirac point can thus be regarded as a pair of two Weyl points with opposite chirality. The low-energy excitations around the Weyl point are known as massless Weyl fermions, and materials that have such Weyl points near the Fermi level (E_F) are called WSMs [11].

For systems strictly obey forementioned Dirac/Weyl equations, they have isotropic Dirac/Weyl cones with linearly dispersed bands in all momentum directions, and the low-energy excitations around Dirac/Weyl points are counterparts of relativistic Dirac/Weyl fermions in high-energy physics, which respect the Lorentz invariance. However, in solid-state physics, band crossings in crystals are restricted by the symmetries of 230 space groups, not the Lorentz invariance. Therefore, other types of band crossings are also feasible, in addition to the isotropic Dirac and Weyl cones.

Take the Weyl Hamiltonian as the example. If we add a tilting term to the Weyl Hamiltonian, it takes the form of

$$H_{\pm} = \pm v_F \boldsymbol{\sigma} \cdot \boldsymbol{k} + \boldsymbol{t} \cdot \boldsymbol{k} \boldsymbol{I_2} \tag{2.4}$$

where $\boldsymbol{t}$ is the tilt vector and $\boldsymbol{I_2}$ is the 2×2 identity matrix. Consider only the right-handed fermion and suppose that $\boldsymbol{t}$ is along the direction of k_z. Then, the Hamiltonian can be written as:

$$H = v_F \begin{pmatrix} k_z(1 + t/v_F) & k_x - ik_y \\ k_x + ik_y & -k_z(1 - t/v_F) \end{pmatrix} \tag{2.5}$$

The corresponding energy spectra are:

$$\varepsilon_{\pm}(k) = \pm v_F(k_x + k_y) \pm (v_F \pm t)k_z \tag{2.6}$$

These two bands cross at the Weyl point $k = 0$. If $v_F > t$, these two linear bands always have velocities of opposite sign along all *k* directions, and $\varepsilon(k) = 0$ occurs only at the Weyl point $k = 0$. The Weyl cone is slightly tilted, and its physical properties are similar to the isotropic Weyl cone. Thus, the Weyl point of this case and the Weyl point with the isotropic Weyl cone are classified as type-I Weyl points. If $v_F < t$, these two bands have velocities of the same sign along the direction of k_z. The Weyl cone is highly tilted, resulting in a Fermi surface comprising open electron and hole pockets rather than a point. The corresponding Weyl point is denoted as a type-II Weyl point. When $v_F = t$, one of the bands has zero velocity along k_z, leading to a line-like

Fermi surface. This kind of Weyl point is called type-III Weyl point [11]. Figure 2.2 gives a schematic view of different types of Weyl points. The same concept can be applied to Dirac points.

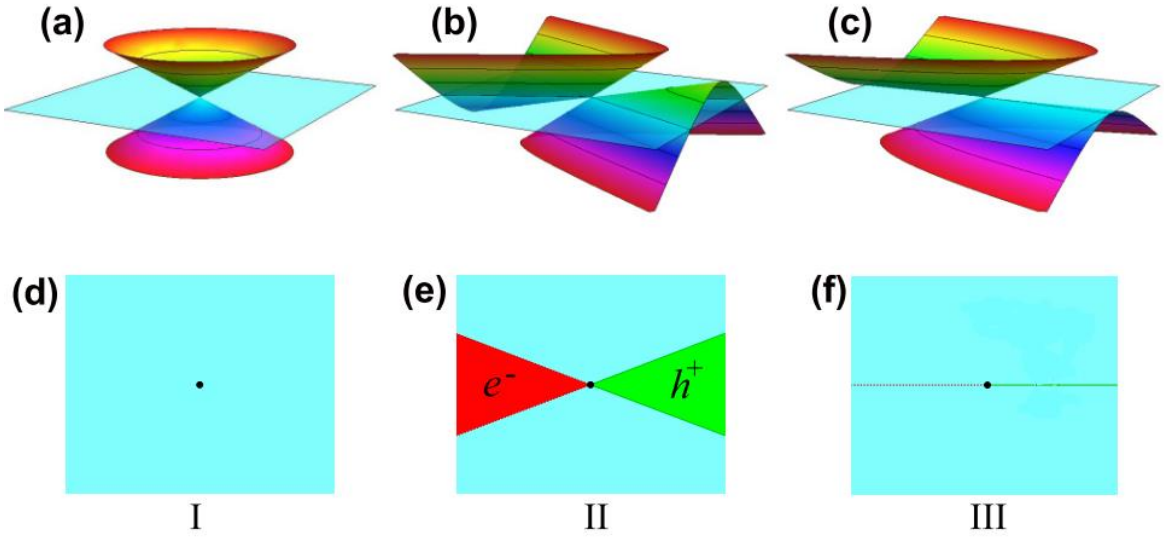

Figure 2.2: (a)(d) Type-I Dirac/Weyl point with a point-like Fermi surface. (b)(e) The type-II Dirac/Weyl point is the contact point between the electron and hole pocket. (c)(f) Type-III Dirac/Weyl point with line-like Fermi surface. The light blue plane corresponds to the Fermi level. Modified from reference [22] with permission from the American Physical Society.

2.2 Dirac Semimetal

DSMs host fourfold Dirac points resulting from two doubly degenerate bands crossing at a point near E_F. The most common mechanism to realize a DSM involves a combination of band inversion with uniaxial rotational symmetry. It is noteworthy that the first experimentally confirmed three-dimensional DSMs, namely Na_3Bi and Cd_3As_2, are associated with this mechanism. Consider Na_3Bi as an example. Figure 2.3a shows the calculated band structure of Na_3Bi with and without the inclusion of SOC. The majority of the band crossings near E_F are gapped out with SOC, except the one along the Γ-A direction (marked by the blue rectangle). This is because Na_3Bi crystallizes in space group No.194 ($P6_3/mmc$) with C_3 rotation symmetry. The

two bands that cross at the rotational axis belong to two distinct irreducible representations, making the band crossing resistant to SOC. Since Na_3Bi has both inversion symmetry (IS) and time-reversal symmetry (TRS), there are two isolated Dirac points along the Γ-A direction (see Figure 2.3b). As displayed in Figure 2.3c, near the Dirac point, the bands disperse linearly along all directions but with different Fermi velocities, resulting in a nearly isotropic cone in the $k_x^D - k_y^D$

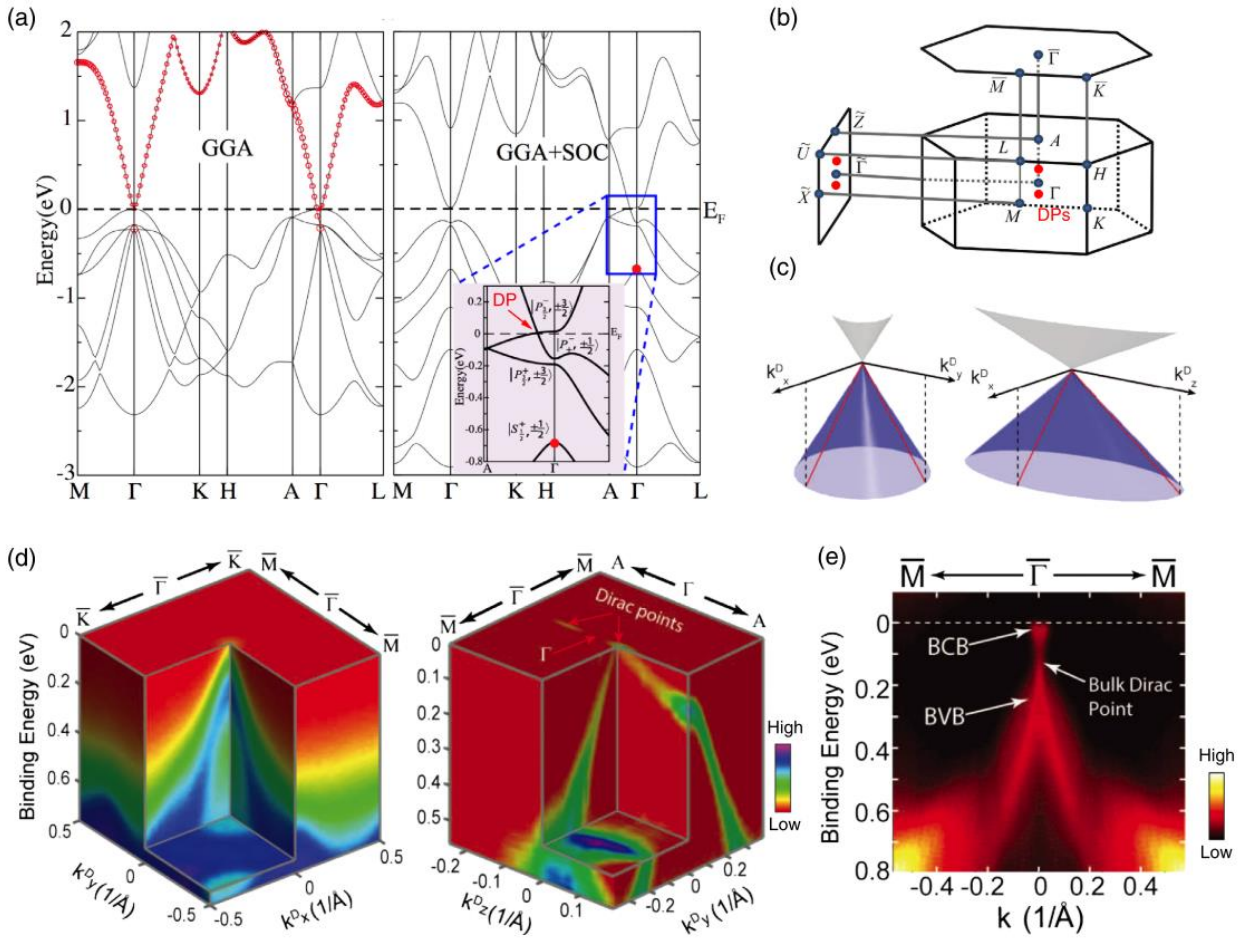

Figure 2.3: (a) Calculated band structure of Na_3Bi with and without SOC. (b) Bulk and projected (010) surface BZs of Na_3Bi.The red dots indicate the momentum location of the Dirac points. (c) Schematic band dispersions near the Dirac points in the $k_x^D - k_y^D$ and $k_x^D - k_z^D$ planes, respectively. (d) 3D ARPES intensity plots, showing the band dispersion of the bulk Dirac cone along the in-plane ($k_x^D - k_y^D$ plane) and out-of-plane ($k_y^D - k_z^D$plane) directions, respectively. (e) ARPES intensity plot shows the band dispersion of the upper Dirac cone along the $\bar{\Gamma} - \bar{M}$ direction after the *in situ* K-doping. Taken from reference [11] with permission from the American Physical Society.

plane and an anisotropic cone in the $k_x^D - k_z^D$ plane. These have been experimentally observed by ARPES (see Figure 2.3d). Furthermore, by tuning the position of E_F through the *in situ* K-doping, the Dirac point in the bulk bands has also been observed, as shown in Figure 2.3e [11, 23].

Another mechanism to realize DSMs relies on nonsymmorphic symmetries, which can give rise to fourfold Dirac points at high-symmetry points on the boundary of BZ. It is theoretically predicted that β-cristobalite BiO_2 is a promising candidate for a nonsymmorphic DSM, which has three Dirac points located on the surface of BZ [24]. However, at present, there is a dearth of experimental evidence to support this theoretical prediction.

2.3 Weyl Semimetal

WSMs have twofold Weyl points at which two non-degenerate bands cross. Breaking either IS or TRS can convert a DSM into a WSM. The Weyl points can be characterized by the Fermi surface (FS) Chern number *C*. For the Weyl point depicted by (2.3), the corresponding Chern number is

$$C^{\pm} = \frac{1}{2\pi} \oiint_{\mathrm{FS}} \boldsymbol{\Omega}_{\pm}(\boldsymbol{k}) \cdot d\boldsymbol{S} = \pm 1 \tag{2.7}$$

where $\boldsymbol{\Omega}_{\pm}(\boldsymbol{k}) = \nabla_k \times \boldsymbol{A}_{\pm}(\boldsymbol{k}) = \pm \frac{\hat{e}_k}{2k^2}$ denotes the Berry curvature. According to Equation (2.7), a Weyl point acts as a source or drain of Berry curvature in the momentum space. This means that Weyl points can be thought of as magnetic monopoles in the momentum space. To comply with the periodic BZ condition, the Berry curvature must originate from a source and terminate at a drain within the BZ. This requires that Weyl points must always appear in pairs of opposite chirality, resulting in them being topologically stable as long as they stay apart in the momentum space [11].

Because a pair of Weyl points with opposite chirality functions as a source and drain of Berry curvature, it leads to the penetration of Berry flux into all the 2D planes that exist between them. Consequently, each of these planes possesses a non-zero Chern number, which gives rise to the formation of a topological edge state. Combining all such edge states forms an unclosed energy contour, also known as the Fermi arc. The Fermi arc starts from the projection of one Weyl point, ending at the other with the opposite chirality on the surface, as shown in Figure 2.4 [11, 25]. The presence of Fermi arcs constitutes a noteworthy characteristic of WSMs.

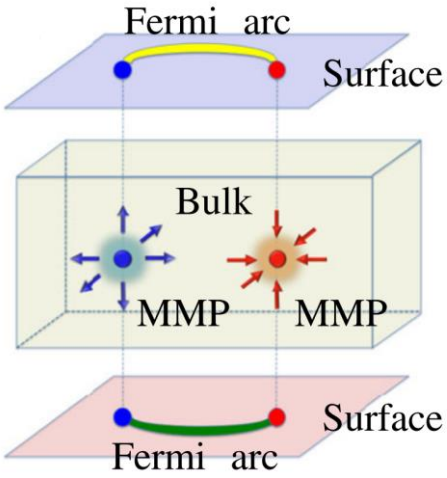

Figure 2.4: A Weyl semimetal has Fermi arcs on its surface connecting projections of two Weyl points with opposite chirality. In momentum space, the Weyl point behaves like a magnetic monopole (MMP), with its chirality corresponding to the charge of the MMP. Modified from reference [26] with permission from the American Physical Society.

Take TaAs, a transition metal monoarsenide, as an example. As shown in Figure 2.5, TaAs crystallizes in space group No.109 ($I4_1md$), having four Ta-As layers along the c-axis in a unit cell devoid of IS. TaAs is a WSM with twelve pairs of Weyl points in the BZ, each pair with monopole charges of ± 1. There are four pairs of Weyl points located at each of the $k_z = 0$ and $\pm 1.16\pi/c$ planes, where c is the lattice parameter. The calculated Fermi surface on the (001) surface of TaAs exhibits

Fermi arcs connecting projected Weyl points of opposite chirality. The ARPES experiments confirmed the existence of these Fermi arcs, and the observations demonstrate excellent agreement with the theoretical calculations [27].

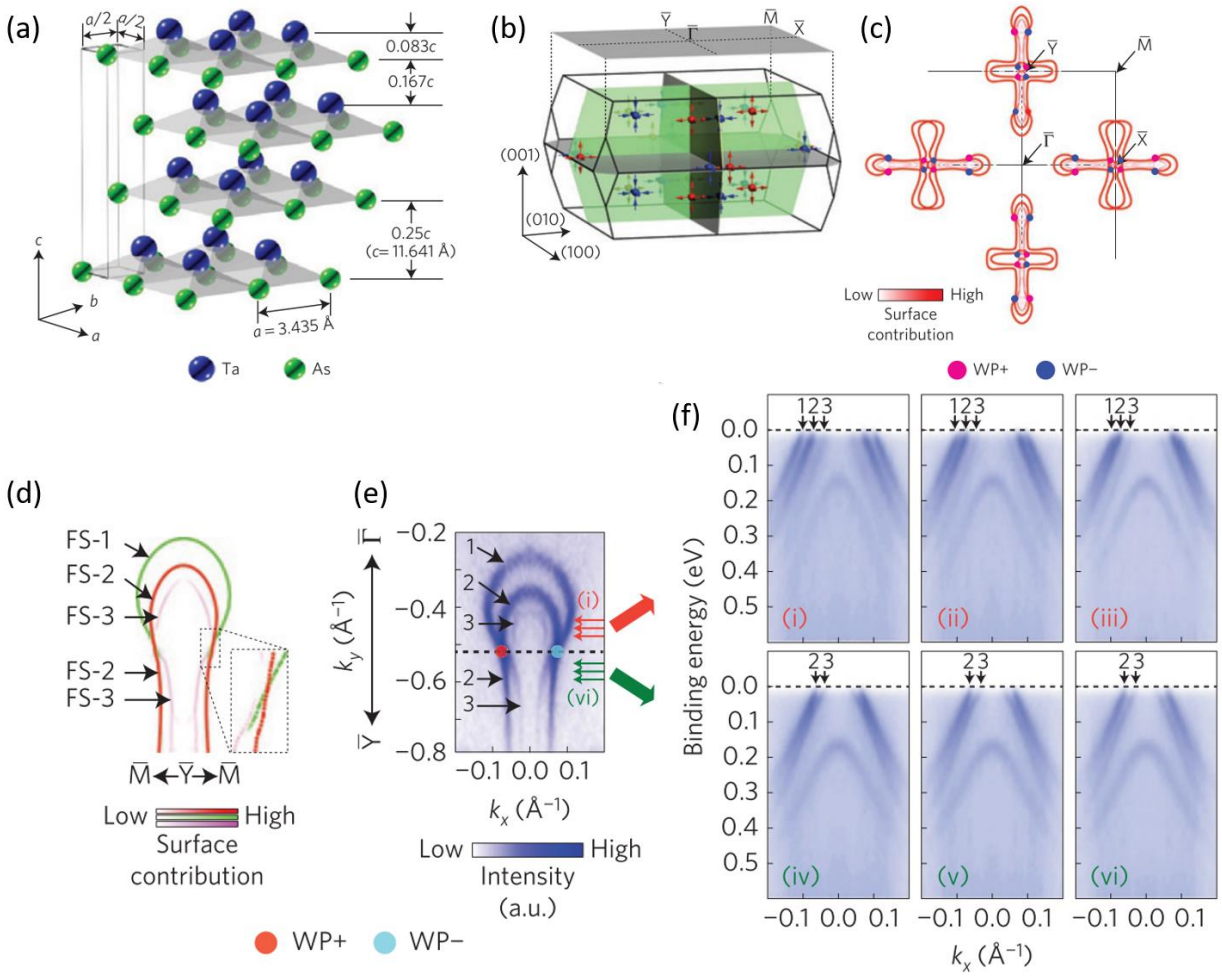

Figure 2.5: (a) Crystal structure of TaAs. (b) Schematic of the bulk and (001) surface Brillouin zones (BZs) of TaAs. Twelve pairs of Weyl points are predicted in each BZ, with four pairs at each of the k_z = 0 and $\pm 1.16\pi/c$ planes, respectively. (c) Fermi surface from ab initio calculations is plotted on the (001) surface BZ with the (projected) Weyl points (in red and blue) overlaid, showing the characteristic Fermi arcs. The color bar shows the surface contribution of the FS (white/0% to red/100%). (d) Calculated Fermi surface geometry with a fine k-space grid around the Y point of the BZ showing the Fermi arc (green curve). Different FS segments are color coded (with contributions indicated by the color bar) and labelled as FS 1-3. The inset shows the detailed evolution of different Fermi surface segments around the Weyl point. (e) Fermi surface measured using ARPES at high resolution showing excellent agreement with (d). The dashed line connects the two Weyl points for reference. The six arrows above and below the dashed line indicate the measurement positions in (f). (f) Three band dispersions measured above and below the dashed line in (e) (at the locations indicated by the red and green arrows in (e), respectively). Modified from reference [27] with permission from Springer Nature.

2.4 Nodal-line Semimetal

Unlike DSMs and WSMs, which possess zero-dimensional band crossings, i.e., discrete Dirac/Weyl points, NLSMs have one-dimensional nodal lines formed by the band crossings in the momentum space near or at the E_F. The nodal lines exhibit linear dispersions exclusively along directions that are perpendicular to them. Consequently, the low-energy excitations of NLSMs are massless along the transverse directions, while they are massive along the direction that is tangent to the nodal lines [11].

Each nodal line is associated with a topological invariant known as the winding number, *w*. Consider a closed loop that encircles the nodal line in the momentum space, as depicted in Figure 2.6. The winding number *w* is defined as the integral of the Berry connection along this loop, i.e.,

$$w = \int_l \boldsymbol{A} \cdot dl \tag{2.8}$$

where $\boldsymbol{A}$ is the Berry connection and *l* is the loop encircling the nodal line [28].

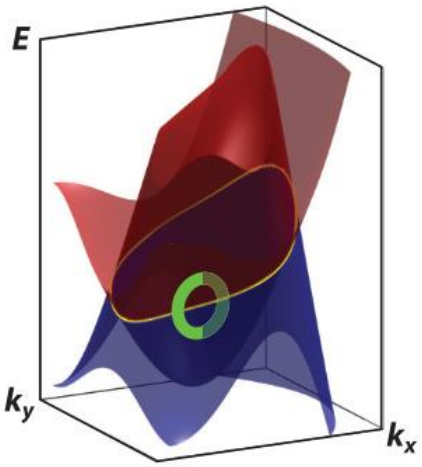

Figure 2.6: Schematic band structure of the NLSM. The conduction and valence bands are degenerate on a 1D closed loop, shown as the yellow circle in the BZ. The topological invariant of the nodal line is a winding number *w*, which is defined as the line integral of the Berry connection along a closed loop, shown as the green circle that encircles the nodal line. Modified from reference [28] with permission from Annual Reviews.

NLSMs can be classified based on the types of symmetry protection and the geometry of the nodal lines. First, nodal lines can exist as closed loops, also referred to as nodal circles, located within the BZ. In such cases, some nodal lines are protected by the combination of IS and TRS and are stable only in the absence of SOC, such as the theoretically proposed NLSM, Cu_3NPd [29]. In contrast, some other nodal lines are stable even in the presence of SOC. They are protected by the mirror-symmetry in the system with either IS or TRS breaking, such as $HgCr_2Se_4$ [30], or protected by the nonsymmorphic symmetry in the system with IS and TRS, such as $SrIrO_3$ [31]. Additionally, nodal lines can also exist as lines running across the BZ, such as in $BaTaS_3$ [32].

Chapter 3 Theory of Transport Properties of Topological Semimetals

In view of their distinctive electronic band structures, topological semimetals exhibit unique transport properties, including significant magnetoresistance (MR), anomalous Hall effect (AHE), negative longitudinal magnetoresistance, among others. Transport measurements provide an alternative approach for gaining insight into the physics of topological semimetals, complementing direct observation of band structure using ARPES. This chapter reviews the theory of topological semimetals' transport phenomena, covering magnetoresistance, Hall effect, and quantum oscillations.

3.1 Magnetoresistance

3.1.1 Lorentz Force-Induced Magnetoresistance

Magnetoresistance (MR) refers to the alteration in longitudinal electrical resistance R_{xx} (or resistivity ρ_{xx}) in the presence of an external magnetic field. It is defined as $MR = (R_{xx}(\mu_0 H) - R_{xx}(0))/R_{xx}(0)$ (or $MR = (\rho_{xx}(\mu_0 H) - \rho_{xx}(0))/\rho_{xx}(0)$), where $\mu_0 H$ is the external magnetic field, and $R_{xx}(0)$ (or $\rho_{xx}(0)$) is the longitudinal resistance (resistivity) in the zero magnetic field. The most common mechanism of MR is the Lorentz force. When the external magnetic field is perpendicular to the current, it causes the carriers' motion to be deflected. Because the resistivity is governed by the scattering processes depending on the velocity and direction of carriers' motion, the Lorentz force-induced deflection of motion results in a positive MR. It is worth pointing out

that ferromagnetic materials may exhibit negative MR due to the polarization of the electrons, particularly at temperatures close to their Curie temperatures [33].

In the study of semimetals, the analysis of magnetic field-dependent resistivity ρ_{xx} is usually conducted alongside the Hall resistivity ρ_{yx}, using the two-band model. The experimental data should be obtained under conditions in which the applied magnetic field is perpendicular to the current passing through the sample. The two-band model is a simple classical model that considers only one electron and one hole band in the studied material. While this model is clearly oversimplified for a real system, as it averages the effect of all electron (hole) bands and neglects interactions between them, it still provides insights into the carrier density and mobility of the material. The two-band model describes the ρ_{xx} and ρ_{yx} with the following two equations:

$$\rho_{xx}(B) = \frac{1}{e}\frac{(n_h\mu_h+n_e\mu_e)+(n_h\mu_e+n_e\mu_h)\mu_h\mu_eB^2}{(n_h\mu_h+n_e\mu_e)^2+(n_h-n_e)^2\mu_h{}^2\mu_e{}^2B^2} \tag{3.1}$$

$$\rho_{yx}(B) = \frac{B}{e}\frac{(n_h\mu_h{}^2-n_e\mu_e{}^2)+(n_h-n_e)\mu_h{}^2\mu_e{}^2B^2}{(n_h\mu_h+n_e\mu_e)^2+(n_h-n_e)^2\mu_h{}^2\mu_e{}^2B^2} \tag{3.2}$$

where $B = \mu_0 H$ is the magnetic field, n_h is the hole carrier density, n_e is the electron carrier density, μ_h is the hole mobility, and μ_e is the electron mobility [34]. According to the two-band model, a system with an n_h distinct from n_e exhibits a saturated MR under high magnetic fields. On the other hand, in an electron-hole compensated system where n_h equals n_e, a non-saturating MR proportional to B^2 is present under high magnetic fields. This kind of non-saturating quadratic MR has been observed in various compensated semimetals, such as semimetal LaBi [35] and type-II WSM $MoTe_2$ [36].

It is important to note that although the two-band model is widely used, it has certain limitations. Firstly, it is not applicable to open orbitals, which arise when the Fermi surface is not closed in momentum space. Secondly, it is a classical model that does not account for quantum

effects, such as orbit quantization [28]. Therefore, while the two-band model is useful in many cases, it should be applied with caution and with an understanding of its limitations.

3.1.2 Large Magnetoresistance in Topological Semimetals

The MR reaches a giant value at low temperatures (1.5 – 5 K) without saturation in many topological semimetals when the magnetic field is applied perpendicular to the current, as listed in Table 3.1 [28]. According to the two-band model, the MR is proportional to the carrier mobility. The carrier mobility μ is determined by the equation $\mu = e\tau/m^*$, where τ represents the relaxation time and m^* is the effective mass. In topological semimetals, the effective mass is extremely small due to the linear dispersions near the E_F, as confirmed by the experimental quantum oscillation results. The feature leads to a large carrier mobility, which results in a significant MR.

Table 3.1: Magnetoresistance (MR) at 9 T, residual resistivity ρ_{res}, transport mobility μ_T, quantum relaxation time τ_q, quantum mobility μ_q, and effective mass ratio m^*/m_0 of various topological semimetals at base temperatures (1.5 – 5 K). NA denotes the corresponding data not available. Adapted from reference [28] with permission from Annual Reviews.

	MR at 9 T	ρ_{res} (μΩ·cm)	μ_T [cm^2/(V·s)]	τ_q (ps)	μ_q [cm^2/(V·s)]	m^*/m_0
Cd_3As_2	34.5–1,336	0.032–46.5	4×10^3–8.7×10^6	0.03–0.21	4,700–6,000	0.023–0.26
Na_3Bi	5.69–97.1	1.72–87	5,500–78,900	0.0816	NA	0.11
TaAs family	3–30,000	0.63–1.9	18,000–10,000,000	0.038–1.1	32,000	0.021–0.68
WTe_2	4,000–25,000	0.39–1.9	24,000–176,000	NA	NA	0.41–0.46
$MoTe_2$	2,653	28	16,000–58,000	NA	NA	0.8–2.9
$PtSn_4$	1,000–2,100	NA	NA	NA	14,257–15,809	0.05–0.36
$PtBi_2$	12,000	NA	NA	NA	NA	NA
$Pt(Te/Se)_2$	A few tens	NA	3,600–5,500	NA	NA	0.11–3.6
$PdTe_2$	A few tens	NA	NA	0.18–0.65	1,293–6,209	0.04–1.16
AMn(Sb/Bi)$_2$ (A = Ca, Sr, Ba, Yb)	1	NA	1,500–3,400	NA	NA	NA
WHM (W = Zr or Hf; H = Si, Ge, or Sn; M = S, Se, or Te)	1.3–1,400	0.052	2,000–28,000	0.025–0.35	209–10,000	0.025–0.27, 1.32

The two-band model has proven to be an effective model for explaining the non-saturating quadratic MR. However, it falls short in explaining the non-saturating linear MR (see Figure 3.1) observed in certain topological semimetals, such as NLSM ZrGeSe [37] and WSM CoS_2 [38]. While the inhomogeneous carrier density in disordered systems can lead to a linear MR [39], this is not the case in high-quality nanoflakes or single crystals used in these studies. The linear MR in ZrGeSe nanoflake is ascribed to the linearly dispersed bands, according to Abrikosov's quantum linear MR theory, which will be reviewed in **section *3.3.3***. The linear MR observed in CoS_2 single

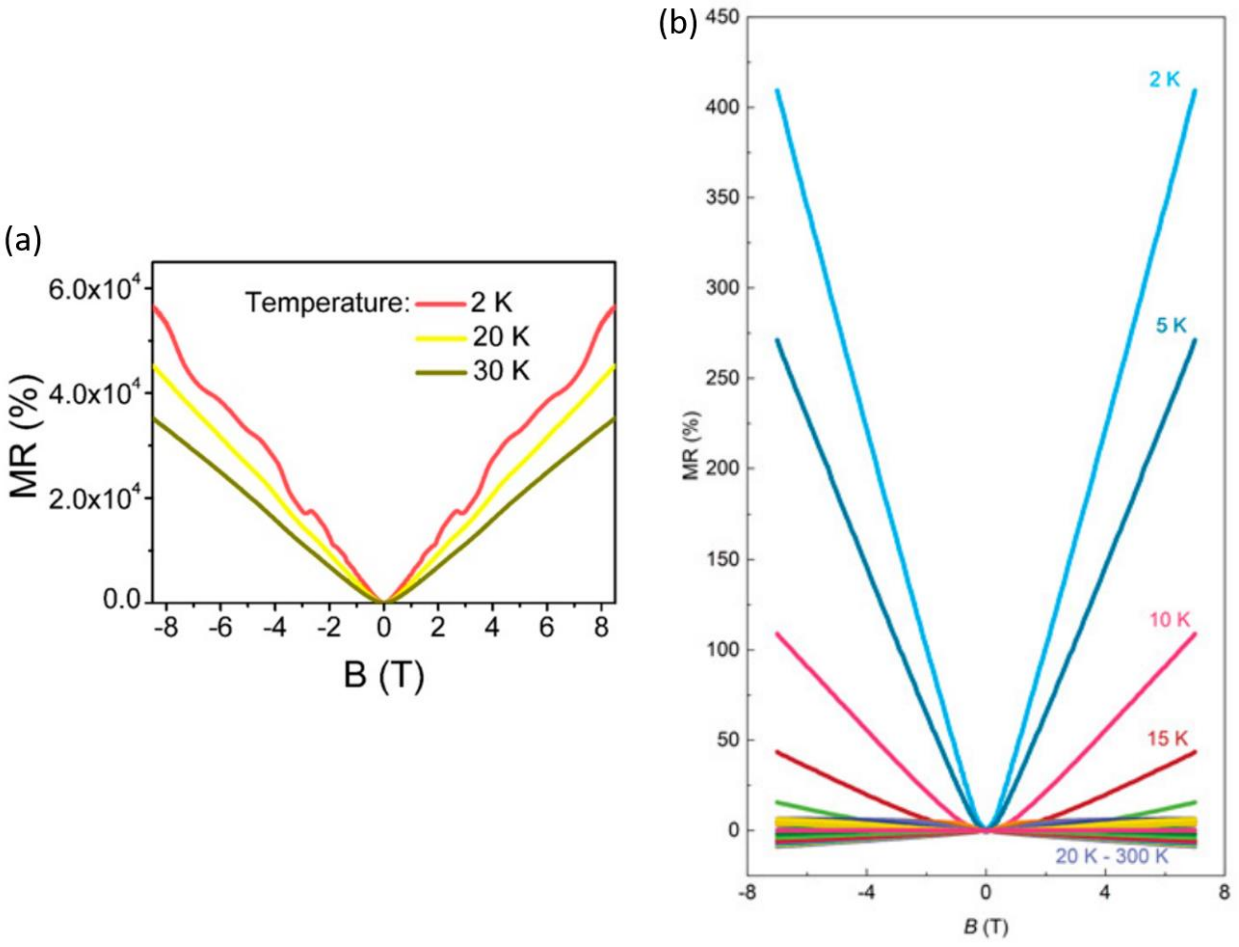

Figure 3.1: (a) MR of ZrGeSe nanoflake. Adapted with permission from [37]. Copyright 2024 American Chemical Society. (b) MR of CoS_2 single crystal. Large linear MR is observed below 20 K. Adapted from reference [38] (Copyright National Academy of Sciences of the United States of America).

crystal, on the other hand, has been explained by researchers through a model that elucidates the interplay of the magnetic field in real space and the Berry curvature in momentum space. The model suggests that the slope of the linear MR is determined by the average Berry curvature in the vicinity of the Fermi surface [38]. It is clear that the linear MR is strongly linked to the unique band structure of topological semimetals, and, therefore, it cannot be accounted for by the classical model.

3.1.3 Chiral Anomaly-Induced Negative Longitudinal Magnetoresistance

Consider a WSM with only one pair of Weyl points with opposite chirality. The chemical potentials of left-handed and right-handed Weyl fermions are equivalent in the absence of both electric field $\boldsymbol{E}$ and magnetic field $\boldsymbol{B}$, which implies that the number of electrons with opposite chirality is equal. When a magnetic field $\boldsymbol{B}$ is applied, the Weyl bands are quantized into Landau levels (LLs), which can be expressed by the following equations:

$$\varepsilon_n = v_F sgn(n)\sqrt{2\hbar|n|eB + \left(\hbar \boldsymbol{k}\cdot\widehat{\boldsymbol{B}}\right)^2}, \quad n = \pm1, \pm2, \dots,$$

$$\varepsilon_0 = -\chi\hbar v_F \boldsymbol{k}\cdot\widehat{\boldsymbol{B}}, \qquad \chi = \pm1 \tag{3.3}$$

where n is the index of LL, v_F is the Fermi velocity, and χ is the chirality of the Weyl points. The energy levels become discrete, and only the zeroth LL is linearly dispersed and chiral, crossing the E_F [11], as illustrated in Figure 3.2a. Suppose the system is in the quantum limit at low temperatures, i.e., only the zeroth LLs contribute to the low-energy physics. If an electric field $\boldsymbol{E}$ is applied parallel to the magnetic field $\boldsymbol{B}$, the applied electric field would shift the chemical potential, leading to an imbalance of the occupied states in the left-handed and right-handed LLs and, thus, a charge pumping from one Weyl point to the other. This is known as the chiral anomaly.

The Chiral anomaly can be manifested by the negative longitudinal magnetoresistance. In a sufficiently clean system, the backscattering of electrons with opposite chirality is effectively suppressed. Consequently, the rate at which electrons are pumped from one Weyl point to the other is proportional to $\boldsymbol{E} \cdot \boldsymbol{B}$, resulting in a negative longitudinal magnetoresistance [11].

Figure 3.2b shows the longitudinal magnetoresistance of DSM Na_3Bi at different temperatures. As previously discussed in Chapter 2, the applied magnetic field breaks the TRS and converts the DSM into a WSM. The two overlapping Weyl points that make up the Dirac point are

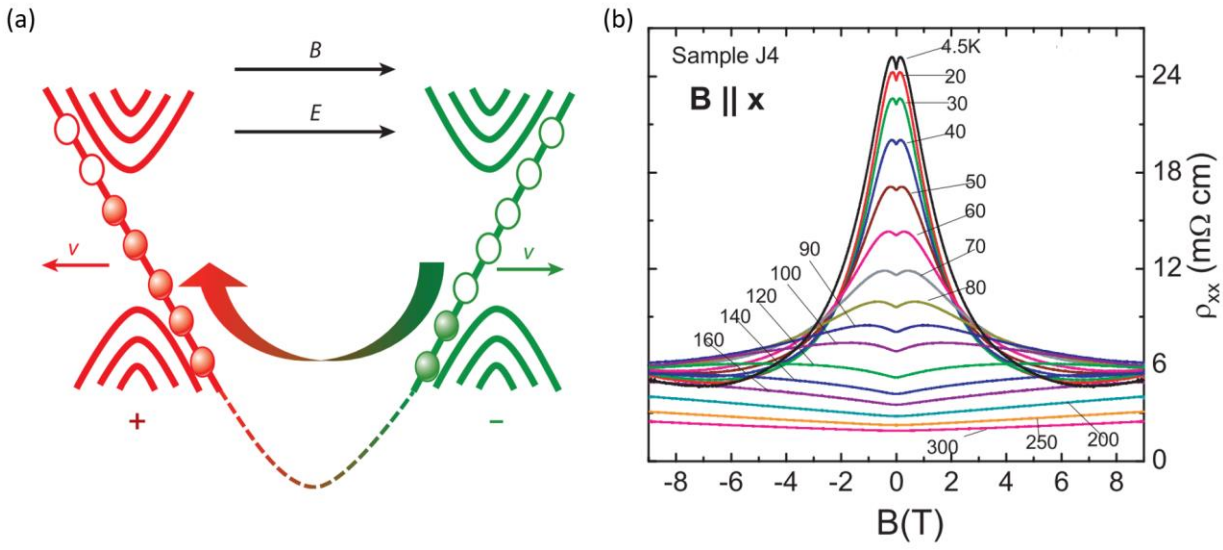

Figure 3.2: (a) Illustration of chiral anomaly. Red and green colors represent right-handed and left-handed electrons separately. Solid and open circles denote occupied and unoccupied states, respectively. Adapted from reference [25] with permission from Annual Reviews. (b) Longitudinal magnetoresistance of Na_3Bi at selected temperature from 4.5 to 300 K. Adapted from reference [40] with permission from AAAS.

positioned separately in the direction of the applied magnetic field. Indeed, negative longitudinal magnetoresistance has been observed in Na_3Bi. At temperatures below 100 K, an increase in magnetic field results in a decrease in longitudinal magnetoresistance [40]. However, it is important to note that the chiral anomaly-induced negative longitudinal magnetoresistance is not

observed in all DSMs and WSMs. To observe this phenomenon, the system must be clean enough with negligible scattering between Weyl points and only Dirac or Weyl cones present at/near the E_F without the presence of other trivial bands.

3.2 Hall Effect

In 1879, Edwin H. Hall discovered a transverse electromotive force within a conductor carrying current when placed in a magnetic field. This phenomenon, which came to be known as the ordinary Hall effect, is directly proportional to the magnetic field and current [41]. The Hall resistance is defined as the ratio of the transverse voltage to the current. In a system with only one carrier type, the Hall resistance displays a linear relationship with the magnetic field. The corresponding Hall resistivity ρ_{yx} is equal to B/ne, where B is the magnetic field, and n is the carrier density. In a system with two types of carriers, a hole-like and an electron-like, ρ_{yx} follows the equation (3.2) as mentioned before. The ordinary Hall effect provides an effective method to identify the types of a material's carriers as well as their corresponding carrier densities.

A few years later, Hall found that the transverse voltage was significantly larger in ferromagnetic materials compared to nonmagnetic materials. This stronger effect is referred to as the anomalous Hall effect (AHE) [42]. In ferromagnetic materials, ρ_{yx} is found to be closely related to the material's magnetization M_z. Empirically, a relationship between them has been established as follows:

$$\rho_{yx} = R_0 B + R_s M_z \tag{3.4}$$

Here, $R_0 B$ denotes the contribution of the ordinary Hall effect, $R_s M_z$ denotes the contribution of the AHE, and R_0 and R_s are the ordinary and anomalous Hall coefficients, respectively [42]. Unlike the ordinary Hall effect, the AHE results in a non-zero ρ_{yx} in the absence of an external magnetic field, named anomalous Hall resistivity. The mechanisms responsible for the occurrence

of anomalous Hall resistivity can be classified into two categories: intrinsic and extrinsic (side-jump and skew-scattering), as illustrated in Figure 3.3, which will be further reviewed in the subsequent text.

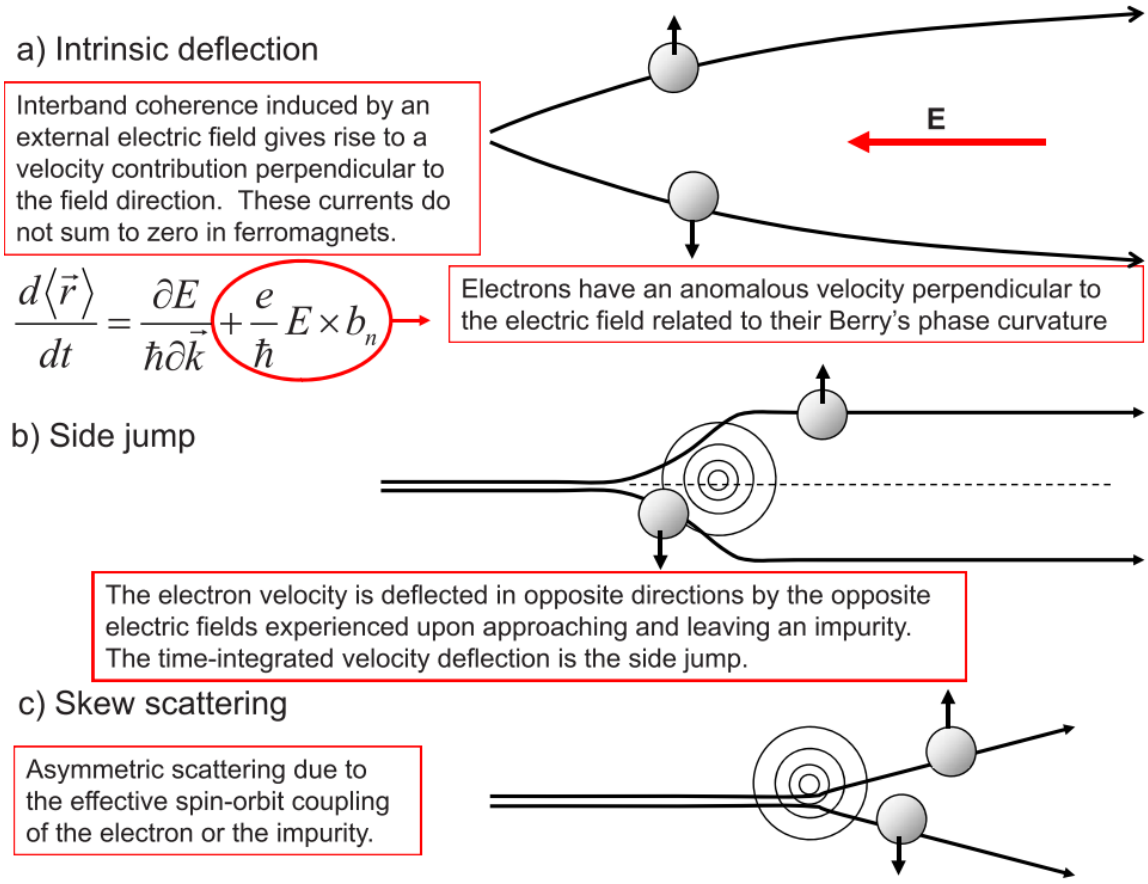

Figure 3.3: Illustration of the three main mechanisms that can give rise to an AHE. In any real material all of these mechanisms act to influence electron motion. Adapted from reference [42] with permission from the American Physical Society.

3.2.1 Intrinsic Anomalous Hall Effect

The theory of the intrinsic AHE was first proposed by Karplus and Luttinger in 1954 [43]. They demonstrated that in the presence of an external electric field, electrons acquire an additional

group velocity perpendicular to the electric field. In ferromagnetic conductors, the sum of this anomalous velocity over all occupied states is non-zero, contributing to the Hall conductivity σ_{xy}. Because this contribution is independent of scattering, only depending on the band structure, it is known as the intrinsic contribution to AHE. The intrinsic anomalous Hall conductivity, σ_{xy}^{int}, is thus independent of the longitudinal conductivity σ_{xx}, and the corresponding intrinsic anomalous Hall resistivity is proportional to ρ_{xx}^2.

After the concepts of the Berry phase and topology have been introduced in solid-state physics, the intrinsic anomalous Hall conductivity was directly linked to the integration over the Fermi sea of the Berry curvature of each occupied band. More precisely, it is evaluated using the following equation:

$$\sigma_{ij}^{int} = -\varepsilon_{ijl}\frac{e^2}{\hbar}\sum_n \int_{BZ}\frac{d\boldsymbol{k}}{(2\pi)^d} f(\varepsilon_n(\boldsymbol{k}))\boldsymbol{b}_n^l(\boldsymbol{k}) \tag{3.5}$$

where ε_{ijl} is the antisymmetric tensor, $\varepsilon_n(\boldsymbol{k})$ is the eigenvalue of the eigenstate $|n, \boldsymbol{k}\rangle$, f is the Fermi-Dirac distribution, and $\boldsymbol{b}_n(\boldsymbol{k})$ is the Berry curvature. In a magnetic system, TRS is broken, i.e., $\boldsymbol{b}_n(\boldsymbol{k}) \neq -\boldsymbol{b}_n(-\boldsymbol{k})$, which can give rise to a non-zero intrinsic anomalous Hall conductivity. The intrinsic contribution has been observed to dominate the AHE in many materials with strong SOC [42].

The Weyl points in WSMs, which can be regarded as monopoles of Berry curvature, may result in a large intrinsic AHE in TRS-breaking WSMs. Indeed, magnetic WSMs, such as $Co_3Sn_2S_2$ [44], Co_2MnAl [45], and Mn_3Sn [46], exhibit significant σ_{xy}^{int}. The AHE in these materials is intrinsic and controllable through the separation of Weyl points. Consequently, these materials have promising potential for spintronic applications [28].

3.2.2 Extrinsic Anomalous Hall Effect

The intrinsic AHE is solely determined by the Hamiltonian of the perfect crystal, as introduced above. However, in real materials, transport properties are also influenced by scatterings due to defects and impurities, so as the AHE. The contributions to AHE caused by such scatterings are divided into two distinct mechanisms: skew-scattering and side-jump.

3.2.2.1 Skew-Scattering Contribution to Anomalous Hall Effect

The skew-scattering mechanism was first proposed by Smit, indicating that the skew-scattering is due to the asymmetric scattering, caused by the SOC, of the conducting electrons against the defects in ferromagnetic materials [47, 48].

In semiclassical Boltzmann transport theory, the transition probability $W_{n\to m}$ is conventionally considered equal to that in the opposite direction, $W_{m\to n}$. However, in the presence of SOC, the transition probability for a right-handed transition with respect to the magnetization direction differs from that of the left-handed transition. When this asymmetry is introduced into the Boltzmann equation, it results in a current proportional to the longitudinal current driven by the applied electric field $\boldsymbol{E}$ and perpendicular to both $\boldsymbol{E}$ and the magnetization. The skew-scattering mechanism tends to dominate AHE in nearly perfect crystals (with high conductivity greater than $10^6(\Omega\, cm)^{-1}$). In this case, both Hall conductivity σ_{xy} and the longitudinal conductivity σ_{xx} are proportional to the Bloch state transport lifetime, and thus, the Hall resistivity ρ_{yx} is proportional to ρ_{xx} [42].

3.2.2.2 Side-Jump Contribution to Anomalous Hall Effect

When a Gaussian wave packet interacts with a spherical impurity possessing SOC, the incident wave vector $\boldsymbol{k}$ undergoes a transverse displacement of $\frac{1}{6}k\hbar^2/m^2c^2$. This mechanism is

known as the side-jump, which was proposed by Berger [49]. The side-jump contribution to the AHE is independent of the transport lifetime and, therefore, is independent of σ_{xx}. As a result, the corresponding anomalous Hall resistivity is proportional to ρ_{xx}^2 . Because the side-jump contribution to the AHE is of the same order as the intrinsic contribution, they cannot be distinguished by their dependence on the transport lifetime. In practice, for materials with anomalous Hall conductivity independent of σ_{xx}, one may first calculate the intrinsic contribution to the AHE. If the calculation result is consistent with the experimental data, the observed anomalous Hall conductivity is ascribed to the intrinsic contribution. Otherwise, it may be attributed to the side-jump contribution [42].

3.3 Quantum Oscillations

Quantum oscillation is a significant phenomenon that offers valuable insights into topological semimetals, including quantum mobility, effective mass, and Berry phase. Quantum oscillations can be observed in the electrical resistance (known as the Shubnikov-de Haas (SdH) effect), magnetization/magnetic torque (known as the de Haas-van Alphen (dHvA) effect), thermoelectric power, etc.

3.3.1 Landau Quantization

The phenomenon of quantum oscillation emerges from the quantized cyclotron motion of charge carriers under magnetic fields, which is also known as the Landau quantization of energy states. With the conduction bands splitting to Landau levels (LLs), the density of states (DOS) at the Fermi level becomes periodic, resulting in the related physical quantities oscillating as a function of the inverse of the magnetic field, i.e., $1/B$. For 2D spinless nonrelativistic electrons with parabolic band dispersions in the presence of an applied magnetic field, the LL energy is $\varepsilon_n =$

$(n + 1/2)\hbar\omega_c$, where $\omega_c = eB/m^*$ represents the cyclotron motion frequency, m^* is the effective mass, and $n = 0, 1, 2, ...$ denotes the LL index. The LL energies are evenly spaced and field-dependent, with the lowest LL having a non-zero energy of $\hbar\omega_c/2$. For the purpose of distinguishing the lowest LL of the nonrelativistic electrons from the zeroth LL with zero energy of the relativistic electrons, here we rewrite the LL energy of 2D nonrelativistic electrons as $\varepsilon_n = (n - 1/2)\hbar\omega_c$, where $n = 1, 2, 3, ...$ The corresponding spectra are illustrated in Figure 3.4b [28].

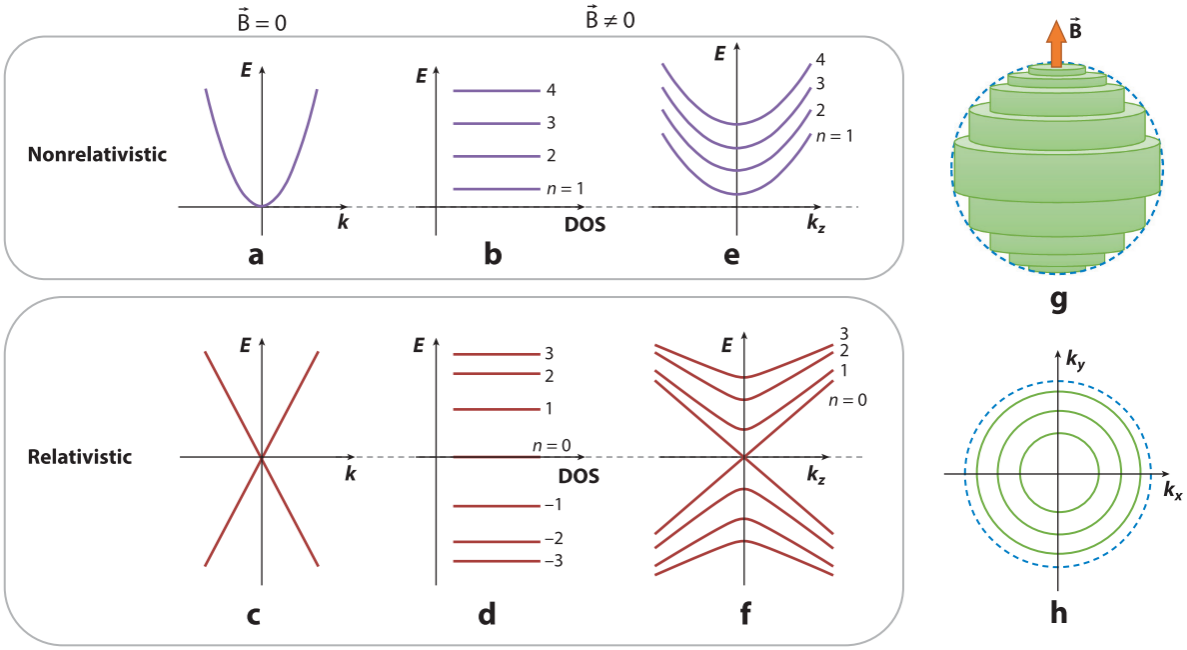

Figure 3.4: Schematics of energy dispersions of (a) nonrelativistic and (c) relativistic electrons. Landau spectra of the 2D spinless (b) nonrelativistic and (d) relativistic electrons. Landau spectra of the 3D spinless (e) nonrelativistic and (f) relativistic electrons with the magnetic field along the k_z direction ($\boldsymbol{B} \parallel k_z$). (g) Landau tubes intersecting a 3D spherical Fermi surface. (h) Landau rings within the 2D Fermi surface. Adapted from reference [28] with permission from Annual Reviews.

For 2D spinless relativistic electrons with linear band dispersions, the LL energy can be expressed as $\varepsilon_n = v_F sgn(n)\sqrt{2e\hbar B|n|}$, where v_F is the Fermi velocity and $n = 0, \pm1, \pm2, ...$, as shown in Figure 3.4d. It is noteworthy that the zeroth LL of 2D spinless relativistic electrons is

fixed at the position of the band crossing. The zeroth LL energy is zero and independent of the magnetic field, which is entirely different from that of 2D nonrelativistic electrons.

Given that the vast majority of topological semimetals reported to date are in 3D form, it is necessary to present the Landau quantization results of 3D electrons. For 3D nonrelativistic electrons, when the external magnetic field is applied along the k_z direction, the LL energy follows the equation:

$$\varepsilon_{n,k} = (n - 1/2)\frac{\hbar eB}{m^*} + \frac{\hbar^2 k_z^2}{2m^*},\ (n = 1, 2, 3, \dots) \tag{3.6}$$

The energy along the magnetic field direction is not quantized. Similarly, in the case of 3D relativistic electrons, the LL energy is given by the equation:

$$\varepsilon_{n,k} = v_F sgn(n)\sqrt{2e\hbar B|n| + (\hbar k_z)^2},\ (n = 0, \pm 1, \pm 2, \dots) \tag{3.7}$$

The zeroth LL energy is still independent of the magnetic field, although not strictly zero. Equation (3.7) is valid for Dirac fermions. However, the expression for the zeroth LL energy requires modification in the case of Weyl fermions, as the spin degeneracy is lifted. This has been discussed in section 3.1.3 (see equation (3.3)).

3.3.2 The Lifshitz–Kosevich Formula

As presented in the last section, for 3D electrons, different LLs overlap in the energy space due to the unquantized energy along the magnetic field direction. The LL energy states lie on the Landau tubes, and, thus, the spherical Fermi surface intersects with multiple Landau tubes (see Figure 3.4g). However, for 2D electrons, the LL energy states lie on the Landau rings, and the circular Fermi surface does not intersect with multiple Landau rings (see Figure 3.4h). Consequently, different equations are utilized to describe the 3D and 2D quantum oscillations. In

the subsequent chapters of this thesis, the findings regarding quantum oscillations are all in 3D materials. Therefore, we primarily focus on the formulas for 3D electrons.

At the zero-temperature limit, the oscillatory Gibbs thermodynamic potential Ω for a quantized 3D system follows the equation:

$$\Omega_{osc} = \left(\frac{e}{2\pi c\hbar}\right)^{3/2} \frac{e\hbar B^{5/2}}{m^* c\pi^2 (\partial^2 S_{extr}/\partial k_z^2)^{1/2}} \sum_{r=1}^{\infty} \frac{1}{r^{5/2}} \cos\left[2\pi r\left(\frac{F}{B} - \gamma\right) + 2\pi\delta\right] \tag{3.8}$$

where S_{extr} refers to the extremal Fermi surface cross-section area perpendicular to the magnetic field, $\partial^2 S_{extr}/\partial k_z^2$ is the curvature of the extremal Fermi surface along the magnetic field direction k_z, r is the harmonic index, m^* is the effective mass, and rF is the oscillation frequency. Because the magnetization is the derivative of the Gibbs thermodynamic potential at constant temperature T and chemical potential ζ, the oscillatory magnetization can be expressed by the so-called Lifshitz-Kosevich formula (the LK formula):

$$M_{osc}^{3D} = -\left(\frac{\partial \Omega}{\partial B}\right)_{T,\zeta}$$

$$= -\left(\frac{e}{2\pi\hbar}\right)^{3/2} \frac{S_{extr}}{\pi^2 m^*} \left(\frac{B}{|\partial^2 S_{extr}/\partial k_z^2|}\right)^{1/2} \sum_{r=1}^{\infty} \frac{1}{r^{3/2}} R_T R_D R_S \sin\left[2\pi r\left(\frac{F}{B} - \gamma + \frac{\delta}{r}\right)\right] \tag{3.9}$$

where R_T, R_D, and R_S are the temperature, field, and spin damping factor, separately. The temperature damping factor R_T is related to the finite temperature corrections to the Fermi-Dirac distribution function, which can be expressed as

$$R_T = \frac{raT\mu/B}{\sinh(raT\mu/B)} \tag{3.10}$$

where μ is the ratio of effective cyclotron mass m^* to free electron mass m_0, and $a = \frac{2\pi^2 k_B m_0}{\hbar e} \approx 14.69\ \mathrm{T/K}$. The field damping factor R_D, caused by the finite quantum relaxation time, can be expressed as

$$R_D = \exp\left(-\frac{raT_D\mu}{B}\right) \tag{3.11}$$

where T_D is known as the Dingle temperature, linked to the quantum relaxation time τ_q through the formula $T_D = \hbar/2\pi k_B \tau_q$. And the last, the spin damping factor R_S is due to the phase difference between the spin-up and spin-down subands, which can be expressed as

$$R_S = \cos\frac{r\pi g\mu}{2} \tag{3.12}$$

where g is the Landé g-factor. The rF in the sinusoidal term in equation (3.9) represents the oscillation frequency, while the fundamental frequency F is connected to S_{extr} via the Onsager relation: $F = (\hbar/2\pi e)S_{extr}$. The phase factor $2\pi r\left(-\gamma + \frac{\delta}{r}\right)$ in the sinusoidal term is associated with the Berry phase ϕ_B through the relation $\gamma = \frac{1}{2} - \frac{\phi_B}{2\pi}$. The phase shift δ is determined by the dimensionality of the Fermi surface, i.e., $\delta = 0$ for 2D Fermi surfaces and $\delta = \pm\frac{1}{8}$ for 3D Fermi surfaces.

In practice, the quantum oscillation frequencies can be acquired from the fast Fourier transform (FFT) of the oscillatory components of the magnetization. Normally, the fundamental frequencies dominate quantum oscillations in real materials since components with higher harmonic frequencies rF $(r > 1)$ are rapidly damped with $r^{-3/2}$. The effective mass of each frequency band can be obtained by fitting the corresponding FFT amplitudes at different temperatures using equation (3.10). In systems with Dirac points located at or near the E_F, the effective mass is typically small due to the linear dispersions. Indeed, most topological semimetals exhibit a very small effective mass, as evidenced in Table 3.1 [28]. After knowing the effective mass, the Dingle temperature can be obtained by fitting the field-dependent oscillation amplitude at a fixed temperature to equation (3.11). Then, the quantum relaxation time can be calculated, which is generally large in topological semimetals.

In the analysis of quantum oscillations in topological semimetals, the phase factor is a crucial parameter, alongside the effective mass and quantum mobility, since the nontrivial Berry phase is a hallmark of relativistic electrons. The Berry phase ϕ_B can be extracted from the LL index fan diagram, which plots the LL indices n against the inverse of magnetic field $1/B$. The integer LL indices are assigned when E_F lies in the middle of two adjacent LLs, i.e., the DOS at E_F reaches its minimum. In contrast, the half-integer LL indices are assigned when E_F lies right at a LL, i.e., the DOS at E_F reaches its maximum. For the LL fan diagram of a 3D system plotted under such rules, the linear extrapolated line of the linear fit of $n(\frac{1}{B})$ intersects the n axis at $\frac{\phi_B}{2\pi} - \delta$. The extracted ϕ_B from the LL fan diagram may deviate from the ideal value of π if the band is not perfectly linear. Moreover, the Zeeman effect and uncertainty of the intercept of the linear fit of $n(\frac{1}{B})$ can also lead to deviation [28]. Therefore, analyzing quantum oscillations using the LL fan diagram requires careful consideration of these factors.

The effective mass, Dinger temperature, and phase factor can also be acquired by fitting the oscillatory components with the multiband LK formula, assuming the quantum oscillations of different bands are additive. However, the fitting process can be complicated by the increased number of fitting parameters.

Besides magnetization, quantum oscillations have been observed in other physical quantities, including magnetic torque, resistivity, and thermoelectric power [50].

3.3.3 Beyond the Quantum Limit

When the applied magnetic field is strong enough, all electrons in a band become confined to the lowest LL, and the quantum limit is reached. The critical magnetic field needed to achieve the quantum limit is at least comparable to the quantum oscillation frequency [28]. The enhanced

degeneracy of the lowest LL along with the distinct properties of relativistic electrons may lead to the emergence of novel and exotic phenomena in topological semimetals.

As previously discussed, in a system with nonrelativistic electrons, the lowest LL energy increases linearly with the magnetic field. However, in WSMs, the zeroth LL energy is independent of the magnetic field. Therefore, in the case of quantum limit, the magnetization, $M_{n=0} = -\partial\varepsilon_{0,k}/\partial B$, saturates to a field-independent value in a nonrelativistic system, while it vanishes in a WSM. This anomaly has been observed in the magnetic torque of WSM NbAs under high magnetic fields [51].

Another phenomenon associated with the quantum limit is the linear MR. Abrikosov proposed that when the quantum limit is reached in a system with linear dispersions, the quantum linear magnetoresistance may occur due to the small pockets of the Fermi surface with a small effective mass [52, 53]. The linear MR observed in NLSM ZrGeSe has been well explained by this theory [37].

Chapter 4 Magnetic and Transport Properties of Fe-doped Weyl Semimetal $Co_3Sn_2S_2$

4.1 Motivation

$Co_3Sn_2S_2$, a member of the ternary chalcogenide shandite family, crystallizes in a rhombohedral lattice (space group $R\,\bar{3}\,m$). As shown in Figure 4.1 (drawn using VESTA [54]), $Co_3Sn_2S_2$ has a quasi-two-dimensional structure, where Co and Sn atoms form Kagomé lattice layers sandwiched between S and Sn atoms. $Co_3Sn_2S_2$ is a ferromagnetic material with a Curie temperature of ~174 K and exhibits metallic behavior as its resistivity increases with the increasing temperature [55, 56]. The Co atoms on the Kagomé lattice are the origin of the out-of-plane ferromagnetic order in $Co_3Sn_2S_2$. At the same time, $Co_3Sn_2S_2$ is a Weyl semimetal [57]. It has a high mobility and a large non-saturating magnetoresistance, which are usually seen in topological semimetals [58-60]. In addition, $Co_3Sn_2S_2$ shows a giant anomalous Hall conductivity ~ $1130\ \Omega^{-1}cm^{-1}$ and an anomalous Hall angle ~ 20 % due to its enhanced Berry curvature arising from interactions between its topological band structure and intrinsic ferromagnetism [61, 62]. The spin-orbit coupling (SOC)-induced gap structure along the nodal line, which plays a key role in generating the large Berry curvature, has been implied by the *ab initio* calculations and directly observed using high-resolution angle-resolved photoemission spectroscopy (ARPES) [63]. Recently, simulation results predict possible chiral edge states on an exposed Kagomé Co_3Sn terrace of bulk $Co_3Sn_2S_2$ and suggest that the 2D limit of $Co_3Sn_2S_2$ is a Chern insulator hosting the quantum anomalous Hall effect [64]. Moreover, $Co_3Sn_2S_2$ is identified as a half metal. Techniques

like photoemission [65] and scanning tunneling microscopy [66], and also the analysis of the modified electron-magnon scattering behavior that uses the temperature and magnetic field-dependent electrical resistivity reveal the half-metallic nature of $Co_3Sn_2S_2$ experimentally [67].

Thanks to its exceptional physical properties, $Co_3Sn_2S_2$ is a potential candidate for functional applications in numerous fields, such as thermoelectricity, chemical catalysis, and nonlinear optics. The low electrical resistance and high Seebeck coefficient of $Co_3Sn_2S_2$ are attractive for thermoelectricity [68-71]. The maximum figure-of-merit $ZT = 0.3$ is reached in the temperature range 373K ~ 573 K by doping Fe and In into pristine $Co_3Sn_2S_2$, and such ZT value exceeds that of many n-type sulfides in this temperature range [72]. The high electrical conductivity and the desirable carrier density near the Fermi level also make $Co_3Sn_2S_2$ appealing as cathodes for aqueous Zn-ion batteries, inspiring chemists to utilize topological materials to build high-performance electrochemical batteries [73]. Because the topological states can provide high carrier mobility and are robust against surface deformation or reformation, $Co_3Sn_2S_2$ is a promising material for electrocatalysis. Indeed, it shows an excellent performance for oxygen evolution reactions compared with topological trivial material catalysts [74, 75]. In the nonlinear optics field, it was found that the second harmonic generation phenomenon, often used to investigate non-centrosymmetric materials, can be realized in the inversion-symmetric $Co_3Sn_2S_2$ by applying a finite current, and the induced susceptibility can reach 10^5 pm V^{-1}: a value 10^2-10^4 times greater than those obtained in typical optical materials [76].

Chemical doping is an effective method to modify the physical properties of materials, as it can adjust the position of the Fermi level, induce impurities, and change the grain size. Some chemical doping-related works have been done on $Co_3Sn_2S_2$. For instance, substitutions of In for Sn and Fe for Co enhance the thermoelectric performance of the compound, whereas substitution

of Ni for Co weakens the performance [69, 71]. Moreover, while all such substitutions tend to suppress the magnetism of $Co_3Sn_2S_2$, the resulting solid solutions still show ferromagnetic order below the Curie temperature [77-79]. Nevertheless, Ni-doped $Co_3Sn_2S_2$ solutions maintain the significant anomalous Hall conductivity that has been observed in pure $Co_3Sn_2S_2$, which indicates the robustness of its topological originating anomalous Hall effect (AHE) [80]. However, little has been done on purely Fe-doped $Co_3Sn_2S_2$ solid solutions among the above noted chemical doping-related works. Therefore, in this study, I provide a more detailed account of investigations concerning the magnetic and transport properties of polycrystalline $Co_{3-x}Fe_xSn_2S_2$ in the temperature range 1.8 K ~ 300 K, with the value of x up to 0.4, the content close to the solubility limit ~ 0.5 at ambient conditions [77].

The DC zero-field-cooled (ZFC) and field-cooled (FC) temperature-dependent magnetization curves were measured to reveal the influence of Fe-doping on the samples' magnetic order and an anomalous phase right below the paramagnetic-ferromagnetic transition temperature T_C. The Hall resistivity measurement displays the intrinsic AHE of pure $Co_3Sn_2S_2$ and the complicated Hall effect in the Fe-doped systems. Both the transverse and longitudinal magnetoresistance (MR) of pure and the heaviest Fe-doped $Co_3Sn_2S_2$, are evaluated and compared. Thermal properties, such as heat capacity, Seebeck coefficient, and thermal conductivity, were also measured. In addition, formation energies, band structures, and spin-polarized density of states (DOS) calculated by using the spin-polarized relativistic Korringa-Kohn-Rostoker – Green's function method (sprKKR) [81] are also displayed. Overall, I provide a careful and comprehensive investigation of low-temperature magnetic and transport properties of Fe-doped $Co_3Sn_2S_2$ polycrystals.

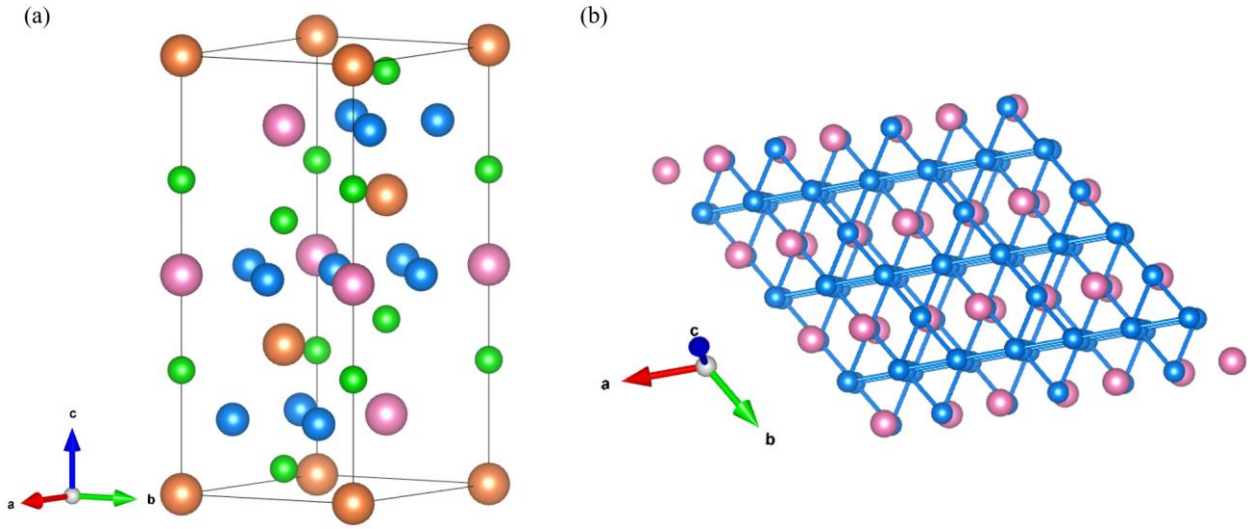

Figure 4.1: Crystal structure of $Co_3Sn_2S_2$. (a) Conventional unit cell of $Co_3Sn_2S_2$. Orange ball represents Sn(1) siting at 3(a) (0, 0, 0); Pink ball represents Sn(2) siting at 3(b) (0, 0, 1/2); Blue ball represents Co siting at 9(d) (1/2, 0, 1/2); and Green ball represents S siting at 6(c) (0, 0, z). (b) Kagomé lattice structure within Co-Sn(2) layers.

4.2 Methods

4.2.1 Experimental Methods

Polycrystalline $Co_{3-x}Fe_xSn_2S_2$ (x = 0, 0.1, 0.2, 0.3, and 0.4) samples were synthesized by the conventional solid-state method. Stoichiometric amounts of tin (99.999%, shot, Alfa Aesar), sulfur (99.999%, pieces, Acros Organics), cobalt (99.998%, powder, Alfa Aesar) and iron (99.998%, powder, Alfa Aesar) were put into alumina crucibles, which were then sealed in quartz tubes under vacuum. The sealed quartz tubes were placed vertically in the box furnace and heated to 1050 ℃ in 48 h with a dwell time of 24 h. Then, the tubes were slowly cooled to 600 ℃ in 180 h. After that, the tubes were cooled to room temperature with a faster cooling rate of 120 ℃/h. The resulting silver shinning ingots were ground into powders, and subsequently consolidated by spark plasma sintering (SPS, FCT Systeme GmbH) in a 12.7 mm diameter graphite die lined with graphite paper under an axial compressive force of 6 kN in vacuum for 1 h at 720 ℃. The acquired disk-shape pellets were polished with sandpaper and cut into small pieces having the desired size

and shape for structural characterization, magnetization, and transport measurements. The pieces for structural characterization were reground into powder, and their crystal structures were confirmed by powder X-ray diffraction (PXRD) using a Rigaku Ultima IV X-ray diffractometer (Cu K_α).

A Physical Property Measurement System (PPMS Dynacool, Quantum Design) was used for all magnetization and transport measurements. The ZFC and FC temperature-dependent magnetization curves were acquired using the Vibrating Sample Magnetometer (VSM) in the following way: to get ZFC curves, each sample was first cooled to 1.8 K with no applied magnetic field; then, a 100 Oe external field was applied, and the magnetic moment of the sample was recorded while the sample was warming to 300 K. The sample was subsequently cooled to 1.8 K in the presence of 100 Oe external field, and the magnetic moment of the sample was again measured while the sample was slowly heated to 300 K to obtain FC curves. Electrical resistivity and Hall resistivity were measured using the Electrical Transport Option (ETO). The heat capacity data were acquired using the Heat Capacity Option. The thermal conductivity and Seebeck coefficient were measured using the Thermal Transport Option (TTO) of the PPMS. To correct for magnetic field-induced temperature errors due to the magnetoresistance (MR), the resistive thermometers were calibrated using the PPMS MR calibration wizard before the transport measurement.

4.2.2 Computational Method

The electronic structures of $Co_{3-x}Fe_xSn_2S_2$ compounds were computed in the full-potential mode using the Korringa-Kohn-Rostoker (KKR) multiple scattering theory [81]. The exchange-correlation potential was modeled by using the Perdew–Burke–Ernzerhof (PBE) parametrization in the scheme of the generalized gradient approximation (GGA) [82]. An angular momentum

cutoff of l_{max} = 3 was used for the expansion of the Green's function, and the irreducible wedge of the Brillouin zone was sampled with a 24 × 24 ×24 *k*-point mesh. To further improve the charge convergence with respect to l_{max}, Lloyd's formula is used to determine the Fermi level. All calculations were carried out in the relativistic representation of the valence states; thus, SOC is taken into account. The dopant-induced disorder between different chemical species occupying the same atomic site was considered with the mean-field coherent potential approximation (CPA) [83]. This effective medium method offers advantages over the supercell method in terms of computation resource requirement and time and configurational issues. Alternatively, for comparison, DOS was calculated based on the KKR multiple scattering theory with the consideration of many-body effects described by using the dynamical mean field theory (DMFT) [84] in a charge and self-energy self-consistent computational scheme. To examine the band structure of $Co_{3-x}Fe_xSn_2S_2$ compounds, the Bloch spectral function $A_B(E, k)$ was calculated for a certain range of the energy *E* along a path in *k*-space. In this case, the input parameters are chosen to calculate the dispersion relation $E(k)$. The energy mesh is specified by the parameters NE = 601, EMIN = 0.48 Ry, and EMAX = 0.78 Ry (E_F is ca. 0.6 Ry), while the corresponding path in k-space was specified by the number of segments of a defined *k*-path and giving all segments the first and last *k*-vectors (NK = 601). Calculating the Bloch spectral function $A_B(E, k)$ for real energies is sensible only for systems with the chemical disorder, which are usually treated using the CPA. In this case, the CPA equations must first be solved for the required energy mesh. (*The calculations were done by our collaborator, Dr. Zhongrui Li.*)

4.3 Results and Discussion

4.3.1 Structure

Figure 4.2a shows PXRD patterns of the acquired $Co_{3-x}Fe_xSn_2S_2$ polycrystals. The low Fe-doping level does not change the structure as the main phase of each Fe-substituted $Co_3Sn_2S_2$ sample is still the same shandite phase of pure $Co_3Sn_2S_2$. Only a few and very weak impurity peaks were observed, which came from the possible by-product SnS. The lattice parameters *a* and *c* refined by the Rietveld method using MAUD software are shown in Figure 4.2b. Unlike in the previous research [77, 78], where the parameter *a* became smaller and the parameter *c* became larger with the increasing concentration of Fe, I find that both parameters *a* and *c* increase with the increasing content of Fe. This is also apparent from a slight left shift in the PXRD patterns and the increase in corresponding d-spacing values calculated from $2dsin\theta = \lambda$ (see Table 4.1). This may be understood by the fact that I substituted Co atoms with larger Fe atoms, causing the lattice to expand. The exception here is the highest Fe content $Co_{2.6}Fe_{0.4}Sn_2S_2$ sample, where the parameter *a* slightly decreased, probably because the Fe solubility limit is reached. As is shown in Figure 4.2b, the ratio of the lattice parameters *c* to *a* increases with heavier Fe-doping, indicating an enhancement of the trigonal distortion in the crystalline lattice, which is caused by the anisotropy of the Fe 3d-orbitals [77].

4.3.2 Magnetic Properties

Figure 4.3a shows the zero-field-cooled (ZFC) and field-cooled (FC) temperature-dependent susceptibility χ of $Co_{3-x}Fe_xSn_2S_2$ samples measured under an applied magnetic field of 100 Oe. The magnetic susceptibility of each sample was calculated by the formula $\chi = M/(H * m)$, where M, H, and m are magnetic moment, applied field and molar mass, respectively. The sharp increase in the susceptibility of pure $Co_3Sn_2S_2$ sample near 175 K (T_C) corresponds to a paramagnetic-ferromagnetic phase transition. As the Fe-doping level increases, T_C decreases and the sample's magnetization is suppressed except for $Co_{2.6}Fe_{0.4}Sn_2S_2$, the

susceptibility of which is larger than of samples $Co_{2.7}Fe_{0.3}Sn_2S_2$ and $Co_{2.8}Fe_{0.2}Sn_2S_2$ in the low-temperature range. The precise value of the Curie temperature T_C of each sample was determined

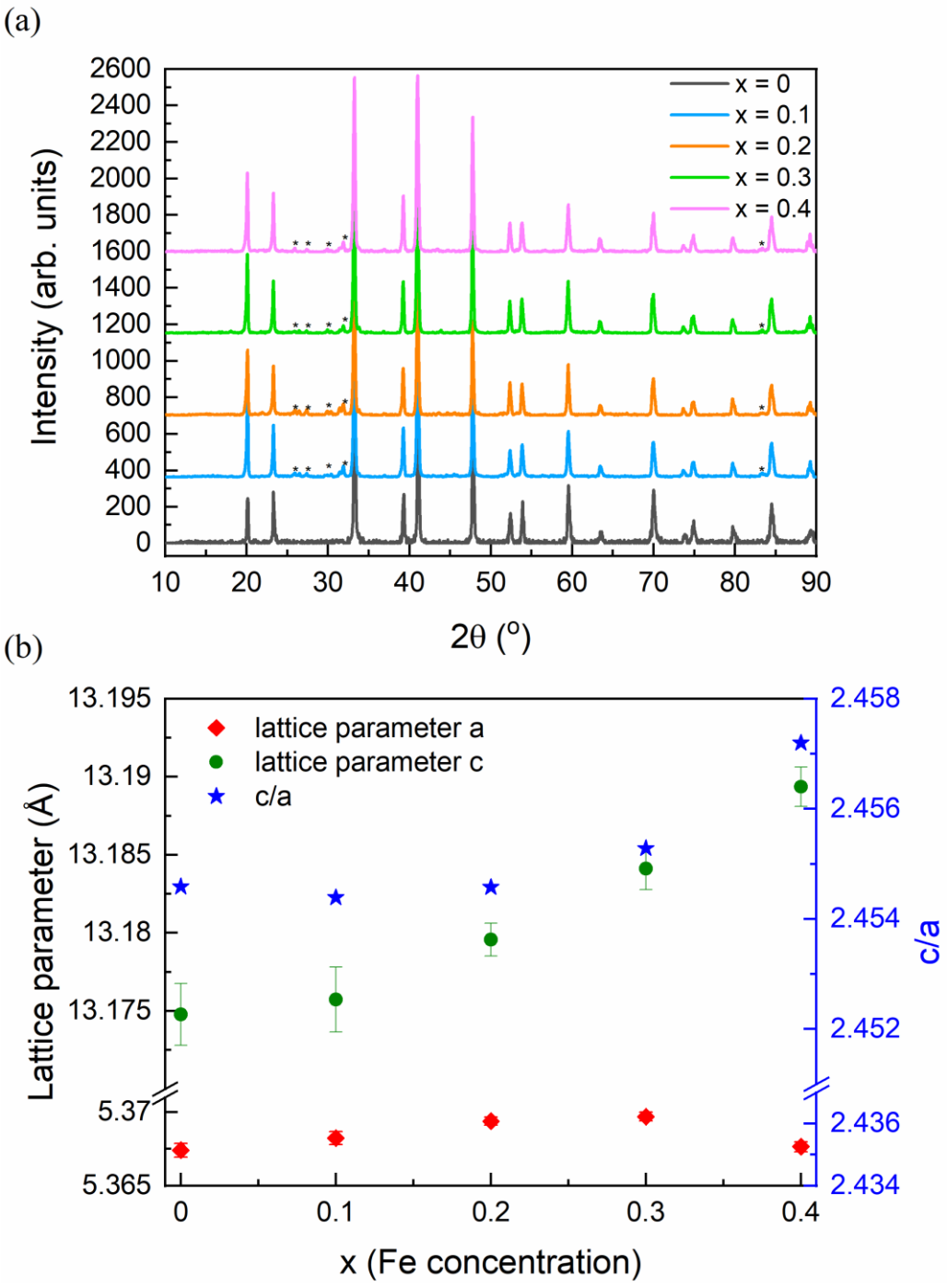

Figure 4.2: (a) Powder X-ray diffraction patterns of $Co_{3-x}Fe_xSn_2S_2$ polycrystals. Impurity peaks are marked with an asterisk. (b) Refined lattice parameters *a* and *c*, and the value of *c*/*a* plotted as a function of Fe concentration *x*.

Table 4.1: Peak positions of PXRD patterns of $Co_{3-x}Fe_xSn_2S_2$ and the corresponding Miller indices and d-spacing values. As the Fe concentration increases, a left shift of the XRD pattern happens, and d-spacing values increase. When x = 0.4, some peaks shift to the right, and the corresponding d-spacing values decrease.

	***x* = 0**		***x* = 0.1**		***x* = 0.2**		***x* = 0.3**		***x* = 0.4**	
(*h*, *k*, *l*)	2θ (°)	*d* (Å)	2θ (°)	*d* (Å)	2θ (°)	*d* (Å)	2θ (°)	*d* (Å)	2θ (°)	*d* (Å)
(0, 0, 3)	20.13208	4.4071	20.11503	4.4108	20.1035	4.4133	20.09124	4.4160	20.09418	4.4154
(0, 1, 2)	23.32276	3.8109	23.30483	3.8138	23.30139	3.8144	23.29594	3.8153	23.30043	3.8145
(1, 1, 0)	33.27567	2.6903	33.25301	2.6921	33.24393	2.6928	33.23299	2.6937	33.2433	2.6929
(0, 2, 1)	39.27583	2.2920	39.2566	2.2931	39.24037	2.2940	39.24145	2.2940	39.25719	2.2931
(2, 0, 2)	41.07189	2.1959	41.04125	2.1974	41.02538	2.1982	41.01322	2.1989	41.01212	2.1989
(0, 2, 4)	47.82436	1.9004	47.8026	1.9012	47.7835	1.9019	47.78057	1.9020	47.79352	1.9015
(2, 0, 5)	52.40634	1.7445	52.38469	1.7452	52.37031	1.7456	52.35451	1.7461	52.36331	1.7458
(1, 1, 6)	53.90212	1.6996	53.87714	1.7003	53.86342	1.7007	53.84753	1.7012	53.84739	1.7012
(2, 1, 4)	59.56304	1.5508	59.53172	1.5516	59.52126	1.5518	59.50755	1.5522	59.52489	1.5517
(0, 0, 9)	63.52463	1.4633	63.48453	1.4642	63.4618	1.4646	63.43703	1.4651	63.42058	1.4655
(2, 2, 0)	70.01015	1.3428	69.97941	1.3433	69.9634	1.3436	69.93396	1.3441	69.96895	1.3435
(2, 1, 7)	73.8532	1.2821	73.68806	1.2846	73.66317	1.2850	73.67621	1.2848	73.67011	1.2849
(1, 0, 10)	74.90493	1.2667	74.87423	1.2672	74.8597	1.2674	74.84457	1.2676	74.85508	1.2674
(1, 3, 4)	79.80894	1.2008	79.76457	1.2013	79.75413	1.2014	79.74307	1.2016	79.74923	1.2015
(2, 2, 6)	84.52947	1.1453	84.51255	1.1455	84.4899	1.1458	84.47691	1.1459	84.49149	1.1457
(4, 0, 4)	89.31211	1.0960	89.23613	1.0967	89.22084	1.0968	89.2141	1.0969	89.19488	1.0971

by the inflection point of the *dM/dT* vs *T* curve, where *M* is the ZFC magnetic moment (see Figure 4.3b). Figure 4.3c shows T_C as a function of the Fe concentration in $Co_{3-x}Fe_xSn_2S_2$ samples. The data are fitted by the second-order polynomial, which predicts that the ferromagnetic order will disappear at $x \sim 0.97$. This is close to the earlier reported experimental value $x \sim 0.8$ for single crystals samples, but significantly less than $x \sim 1.5$ for polycrystals grown by high-temperature and high-pressure techniques [77, 78]. The different values of x are likely due to different Fe concentration in the samples, amplified by the fact that the actual Fe concentration measured in each sample differs somewhat from the intended nominal concentration. As a result, predicting the critical concentration using the nominal concentration yields different results. However, the critical concentration of $x \sim 0.97$, at which ferromagnetism disappears, agrees very well with the theoretical result that the spontaneous magnetic moments in $Co_{3-x}Fe_xSn_2S_2$ samples decrease to

zero at x = 1 [78]. The fact that the Fe-doping suppresses the ferromagnetic order in $Co_3Sn_2S_2$ compounds is also predicted by DFT calculations [78]. The density of states (DOS) of $Co_{3-x}Fe_xSn_2S_2$ near the Fermi levels is dominated by the total contribution of 3d orbitals of Co and Fe atoms. When the Fe-doping level is low, the DOS of Co-3d orbitals, which shows the ferromagnetic spin-polarized state, dominates the total DOS near the Fermi level. However, when the Fe-doping level becomes high, the DOS of Fe-3d orbitals is dominant, which results in the paramagnetic spin-polarized state [78, 85]. Therefore, Fe-doping weakens the ferromagnetism of $Co_3Sn_2S_2$.

Unlike all FC curves that increase monotonically below T_C, all ZFC curves display a hump-like characteristic right below the bifurcation temperature of ZFC and FC curves. This anomaly was also observed under a low applied magnetic field in previous studies [86-89], which indicates that some other magnetic phases very likely exist besides the ferromagnetic state. Guguchia et al. used muon-spin relaxation/rotation (μSR) measurements revealing that an in-plane antiferromagnetic state emerges at temperatures above 90 K (T_C^*) in pure $Co_3Sn_2S_2$ [90]. In the temperature range from 90 K to 172 K, the out-of-plane ferromagnetic state and in-plane antiferromagnetic state co-exist. The magnetic volume fraction of the antiferromagnetic state increases as the temperature increases and reaches the maximum of 80% around 170 K. Therefore, the anomaly in the ZFC curves is likely due to the emergence of the antiferromagnetic phase. However, this anomaly appears at ~105 K in the ZFC curve of the pure $Co_3Sn_2S_2$ sample, higher than the T_C^* observed in μSR measurements. This is probably because the magnetic volume fraction of the antiferromagnetic state is pretty small at 90 K, which can only be detected by the extremely sensitive μSR technique. As the temperature increases, its fraction gradually increases, and macroscopic magnetization measurements can also detect its presence.

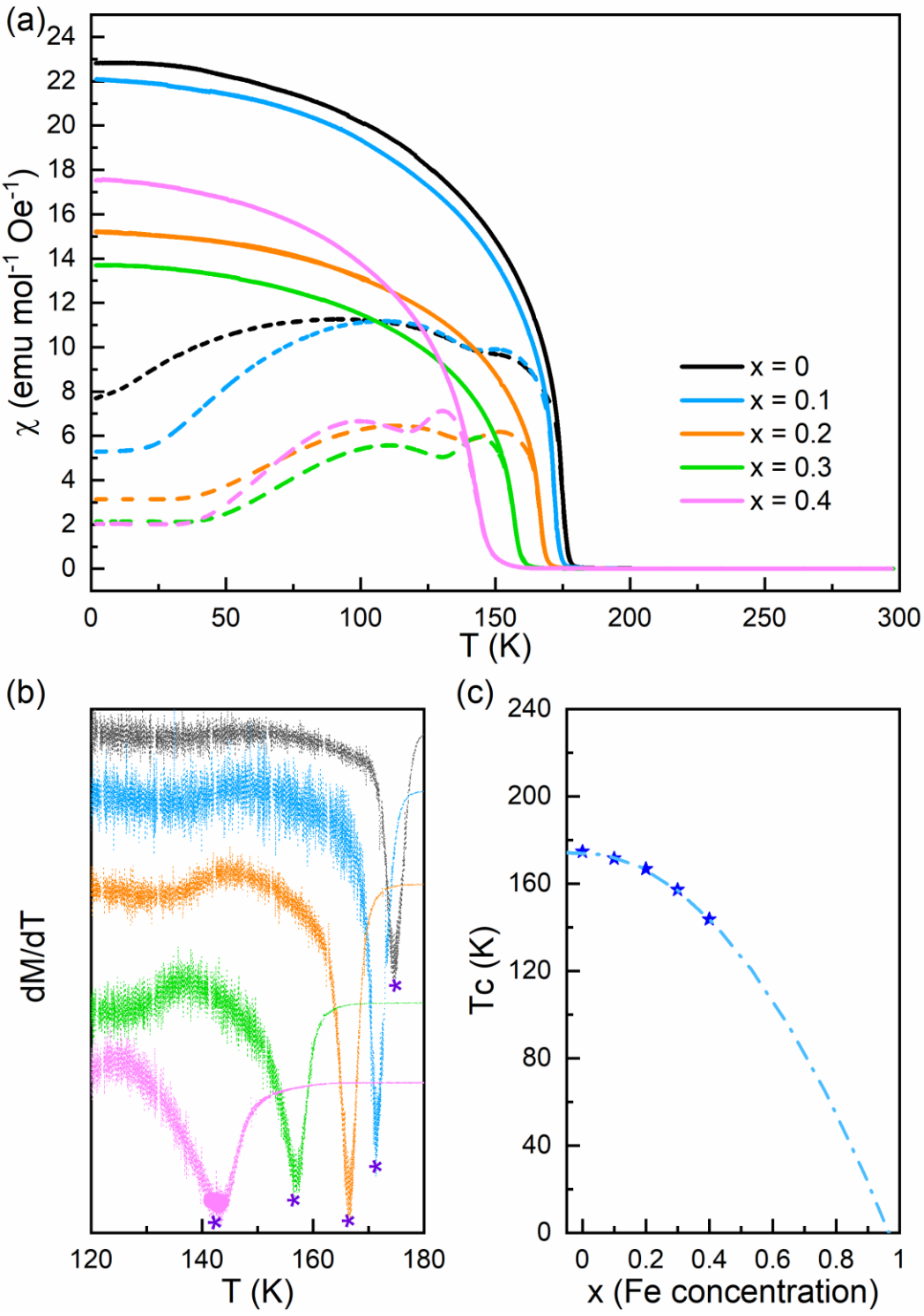

Figure 4.3: (a) Temperature-dependent susceptibility χ of $Co_{3-x}Fe_xSn_2S_2$ measured under an applied magnetic field of 100 Oe. Solid lines and dashed lines represent FC and ZFC curves, respectively. (b) Derivative of ZFC magnetic moment of $Co_{3-x}Fe_xSn_2S_2$. T_C are marked with purple asterisks. (c) T_C as a function of Fe concentration in $Co_{3-x}Fe_xSn_2S_2$. The blue extrapolated line was acquired by fitting the data points with a polynomial curve $T_C = 174.39 - 3.39x - 182.64x^2$.

Figure 4.4a and b show field-dependent magnetization *M* of all samples at 1.8 K and at 200 K, respectively. At 1.8 K, every field-dependent magnetization plot develops hysteresis due to the sample's ferromagnetism. As the concentration of Fe in the sample increases, the coercive field displays a downward trend, except for a slight rise at $x = 0.2$ following a sharp drop at $x = 0.1$. At 200 K, in the paramagnetic domain, the magnetization of each sample increases linearly with the magnetic field.

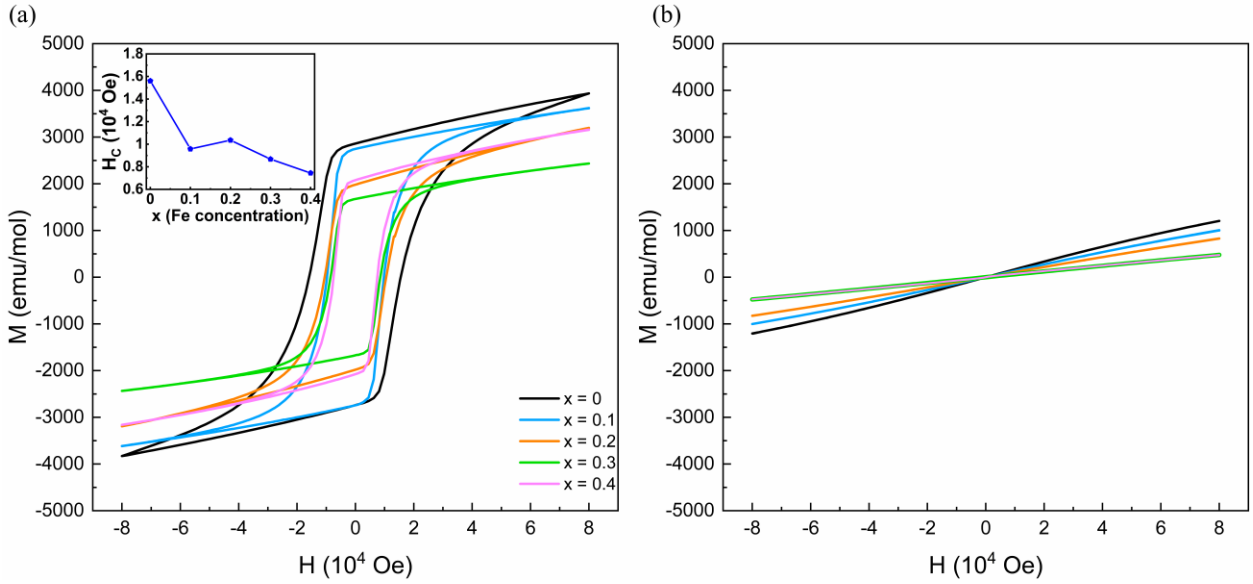

Figure 4.4: (a) Field-dependent magnetization *M* of $Co_{3-x}Fe_xSn_2S_2$ at 1.8 K. The inset shows the coercive field as a function of Fe concentration in $Co_{3-x}Fe_xSn_2S_2$. (b) Field-dependent magnetization *M* of $Co_{3-x}Fe_xSn_2S_2$ at 200 K.

4.3.3 Transport Properties

4.3.3.1 Resistivity

Figure 4.5a shows the temperature-dependent electrical resistivity of all $Co_{3-x}Fe_xSn_2S_2$ samples. $Co_3Sn_2S_2$ exhibits a metal-like behavior as the resistivity rises with the increasing temperature, and the metallic character of transport is retained in all Fe-doped samples.

With the increasing content of Fe, the resistivity increases throughout the temperature range studied, and this is especially so for the sample with x = 0.4, where the resistivity reaches a value ~ 2 mΩ cm at room temperature. This is almost an order of magnitude larger resistivity than for pure $Co_3Sn_2S_2$. The residual-resistivity ratio $RRR = \rho_{300\,K}/\rho_{1.8\,K}$ (see the inset of Figure 4.5a) decreases from 10 at x = 0 to 1.2 at x = 0.4, indicating an enhanced disorder caused by Fe doping.

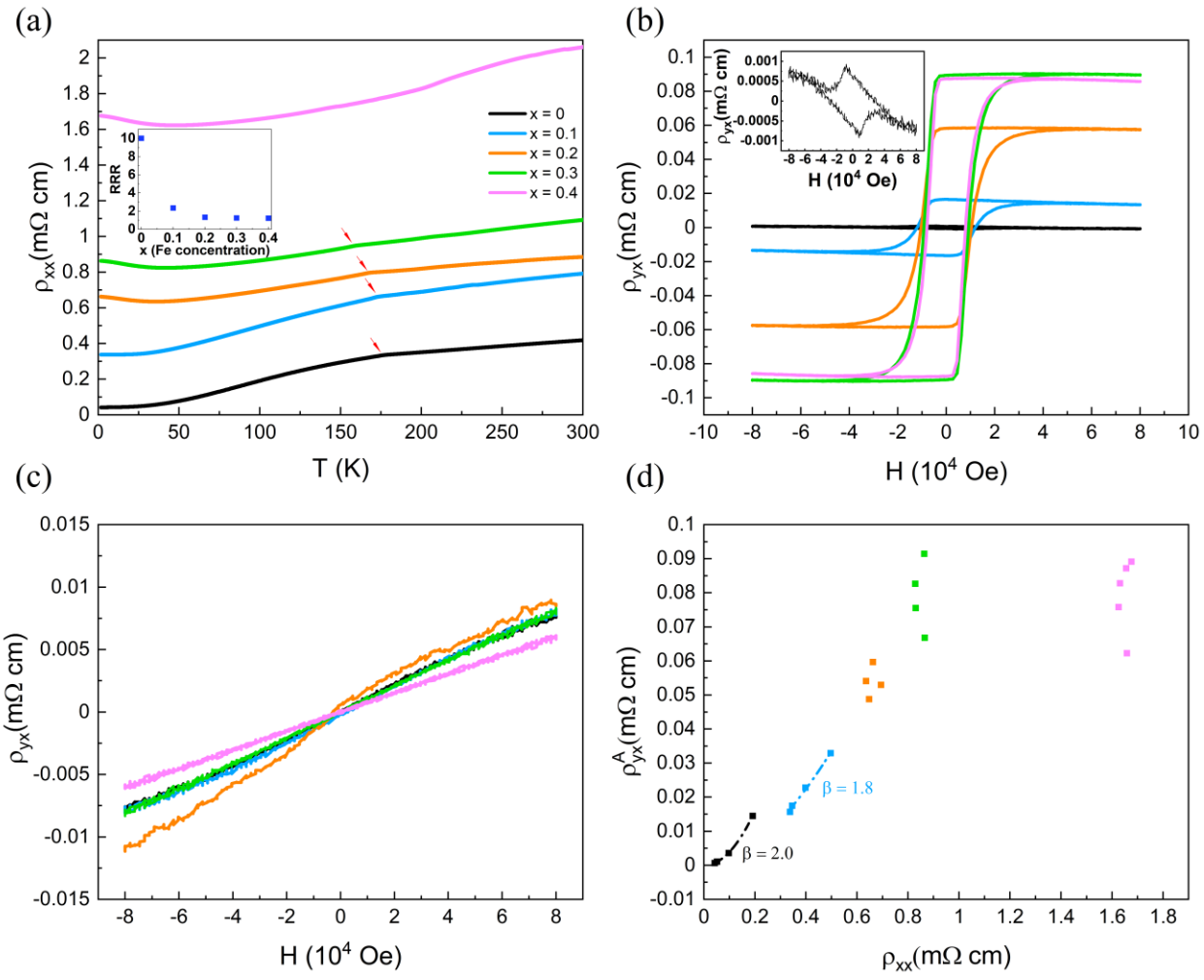

Figure 4.5: (a) Temperature-dependent electrical resistivity ρ_{xx} of $Co_{3-x}Fe_xSn_2S_2$. The kink around T_C is marked with an arrow. The inset shows RRR as a function of Fe concentration. (b) Field-dependent Hall resistivity ρ_{yx} of $Co_{3-x}Fe_xSn_2S_2$ at 1.8 K. The inset shows a zoomed-in figure of Hall resistivity ρ_{yx} for $Co_3Sn_2S_2$. (c) Field-dependent Hall resistivity ρ_{yx} of $Co_{3-x}Fe_xSn_2S_2$ at 200 K. (d) Anomalous Hall resistivity ρ_{yx}^A versus longitudinal electrical resistivity ρ_{xx}. For samples' $x \geq 0.2$, the $\rho_{yx}^A \sim \rho_{xx}^\beta$ relationship is no longer retained and the parameter β cannot be determined.

Each resistivity curve, except for the sample $Co_{2.6}Fe_{0.4}Sn_2S_2$, displays a kink around the sample's T_C, implying that the ordered magnetic state results in a smaller resistivity.

At temperatures below about 50 K, samples $Co_{3-x}Fe_xSn_2S_2$ with x = 0.2, 0.3 and 0.4 show a distinctly rising resistivity as the temperature falls. This is likely due to the Kondo effect as the doped Fe atoms act as magnetic impurities that very effectively scatter conduction electrons. The Kondo effect is characterized by a -lnT-dependent resistivity shown in Figure 4.6. At still lower temperatures, the resistivity rises more slowly, yet another feature of the Kondo effect. The Kondo temperature T_K, which is used to assess the strength of Kondo interactions, is determined by the deviation point of $-In\,T$ dependence [91, 92]. Not surprisingly, T_K increases from 11.6 K for $Co_{2.8}Fe_{0.2}Sn_2S_2$ to 12.8 K for $Co_{2.7}Fe_{03}Sn_2S_2$ and to 13.5 K for $Co_{2.6}Fe_{0.4}Sn_2S_2$ as the heavier Fe doping results in more intense Kondo scattering.

4.3.3.2 Hall resistivity

Figure 4.5b and 5c show the field-dependent Hall resistivity ρ_{yx} of $Co_{3-x}Fe_xSn_2S_2$ at 1.8 K and 200 K, respectively. The Hall resistivity $\rho_H(T,H)$ can be written as $\rho_H(T,H) = R_0H + R_sM(T,H)$, where $M(T,H)$ is the magnetization, and R_0 and R_s are the ordinary and anomalous Hall coefficients, respectively [42]. At 1.8 K, all samples are in the ferromagnetic phase, displaying a significant magnetic hysteresis. Thus, as implied by the anomalous Hall term in the equation, the Hall resistivity ρ_{yx} curve mimics the magnetization curve, indicating the occurrence of the anomalous Hall effect (AHE). At 200 K, as the magnetic order disappears, ρ_{yx} displays a linear relationship with the magnetic field. Figure 4.5d summarizes the relation between the anomalous Hall resistivity of each sample and its longitudinal electrical resistivity ρ_{xx} at several different temperatures below 100 K. The anomalous Hall resistivity ρ_{yx}^A is defined as the value of the Hall resistivity ρ_{yx} at zero field. Only for ρ_{yx}^A of $Co_3Sn_2S_2$ at 1.8 K and 30 K, I deduced its value from

the ρ_{yx} curve at zero field directly since the simultaneous existence of electron and hole carriers in the sample at low temperatures leads to a non-linear field-dependent Hall resistivity at high fields [61]. For other data points, I acquired ρ_{yx}^{A} by fitting the linear part of the ρ_{yx} curve, and

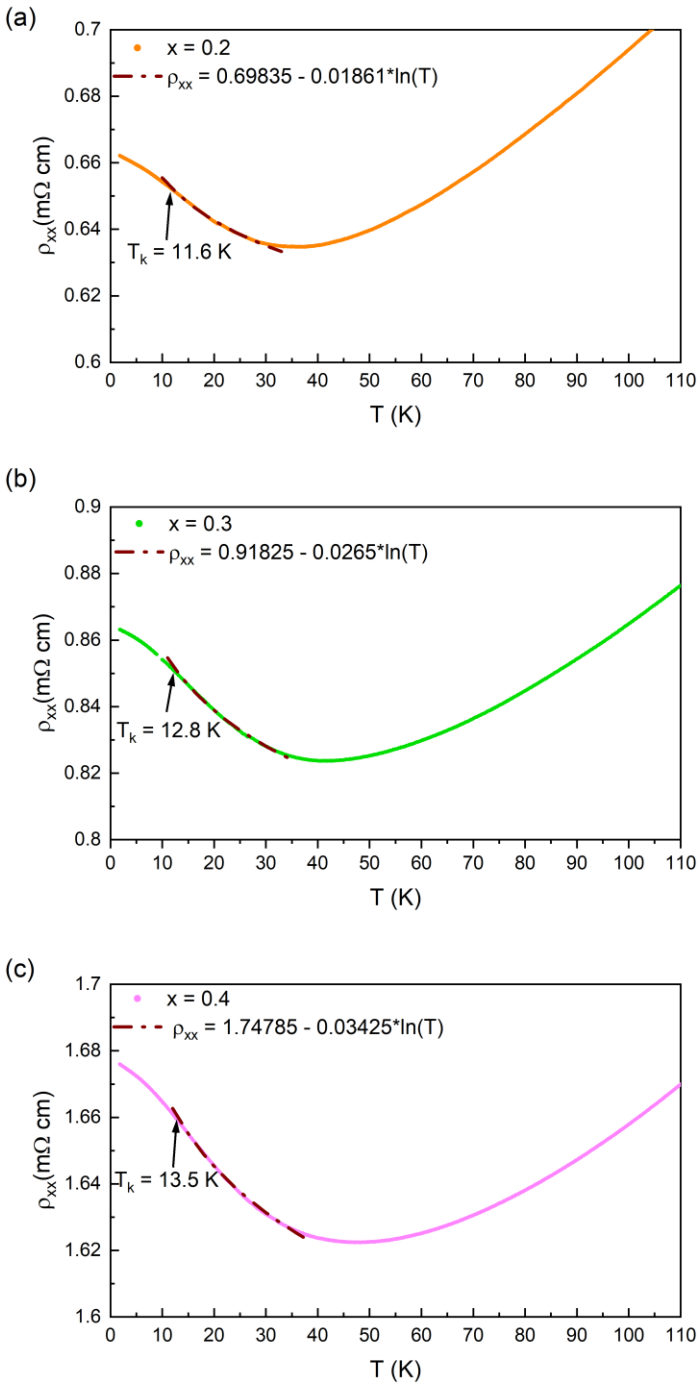

Figure 4.6: The upturn in the low temperature resistivity of $Co_{3-x}Fe_xSn_2S_2$ (x = 0.2, 0.3, and 0.4). The data below the resistivity minimum temperature are fitted by $\rho_{xx} = a - b * In\, T$.

the intercept of the linear fit line with the ρ_{yx}-axis is the value of ρ_{yx}^{A}. In order to eliminate the impact of any lead misalignment during the experiment, ρ_{yx}^{A} was corrected by $\rho_{yx}^{A} = \left(\rho_{yx}^{A}(+H) - \rho_{yx}^{A}(-H)\right)/2$, where $\rho_{yx}^{A}(+H)$ is the intercept of the linear fit of the positive field part, and $\rho_{yx}^{A}(-H)$ is that of the negative part. Generally, ρ_{yx}^{A} can be partitioned into contributions proportional to ρ_{xx} (caused by the skew-scattering contribution), and ρ_{xx}^{2} (resulting from the intrinsic and the side jump contributions). Therefore, the $\rho_{yx}^{A} \sim \rho_{xx}^{\beta}$ relationship ($1 \leq \beta \leq 2$) has been reported in many different material systems previously [42]. For pure $Co_3Sn_2S_2$ and for $Co_{2.9}Fe_{0.1}Sn_2S_2$, the data points were fitted by the formula $\rho_{yx}^{A} = \alpha\rho_{xx}^{\beta}$, where $\beta = 2.0$ for pure $Co_3Sn_2S_2$ and $\beta = 1.8$ for $Co_{2.9}Fe_{0.1}Sn_2S_2$. The AHE in $Co_3Sn_2S_2$ is caused by its large Berry curvature topologically enhanced at Weyl nodes, which is the mechanism of the intrinsic contribution to AHE [61]. Thus, in pure $Co_3Sn_2S_2$, I observe that the fitting parameter β is 2. In lightly Fe-doped samples, the intrinsic contribution still dominates the AHE because β is close to 2, as in $Co_{2.9}Fe_{0.1}Sn_2S_2$. However, because Fe atoms randomly occupy Co sites, the spin-orbit interaction induces asymmetric scattering of the conduction electrons that leads to a nontrivial skew-scattering contribution to the AHE. Consequently, β is smaller than that of the Fe-free sample. With heavier Fe-doping, i.e., for $x \geq 0.2$, the $\rho_{yx}^{A} \sim \rho_{xx}^{\beta}$ relationship is no longer retained. The Kondo effect and the strong disorder in the samples make the AHE's mechanism complex and cannot be resolved by any currently known theories.

4.3.3.3 Magnetoresistance

The transverse MR of $Co_3Sn_2S_2$ and $Co_{2.6}Fe_{0.4}Sn_2S_2$, measured under an externally applied magnetic field perpendicular to the current, is shown in Figure 4.7a and b, respectively. The MR is determined by the formula $\mathrm{MR} = (\rho_{xx}(H) - \rho_{xx}(0))/\rho_{xx}(0)$, where $\rho_{xx}(0)$ and $\rho_{xx}(H)$ are

the longitudinal resistivity at zero and H fields, respectively. $\rho_{xx}(H)$ is corrected by $\rho_{xx}(H) = (\rho_{xx}(+H) + \rho_{xx}(-H))/2$ to get rid of any influence of possible lead misalignment in the experiment, where $\rho_{xx}(+H)$ and $\rho_{xx}(-H)$ are the longitudinal resistivity measured separately at positive and negative fields. At low temperatures (below 45 K), $Co_3Sn_2S_2$ has a distinctly positive and parabolic MR. The MR diminishes as the temperature rises and, around 55 K, the MR is nearly zero and turns negative at 60 K. At 170 K, the temperature close to the transition temperature T_C, the MR reaches its highest negative value and shows a linear dependence on the field. At 200 K, where $Co_3Sn_2S_2$ is in the paramagnetic phase, the MR has a much smaller negative value but exhibits the parabolic behavior again. All MR curves show hysteresis in the low field region below T_C, which becomes more evident as the temperature increases. There are four contributions to the MR phenomenon. 1) The effective drop in the carrier velocity due to the Lorentz deflection caused by the applied magnetic field leads to a positive MR proportional to $(\mu H)^2$; 2) The magnetic moments of the sample create a fictitious field and generate an extra MR as if the applied magnetic field was present [93]; 3) Carrier scattering results from the interaction between the spins of the carriers and the applied magnetic field; 4) The thermal spin fluctuation in weakly ferromagnetic materials causes a negative MR proportional to H in the ferromagnetic phase and H^2 in the paramagnetic phase [94]. The thermal spin fluctuation mechanism dominates the MR at high temperatures, resulting in negative MR. As the temperature decreases, the Lorentz deflection mechanism gradually dominates the MR because the carrier mobility is higher at low temperatures causing a stronger deflection of the carriers [95, 96]. Thus, a shift in MR from negative to positive is observed.

Focusing on the hysteresis behavior of pure $Co_3Sn_2S_2$ in the low-magnetic field region, I find that the MR curve shows different hysteresis behavior below and above 25K (see Figure 4.8a,

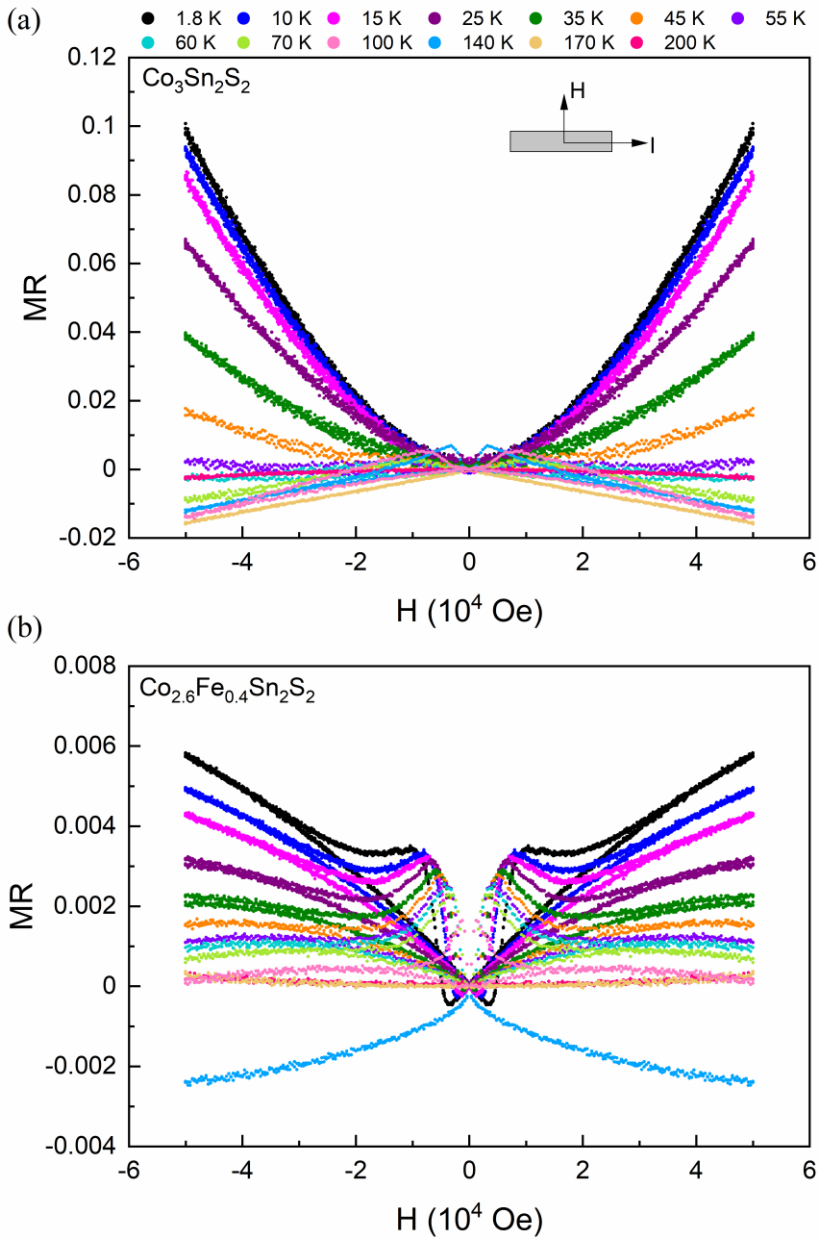

Figure 4.7: (a) Transverse magnetoresistance of $Co_3Sn_2S_2$. (b) Transverse magnetoresistance of $Co_{2.6}Fe_{0.4}Sn_2S_2$.

b, and c), which was previously seen only in nanoflake $Co_3Sn_2S_2$ samples [93]. All the MR data were collected from scans spanning from the maximum positive field to the maximum negative field and back to the maximum positive field. At low temperatures, here at 1.8 K, the blue curve in Figure 4.8a in the regime of positive fields, representing a sweep from the highest positive field,

lies above the red curve representing a sweep from the largest negative field. This trend is reversed in the domain of negative fields. This characteristic feature persists until the temperature reaches 25 K, at which point the behavior flips and is even more noticeable at 35 K. Such hysteresis behavior comes mainly from contributions 2) and 3). When the moments and the applied field are in the opposite direction, the sum of the fictitious and the applied field is smaller, resulting in a smaller MR. However, in this situation, the carrier scattering is stronger due to the sample becoming demagnetized, so the MR attributable to contribution 3) is larger. Below 25 K, contribution 2) predominates, causing a decrease in MR while the moments and the applied field are in the opposite direction. Above 25 K, the higher temperature induces a stronger carrier scattering so that contribution 3) wins the competition between the two mechanisms. Therefore, a distinct hysteresis behavior in the magnetoresistance of pure $Co_3Sn_2S_2$ is observed.

The heaviest Fe-doped sample in this study, $Co_{2.6}Fe_{0.4}Sn_2S_2$, has a MR of less than 1%, which is an order of magnitude smaller than that of the pure $Co_3Sn_2S_2$ sample (see Figure 4.7b). At temperatures below its T_C, $Co_{2.6}Fe_{0.4}Sn_2S_2$ possesses a butterfly-like MR, and the magnetic field, where maxima of the butterfly-like patterns occur, decreases as temperature increases. Because heavy Fe-doping generates a strong disorder in the $Co_{2.6}Fe_{0.4}Sn_2S_2$ sample and suppresses its magnetic order, the hysteresis in MR is mainly controlled by the carrier scattering. Even at the lowest temperature of 1.8 K, the fictitious field contribution can be detected only in low fields. When the applied magnetic field is weaker than 6000 Oe, an apparent reduction in MR happens while the moments and applied field are in the opposite direction, as illustrated in Figure 4.8d. When the field becomes stronger, the fictitious field contribution is less evident and is overwhelmed by the carrier scattering contribution. As the temperature exceeds 55 K, the effect of

the fictitious field can no longer be traced, and the hysteresis behavior is completely dominated by the carrier scattering contribution (see Figure 4.8e and f.).

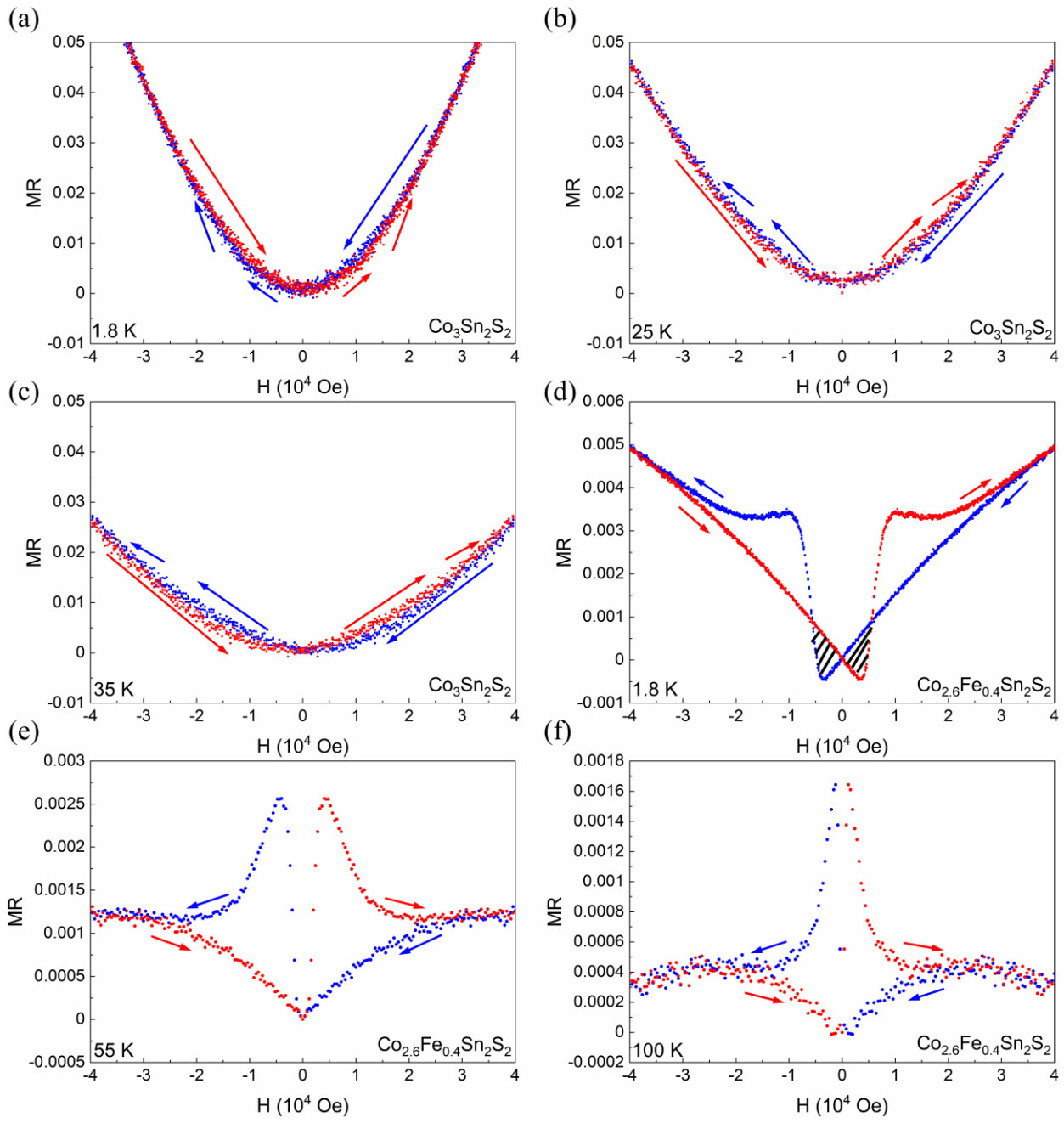

Figure 4.8: Low-magnetic field transverse magnetoresistance plot of $Co_3Sn_2S_2$ (a) at 1.8 K, (b) 25 K, and (c) 35 K. Low-magnetic field transverse magnetoresistance plot of $Co_{2.6}Fe_{0.4}Sn_2S_2$ (d) at 1.8 K, (e) 55 K, and (f) 100 K. The blue circles represent the data taken from $+5 \times 10^4$ Oe to -5×10^4 Oe (direction indicated by blue arrows), and the red circles represent the data taken from -5×10^4 Oe to $+5 \times 10^4$ Oe (direction indicated by red arrows). The shaded areas in (d) indicate the region where an apparent reduction in MR occurs due to the effect of the fictitious field.

The hysteresis behavior is also observed in longitudinal MR measurements where the externally applied magnetic field is parallel to the current. As presented in Figure 4.9a, b, and c, the trend in the blue and red curves that indicate the direction of the magnetic sweep in the longitudinal magnetoresistance of pure $Co_3Sn_2S_2$ is similar to the case of the transverse magnetoresistance shown in Figure 4.8a, b, and c. Moreover, the longitudinal magnetoresistance of $Co_{2.6}Fe_{0.4}Sn_2S_2$ also displays a clear butterfly-like pattern, Figure 4.9d, e, and f, documenting a strongly hysteretic behavior of the MR regardless of the orientation of the magnetic field. This is expected in polycrystalline samples.

One of the peculiar transport phenomena in Weyl semimetals is the negative longitudinal magnetoresistance, which is caused by the chiral anomaly [97]. However, both $Co_3Sn_2S_2$ and $Co_{2.6}Fe_{0.4}Sn_2S_2$ show positive longitudinal MR at low temperatures (see Figure 4.10). Although the longitudinal MR of $Co_3Sn_2S_2$ and $Co_{2.6}Fe_{0.4}Sn_2S_2$ turns negative at 60 K and 140 K, respectively, this is more likely owing to the thermal spin fluctuation, which can also result in negative MR, as seen in the transverse MR measurements. The absence of the negative longitudinal MR could be attributed to the significant orbital MR in samples [98]. Even if the applied external magnetic field is parallel to the current, out-of-plane moments in samples form a fictitious field that acts like an applied magnetic field perpendicular to the current, giving rise to a large orbital MR and concealing the phenomenon of negative longitudinal magnetoresistance [93].

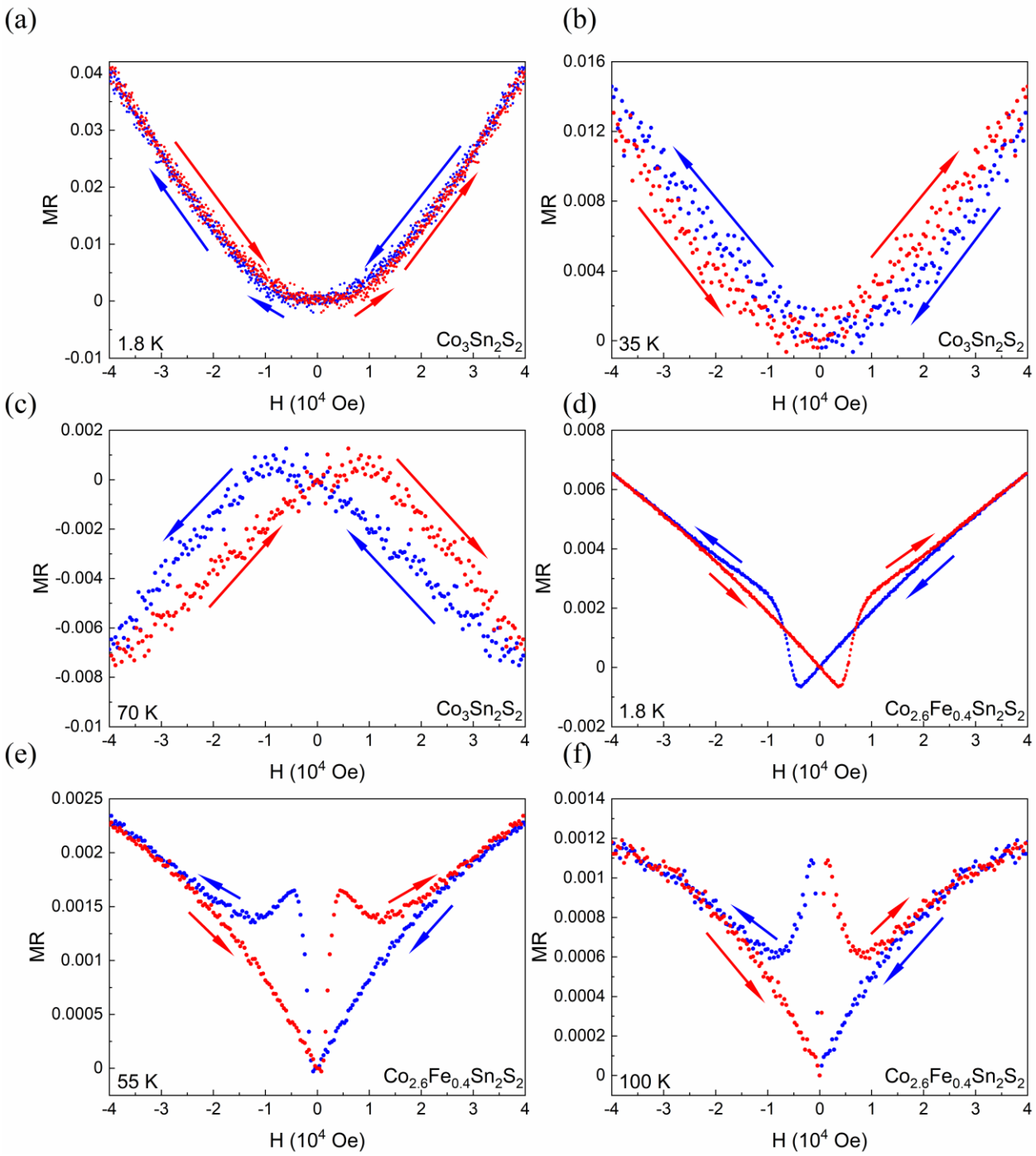

Figure 4.9: Low-magnetic field longitudinal magnetoresistance plot of $Co_3Sn_2S_2$ (a) at 1.8 K, (b) 25 K, and (c) 35 K. Low-magnetic field longitudinal magnetoresistance plot of $Co_{2.6}Fe_{0.4}Sn_2S_2$ (d) at 1.8 K, (e) 55 K, and (f) 100 K. The blue circles represent the data taken from $+5 \times 10^4$ Oe to -5×10^4 Oe (direction indicated by blue arrows), and the red circles represent the data taken from -5×10^4 Oe to $+5 \times 10^4$ Oe (direction indicated by red arrows). The shaded areas in (d) indicate the region where an apparent reduction in MR occurs due to the effect of the fictitious field.

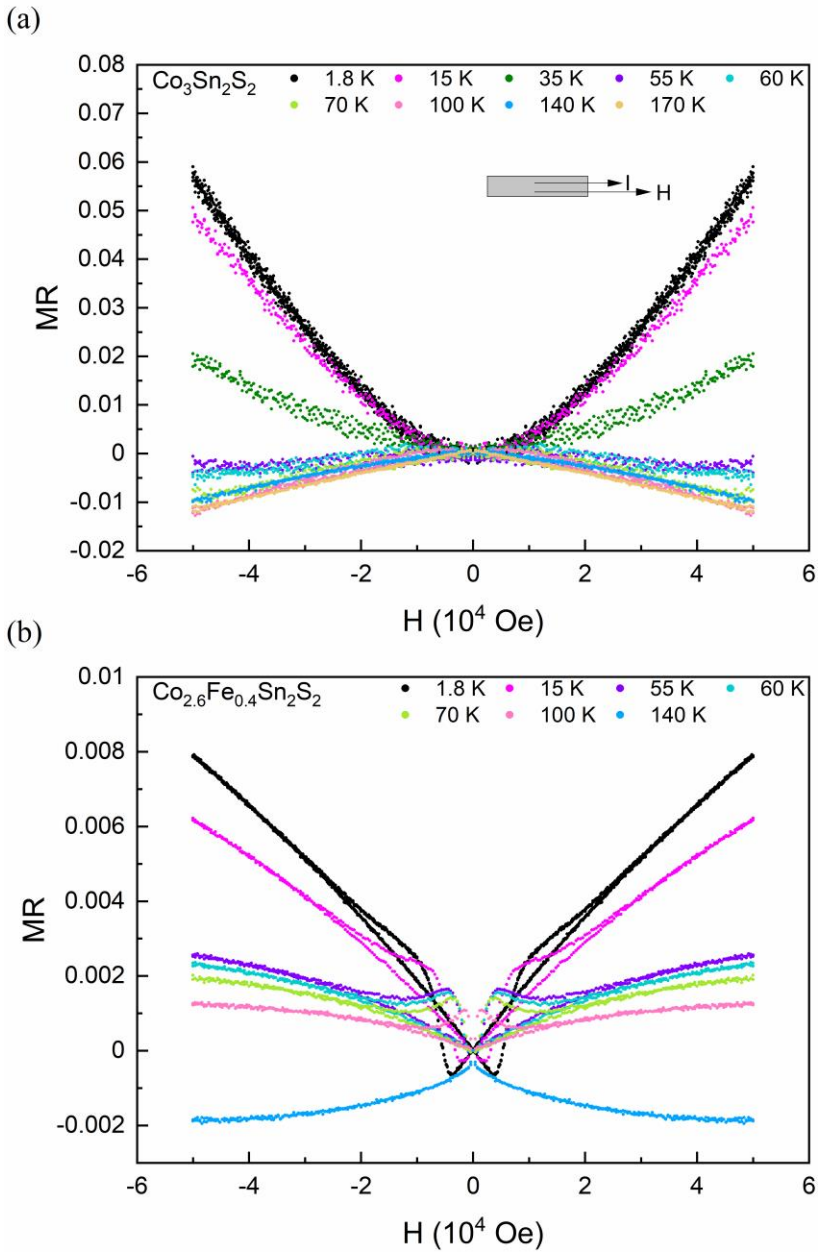

Figure 4.10: (a) Longitudinal magnetoresistance of $Co_3Sn_2S_2$. (b) Longitudinal magnetoresistance of $Co_{2.6}Fe_{0.4}Sn_2S_2$.

4.3.3.4 Heat capacity

Figure 4.11a shows the heat capacity c_p of $Co_{3-x}Fe_xSn_2S_2$ between 2 K and 10 K. It is evident that Fe-doping increases the sample's heat capacity. At low temperatures, heat capacity can generally be described by a power law dependence $c_p(T) = AT^{\alpha(T)}$, where A is a certain

prefactor, and $\alpha(T)$ is a temperature-dependent index characterizing the degree of change in heat capacity versus temperature [99]. For a set of experimental data points, $\alpha(T)$ is estimated by $\alpha(T) = In\frac{C_2}{C_1}/In\frac{T_2}{T_1}$, where $T = (T_1 + T_2)/2$ and T_1 and T_2 are temperatures corresponding to heat capacities C_1 and C_2, respectively [99]. Figure 4.11b plots the index $\alpha(T)$ of each sample below 10 K. There is no significant difference between $\alpha(T)$ values of different samples at the same temperature. At 10 K, $\alpha(T) \approx 3$, indicating that the phonon contribution dominates the heat capacity. As the temperature decreases, $\alpha(T)$ decreases monotonically, and at 2 K, $\alpha(T) \approx 1$, suggesting that the electron contribution gradually dominates and controls the sample's heat capacity at lower temperatures.

To extract further information, the heat capacity data are fitted with equation $c_p/T = \gamma + \beta T^2$, where γ is the Sommerfeld coefficient, β is the coefficient of phonons [100], and T is the temperature (see Figure 4.11c). It should be pointed out that the magnetic contribution to the heat capacity is ignored here. According to the Weiss model, the magnetic contribution to the specific heat of ferromagnetic materials is proportional to dM^2/dT, where M is the magnetization and T is the temperature [100]. Therefore, the magnetic contribution follows a general trend of being small at low temperatures and starting to rise rapidly as the Curie temperature T_c is approached [100]. In **section *4.3.2***, I mentioned that $Co_{3-x}Fe_xSn_2S_2$ samples have a T_c of at least 143 K. Hence, it is reasonable to overlook the magnetic contribution at the lowest temperatures. The values of γ and β, as well as the Debye temperature [100] θ_D of each sample derived from the corresponding β parameter, are summarized in Table 4.2. Pristine $Co_3Sn_2S_2$ has the Sommerfeld coefficient of 11.2 mJ mol^{-1} K^{-2} and the Debye temperature of 375.4 K, which agrees with the previous report [101]. It is clear that doping with Fe increases both γ and β values, although the γ values for x = 0.1 and x = 0.2 seem not to conform to the trend. Because the electronic specific heat is proportional to the

DOS at the E_F [100], the larger γ value of the sample with a higher Fe concentration means the higher DOS at the E_F. This conclusion is in line with the computational results discussed later. The larger β value observed in the sample with a higher Fe concentration indicates that it has a lower θ_D. The θ_D is the temperature of a crystal's highest normal mode of vibration [102], and grain

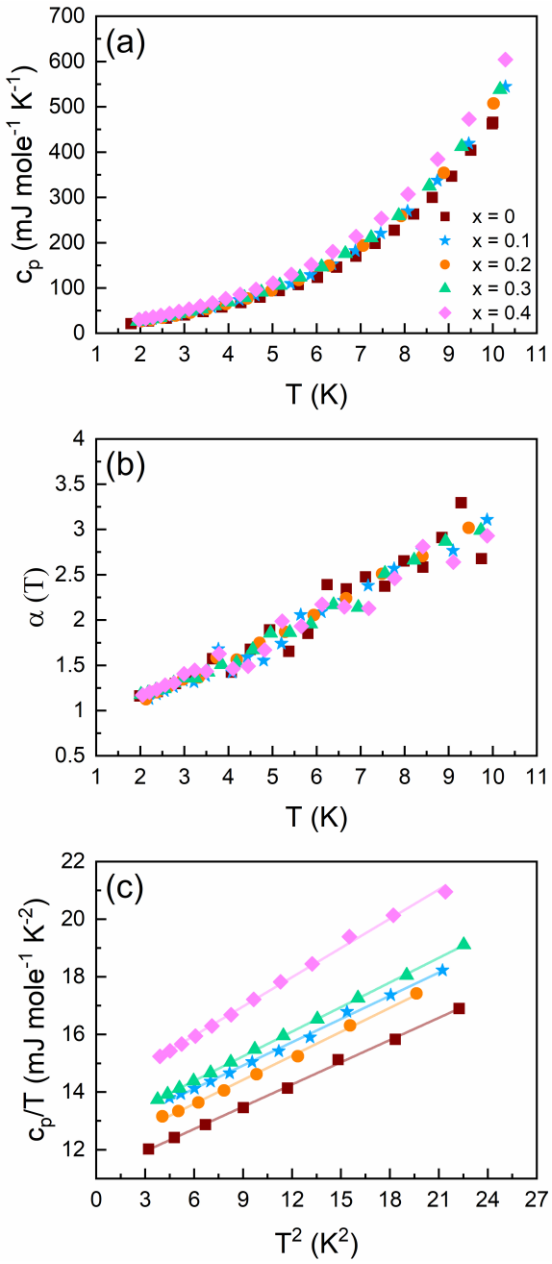

Figure 4.11: (a) Heat capacity c_p of $Co_{3-x}Fe_xSn_2S_2$. (b) The temperature-dependent index $\alpha(T)$ of $Co_{3-x}Fe_xSn_2S_2$. (c) c_p/T versus T^2 plot. The heat capacity data are fitted with equation $c_p/T = \gamma + \beta T^2$. The fitting parameters γ and β are summarized in Table 4.2.

boundaries, defects, impurities, and disorders can somewhat reduce the value of θ_D [103]. Thus, the impurities and disorders induced by Fe-doping may be the cause of the decreasing θ_D. Generally, a sample with a lower θ_D is expected to have a lower thermal conductivity [104]. This is true for my samples, as seen in the following section.

Table 4.2: Fe concentration *x*, Sommerfeld coefficient γ, calculated DOS at the Fermi level (E_F), fitting coefficient β, and Debye temperature θ_D.

x (Fe concentration)	$\gamma\ (mJ\ mol^{-1}\ K^{-2})$	DOS $(States\ eV^{-1})$	$\beta\ (mJ\ mol^{-1}\ K^{-4})$	$\theta_D\ (K)$
0	11.2	1.64	0.257	375.4
0.1	12.5	2.21	0.269	369.9
0.2	11.9	2.47	0.278	366.0
0.3	12.7	2.56	0.285	362.9
0.4	13.9	2.67	0.338	342.7

4.3.3.5 Seebeck Coefficient and Thermal Conductivity

The temperature-dependent Seebeck coefficient *S* of $Co_{3-x}Fe_xSn_2S_2$ under a zero external magnetic field is shown in Figure 4.12a. All samples have a negative Seebeck coefficient in the measured temperature range, indicating that the dominant carriers are electrons, consistent with the reported computational and experimental results [68, 105]. As the temperature falls, the absolute value of the Seebeck coefficient, $|S|$ first decreases linearly, showing the sample's metallic character, and then exhibits a kink near the sample's Curie temperature T_c due to the lower entropy state caused by the magnetic ordering and hence the suppression of $|S|$ [106]. As the temperature drops further, the $|S|$ of $Co_3Sn_2S_2$ and $Co_{2.9}Fe_{0.1}Sn_2S_2$ displays a local maximum at temperatures around 40 K. This anomaly on the Seebeck coefficient of samples with $x = 0$, $x = 0.1$, as well as the hint of it on sample $x = 0.2$, is likely due to the phonon drag effect that is wiped out at higher Fe concentrations. As the temperature approaches 0 K, all *S* curves converge to 0, as expected by the Nernst's theorem. By utilizing the electrical resistivity data, the power factor $PF =$

S^2/ρ of each sample is calculated and plotted in Figure 4.12b. For $Co_3Sn_2S_2$ and $Co_{2.9}Fe_{0.1}Sn_2S_2$, the *PF* curve exhibits a broad maximum at about 40 K, corresponding to the local maximum of $|S|$. Even though Fe-doping clearly enhances $|S|$ at temperatures above 120 K, *PF* is significantly decreased in Fe-doped samples due to their larger electrical resistivity arising from the stronger carrier scattering caused by the Fe-doping-induced disorder.

Figure 4.12c shows the temperature-dependent thermal conductivity κ of $Co_{3-x}Fe_xSn_2S_2$ under a zero magnetic field. The κ of pure $Co_3Sn_2S_2$ initially rises as temperature decreases, reaches a peak of 8.7 W K^{-1} m^{-1} at 40 K, and then starts to decrease and converges to 0. The κ of Fe-doped samples displays a similar pattern, however the presence of Fe dramatically reduces the sample's ability to conduct heat. The highest Fe content sample, $Co_{2.6}Fe_{0.4}Sn_2S_2$, has its maximum κ of approximately 2.7 W K^{-1} m^{-1}, some three times lower value than pure $Co_3Sn_2S_2$. The dimensionless figure of merit, $zT = S^2\rho^{-1}\kappa^{-1}T$, where S is the Seebeck coefficient, ρ is the electrical resistivity, and κ is the thermal conductivity, is calculated for each sample and is depicted in Figure 4.12d. In spite of the fact that Fe-doping significantly suppresses κ and increases $|S|$ above 120 K, it also results in considerably larger electrical resistivity at the same time. Therefore, I only see a slight improvement in the thermoelectric performance in $Co_{2.7}Fe_{0.3}Sn_2S_2$ and $Co_{2.6}Fe_{0.4}Sn_2S_2$ compared to the pristine $Co_3Sn_2S_2$ in a very narrow temperature range, 120 K ~ 160 K. This is remarkably different from the behavior at temperatures above room temperature, where the zT is claimed [69] to increase with the increasing Fe concentration and the enhancement in the Seebeck coefficient weighs over the reduction in the electrical conductivity. However, it needs to be pointed out that my Fe-doped samples, especially $Co_{2.7}Fe_{0.3}Sn_2S_2$ and $Co_{2.6}Fe_{0.4}Sn_2S_2$, have larger electrical resistivity and lower thermal conductivity at room temperature than that reported in this high-temperature research paper [69].

This perhaps can be explained by the different qualities of the studied polycrystals. Since I used a different polycrystal synthesis method, the grain size, domain structure, and actual elements concentration may differ, which can affect the samples' transport properties.

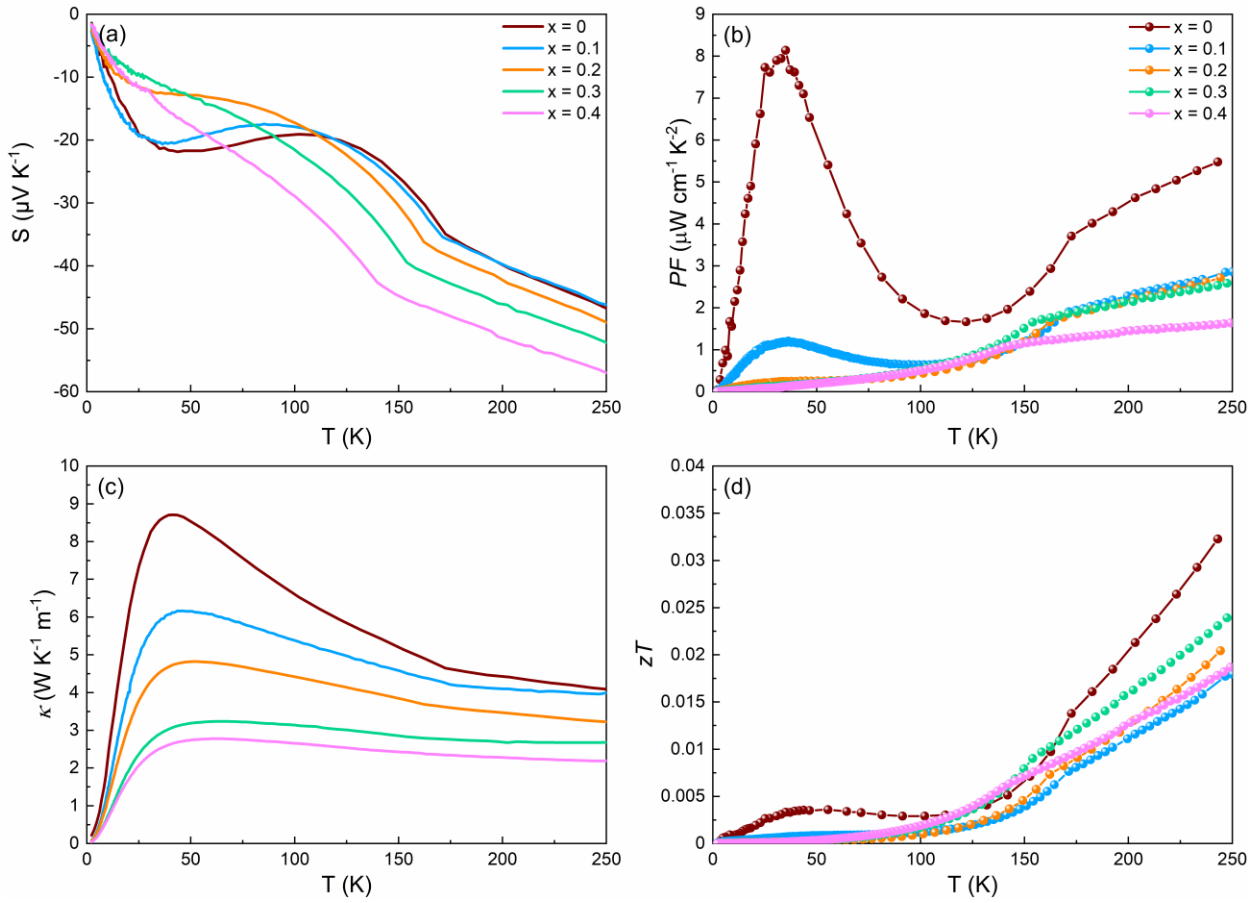

Figure 4.12: Temperature-dependent (a) Seebeck coefficient *S*, (b) power factor *PF*, (c) thermal conductivity κ, and (d) figure of merit *zT* of $Co_{3-x}Fe_xSn_2S_2$ under a zero external magnetic field.

The earlier theoretical works [107-109] predicted that, unlike in traditional thermoelectric materials whose thermoelectric performance is almost unchanged under the magnetic field, the external magnetic field could significantly impact the thermoelectric properties of Dirac/Weyl semimetals due to their unique band structures. Thus, I also studied the influence of the external magnetic field applied parallel to the temperature gradient on the Seebeck effect *S* and thermal conductivity κ of pristine $Co_3Sn_2S_2$ and $Co_{2.8}Fe_{0.2}Sn_2S_2$. As shown in Figure 4.13a, the applied

magnetic field significantly suppresses $|S|$ of $Co_3Sn_2S_2$ near its T_c = 174 K, and the kink at this temperature disappears in both 5×10^4 Oe and 1.1×10^5 Oe curves. This effect is also observed in $Co_{2.8}Fe_{0.2}Sn_2S_2$ (see Figure 4.14a). In the temperature range 70 K ~ 130 K, the situation is reversed, here the magnetic field results in a slight increase in $|S|$ of $Co_3Sn_2S_2$. The field-dependent change in S of $Co_3Sn_2S_2$ (Figure 4.13b) provides a clearer picture. At 171 K, $|S|$ decreases as the magnetic field increases, and it is reduced by about 10% under a field of 1.4×10^5 Oe. At 101 K, $|S|$ increases as the magnetic field increases, and it is raised by about 5.6% under a field of

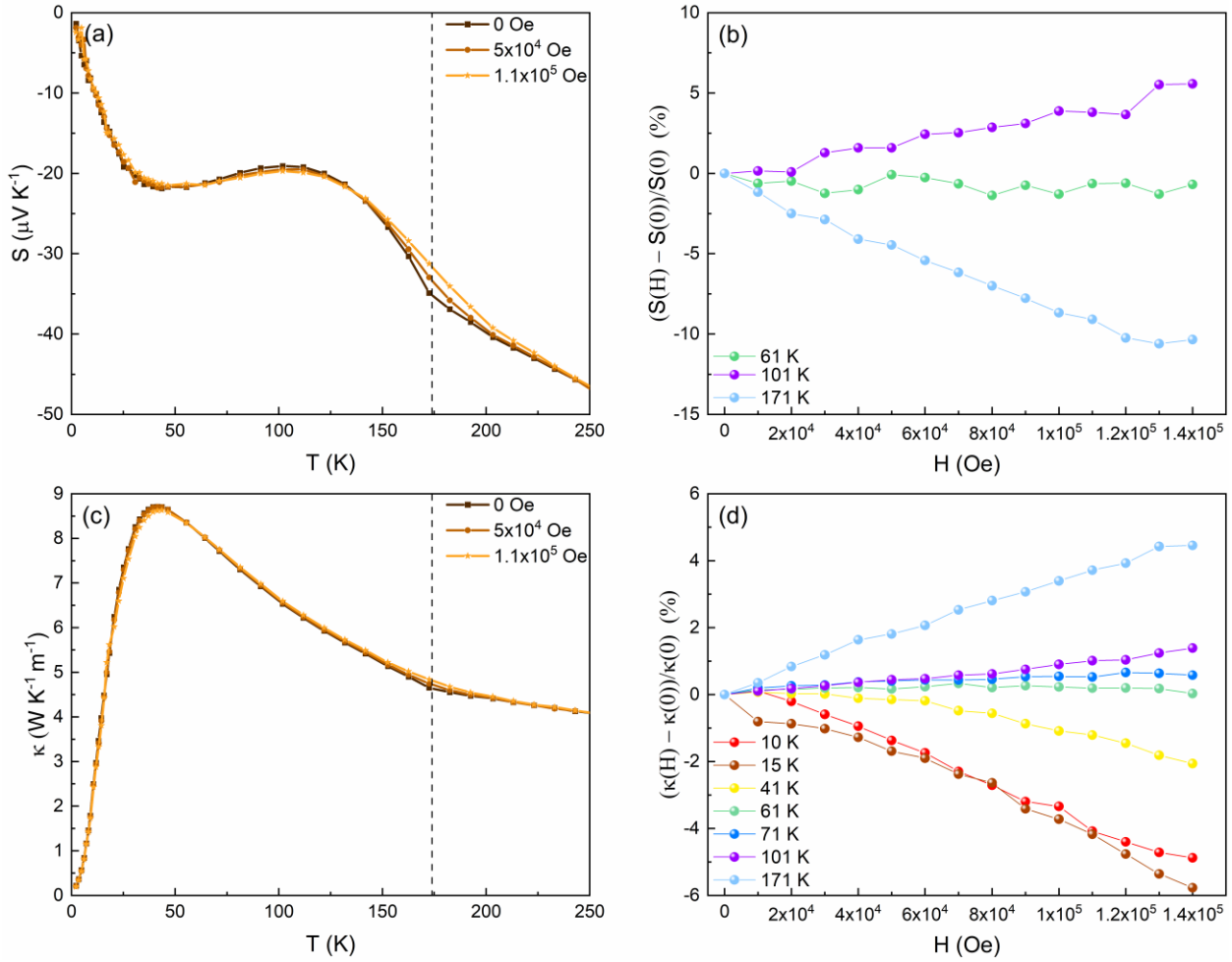

Figure 4.13: Temperature-dependent (a) Seebeck coefficient S and (c) thermal conductivity κ of pristine $Co_3Sn_2S_2$ under the applied magnetic field of 0 Oe, 5×10^4 Oe, and 1.1×10^5 Oe. The Curie temperature of $Co_3Sn_2S_2$, T_c = 174 K, is indicated by the dashed line. Magnetic field-dependent change in (b) S and (d) κ of $Co_3Sn_2S_2$ at different temperatures. The magnetic field is parallel to the temperature gradient in all these measurements.

1.4×10^5 Oe. At 61 K, S is essentially unaltered by the applied magnetic field. The suppression of $|S|$ near T_c can be attributed to the field-induced suppression of the thermal spin fluctuation. In a ferromagnetic material, the spin entropy is small at low temperatures and increases sharply when reaching close to T_c, exhibiting a steplike profile near T_c. If the d-orbital electrons are itinerant or partially itinerant, the behavior of the spin-entropy contribution to S is analogous to that of the spin entropy since S can be thought of as the entropy transferred per charge carrier [110]. At temperatures close to T_c, the spin entropy decreases significantly under a strong external magnetic field, because the thermal spin fluctuation is suppressed. Thus, $|S|$ reduces in the vicinity of T_c under applied magnetic fields. This spin fluctuation-related phenomenon has been observed in many other ferromagnetic materials, such as MnSi, $Fe_2V_{0.9}Cr_{0.}1Al_{0.9}Si_{0.1}$, $Fe_{2.2}V_{0.8}Al_{0.6}Si_{0.4}$, and $A Fe_4Sb_{12}$ (A = Ca, Sr, Ba) [110-112].

Figure 4.13c depicts the temperature-dependent κ of pristine $Co_3Sn_2S_2$ under the applied magnetic field of 0 Oe, 5×10^4 Oe, and 1.1×10^5 Oe. Starting from the temperature around T_c, κ is increased by the applied magnetic field. As the temperature falls, this increase becomes unnoticeable. At about 60 K, κ is almost unchanged by the magnetic field. As the temperature drops further, κ exhibits a decrease under the magnetic field, which is especially obvious around the peak temperature, 40 K. However, $Co_{2.8}Fe_{0.2}Sn_2S_2$ does not clearly display these features (See Figure 4.14b). To get a closer look at the influence of the applied magnetic field on κ, the field-dependent change in κ of $Co_3Sn_2S_2$ at different temperatures are plotted in Figure 4.13d. Above 61 K, κ increases as the magnetic field increases. Under the field of 1.4×10^5 Oe, the increases in κ are about 4.5%, 1.4%, and 0.6% at 171 K, 101 K, and 71 K, respectively. At 61 K, κ is basically unaffected by magnetic fields. Below 61 K, κ decrease as the magnetic field increases, and in the field of 1.4×10^5 Oe, it is reduced by about 2.1%, 5.8%, and 4.9% at 41 K, 15 K, and

10 K, respectively. It is worth pointing out that I observed a similar trend in the field-dependent magnetoresistance of $Co_3Sn_2S_2$, where above about 60 K, the magnetoresistance was negative while below 60 K it turned positive (see **section *4.3.3.3***). This is intuitively reasonable. In general, κ can be partitioned into two contributions: the lattice thermal conductivity κ_L and the electronic thermal conductivity κ_e. The heat transport by phonons is usually independent of the applied magnetic field [113]. Thus, κ_L can be regarded as a constant under the varying magnetic field. After applying an external magnetic field, if the MR is negative,

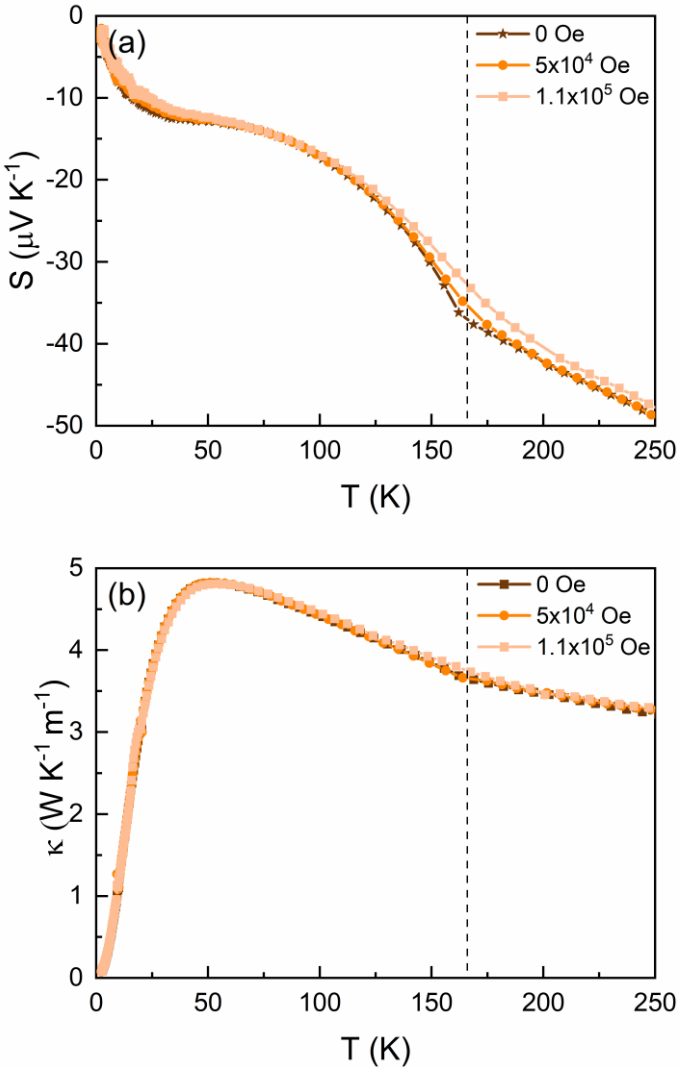

Figure 4.14: Temperature-dependent (a) Seebeck coefficient *S* and (b) thermal conductivity κ of $Co_{2.8}Fe_{0.2}Sn_2S_2$ under the applied magnetic field of 0 Oe, 5×10^4 Oe, and 1.1×10^5 Oe. The Curie temperature of $Co_{2.8}Fe_{0.2}Sn_2S_2$, T_c = 166 K, is indicated by the dashed line. The magnetic field is parallel to the temperature gradient in both measurements.

κ_e increases due to the reduced electrical resistivity, and if the MR is positive, κ_e is diminished since the electrical resistivity increases.

I also explored the influence of the external magnetic field applied perpendicular to the temperature gradient on the S and κ of pristine $Co_3Sn_2S_2$. Nevertheless, as presented in Figure 4.15, the results are very similar to that in Figure 4.13a and c. There is no noticeable difference brought on by the transverse magnetic field. It is worth emphasizing that samples measured in this work are polycrystals and some physical properties respond to the applied magnetic field less noticeably than single crystal samples would. For example, the magnetoresistance (MR) of the $Co_3Sn_2S_2$ sample is about 10% in a magnetic field of 5×10^4 Oe at 2 K, while a single crystal sample can reach a value of ~25% under the same conditions [98]. Currently, the common synthesis method of single crystalline $Co_3Sn_2S_2$ is the flux method, and the acquired sample is a very thin sheet with a diameter of ~ 4 mm [77]. Although this size is good enough for the magnetic and electrical transport measurements, it is too small to obtain reliable thermal transport data with acceptable errors. To further explore the thermal transport properties of $Co_3Sn_2S_2$ under the applied magnetic field, a strategy for growing large single crystals is needed.

4.3.4 Computational results

In the last section of this chapter, I present the computational results. The spin-polarized DOS of $Co_{3-x}Fe_xSn_2S_2$ obtained from the full-potential KKR-Green's function calculations is displayed in Figure 4.16a. For the pristine $Co_3Sn_2S_2$, the spin-up band shows metallic characters, while the spin-down channel has an energy gap of about 0.3 eV, consistent with the reported value [114]. The material clearly exhibits a half-metallic nature. Fe-doping mainly affects the DOS near the Fermi level (E_F). As the concentration of Fe increases, the band gap in the spin-down structure shrinks, and the DOS of the spin-up counterpart shows a noticeable

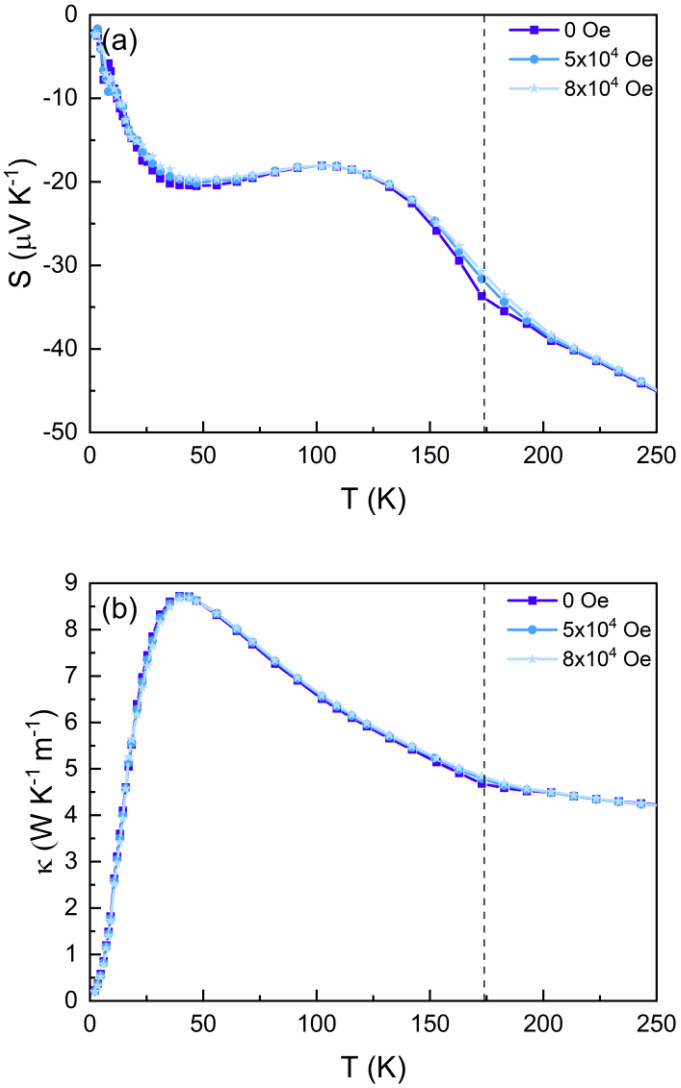

Figure 4.15: Temperature-dependent (a) Seebeck coefficient S and (b) thermal conductivity κ of $Co_3Sn_2S_2$ under the applied magnetic field of 0 Oe, 5×10^4 Oe, and 8×10^4 Oe. The Curie temperature of $Co_3Sn_2S_2$, T_c = 174 K, is indicated by the dashed line. The magnetic field is perpendicular to the temperature gradient in both measurements.

increase in the range between -0.7 eV and -0.4 eV, and also a slight increase at the E_F (see Figure 4.16b and Table 4.2). The DOS at the E_F is dominated by the contributions of Fe and Co atoms. Figure 4.16c shows that at the concentration of x = 0.1, the DOS of Co atoms at the E_F attains its largest value. As the content of Fe increases, the DOS of Co atoms at the E_F marginally decreases. At the same time, as the content of Fe increases, the DOS of Fe atoms at the E_F increases (see Figure 4.16d) and overshadows the decrease in the DOS of Co atoms, resulting in the overall

increase in the total DOS at the E_F. To confirm the validity of the above computation, a KKR+DMFT approach [84] was employed as an alternative method for calculating the DOS. As seen in Figure 4.17, both methods yield a very similar result.

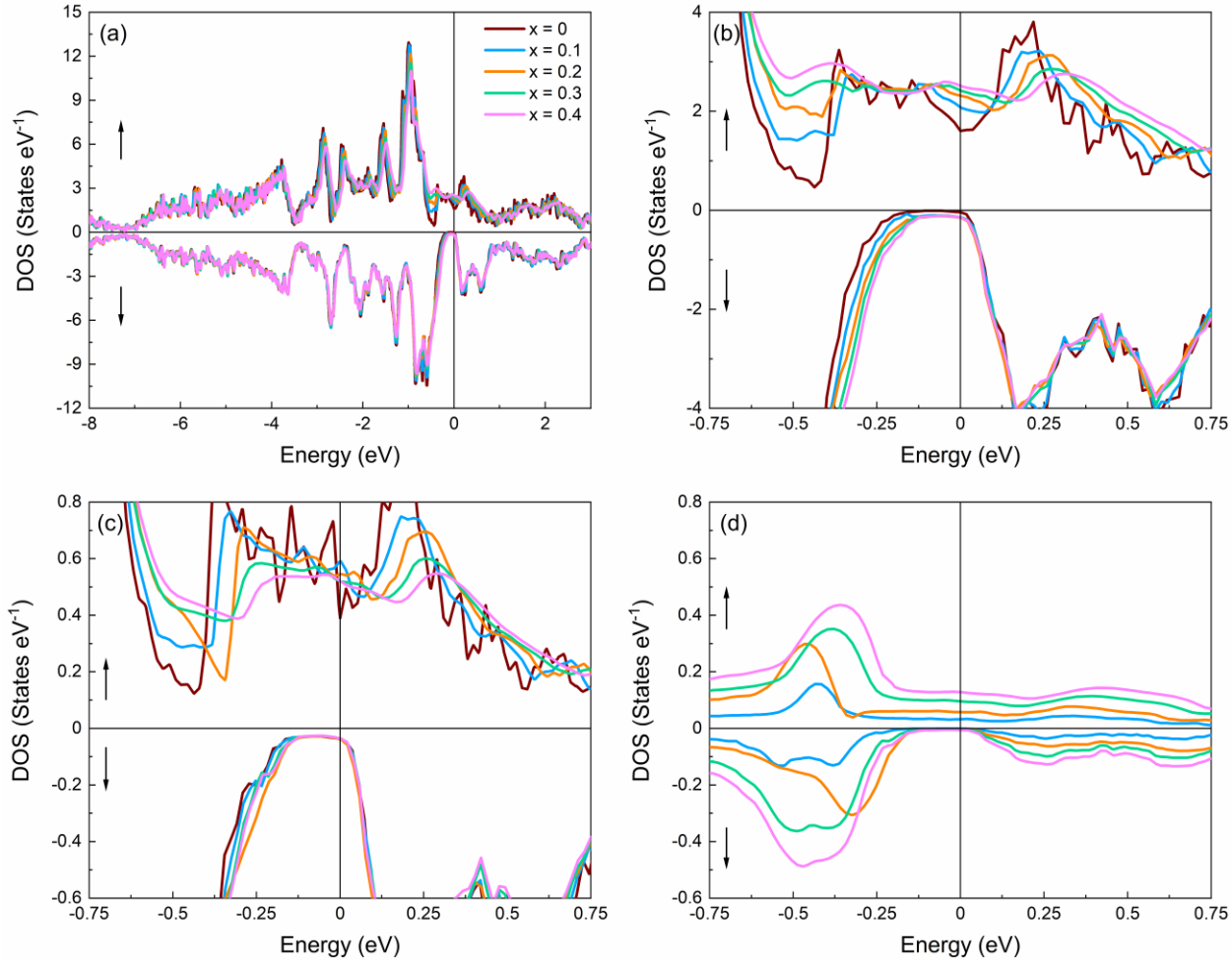

Figure 4.16: (a) DOS of $Co_{3-x}Fe_xSn_2S_2$. (b) Enlarged plots of the DOS of $Co_{3-x}Fe_xSn_2S_2$ near the Fermi level (E_F). The contributions of (c) Co atoms and (d) Fe atoms to the DOS of $Co_{3-x}Fe_xSn_2S_2$ near the E_F. The E_F is set at 0 eV. As indicated by upward (downward) arrows, the upper (lower) half plots denote the spin-up (spin-down) DOS.

Regarding the band structure change under the influence of Fe-doping, the Bloch spectral function $A_B(E, k)$ is adopted, which can be seen as a k-resolved DOS function and be obtained from Fourier transformed of the real-space Green's function. As for an ordered system, it is a δ-like

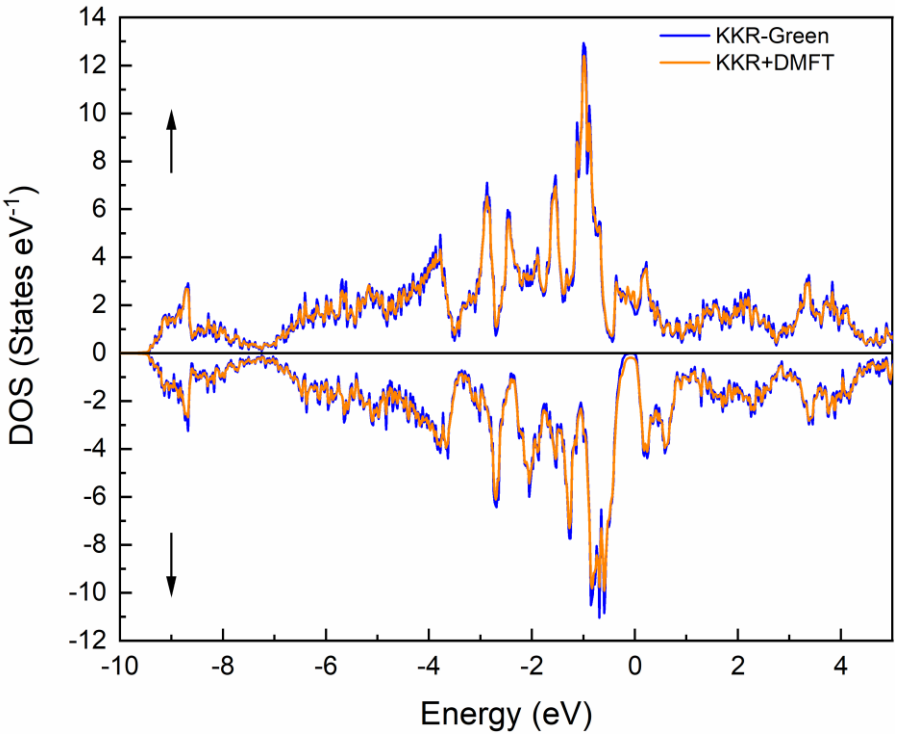

Figure 4.17: The DOS of pristine $Co_3Sn_2S_2$ obtained using KKR-Green's function and KKR+DMFT methods. The Fermi level (E_F) is set at 0 eV. As indicated by an upward (downward) arrow, the upper (lower) half plot denotes the spin-up (spin-down) DOS.

function that carries the same information as the dispersion relation $E(k)$. Calculating $A_B(E, k)$ for an ordered system at complex energies is, therefore, an alternative way to represent $E(k)$, with a broadening according to the imaginary part of E. For a disordered system, $E(k)$ is not well defined, while $A_B(E, k)$ can still be used to represent the electronic band structure. As seen in Figure 4.18, the offset connected with a Block spectral function is due to the disorder in the Fe-doped system. Due to the low Fe-doping concentration, some dispersion relations remain. Hence, one can see these relations in the doped systems, especially the s and p states, which are less important as they are typically far from E_F. However, in some regimes, the dispersion relations are more smeared out, which are mainly d states near E_F and more important in the energy regime. In other words, the k-vector is a good quantum number for an ordered state but is not a good quantum number for

a disordered state. There are some physical meanings revealed by broadening of the Bloch spectrum function. For example, one can derive a lifetime from the width of these curves by using a group velocity. This information is usually needed for transport calculations using the Boltzmann or Kubo-Greenwood equation [115, 116].

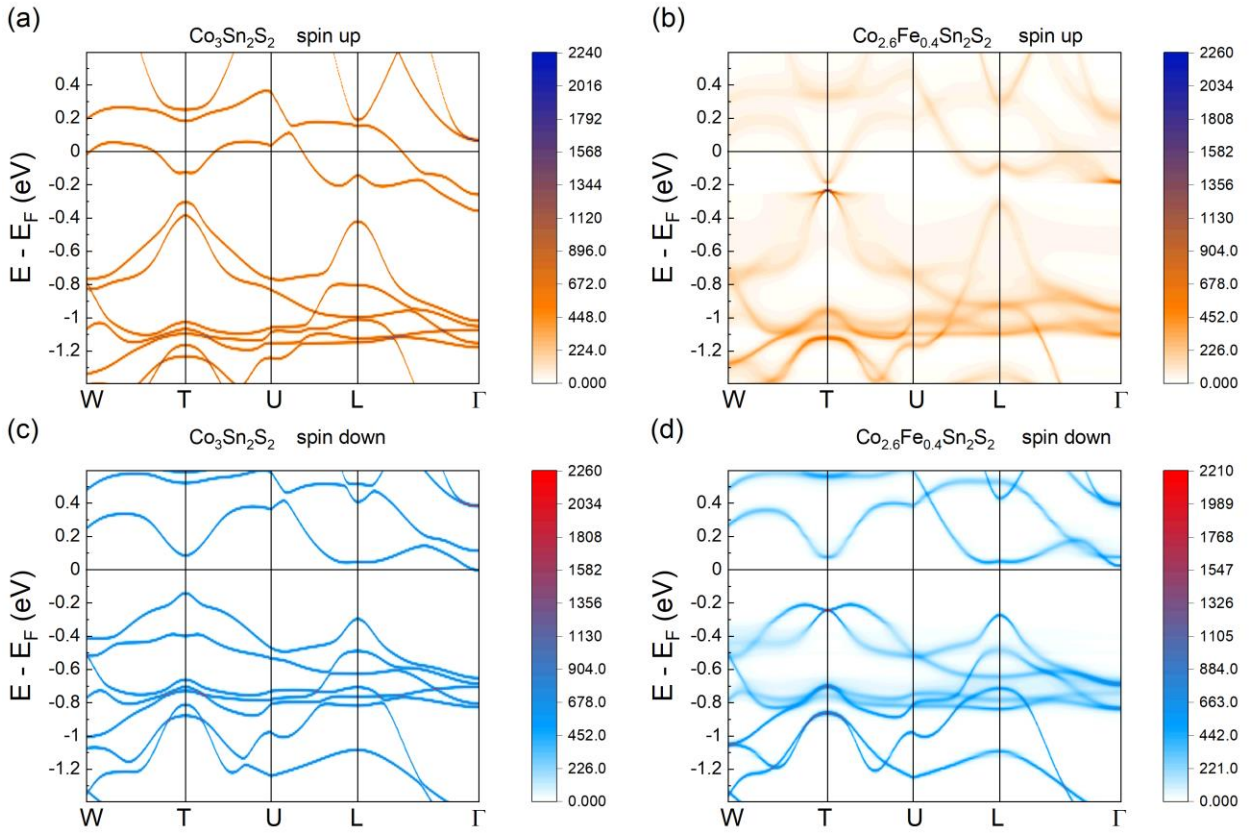

Figure 4.18: The spin-resolved Block spectral functions of pristine $Co_3Sn_2S_2$ (a) spin-up (c) spin-down and $Co_{2.6}Fe_{0.4}Sn_2S_2$ (b) spin-up (d) spin-down. The amplitude is given by the color code.

The formation energy of materials, which represents the energy required to dissociate the material into its individual components, has great significance in judging their stability. The formation energy of $Co_{3-x}Fe_xSn_2S_2$ systems was calculated from the conventional total energy. The relative formation energy of doped systems relative to that of pure system $Co_3Sn_2S_2$ is displayed in Figure 4.19. The positive formation energy of the Fe-doped systems compared to the pristine

one indicates that the doping-induced chemical disorder introduces instability to the structure of pristine $Co_3Sn_2S_2$. Up to x = 0.3, the increase in the formation energy is still very small, but a big jump was observed at the Fe doping concentration of x = 0.4. This aligns with the Fe solubility limit of around x = 0.5 at ambient conditions [77].

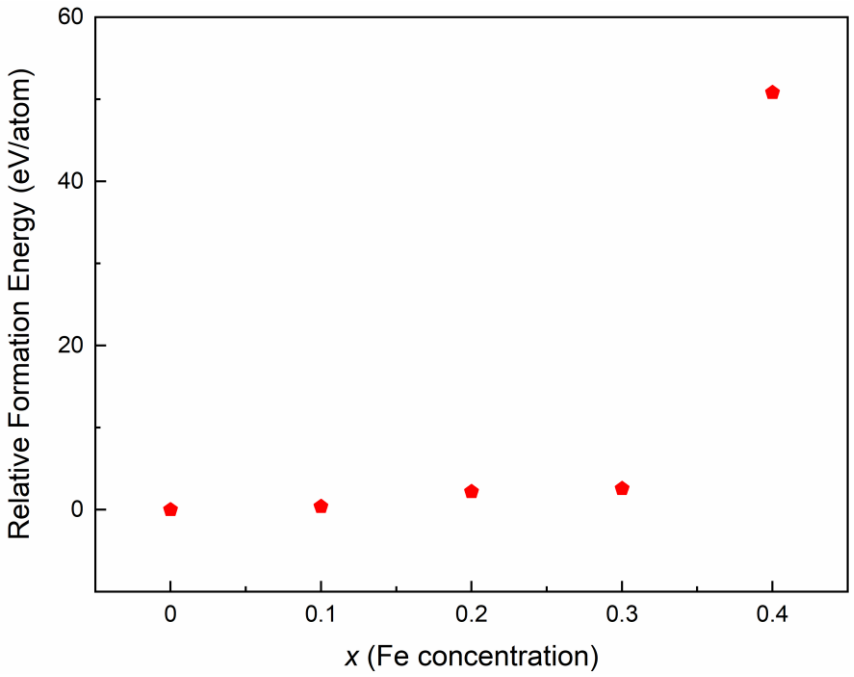

Figure 4.19: The relative formation energy of $Co_{3-x}Fe_xSn_2S_2$ as compared to $Co_3Sn_2S_2$.

4.4 Conclusion

In this work, I demonstrate the effect of Fe-doping on magnetic and transport properties of $Co_3Sn_2S_2$. Fe-doping suppresses the ferromagnetic order and decreases the coercive field extracted from the magnetization curves. The suppression of the magnetic order is mainly due to the paramagnetic spin-polarized state of DOS of Fe-3d near the Fermi level. Right below T_C, all ZFC curves display an anomaly, which is likely due to the emergence of the antiferromagnetic phase. At a low Fe-doping level, the anomalous Hall resistivity is still dominated by the intrinsic

contribution originating from $Co_3Sn_2S_2$'s large Berry curvature, displaying the robustness of the topological origin of the AHE. However, with heavier Fe-doping, in addition to the skew-scattering, the strong disorder and the Kondo effect observed in electrical resistivity measurements make the AHE much more complicated to analyze, leaving it for future studies. Fe-doping largely decreases the MR of $Co_3Sn_2S_2$, but the non-saturating character is retained. The hysteresis in the MR at low magnetic fields below T_C, which was found previously only in nanoflakes, is reported here for the first time in bulk samples, showing the competition and concurrence of the magnetic-moment-induced fictitious field and the carrier scattering contribution to the MR.

The low-temperature thermal and thermoelectrical properties, such as heat capacity, Seebeck coefficient, and thermal conductivity, were also studied. By fitting the low-temperature heat capacity data, it is demonstrated that as Fe concentration increases, the sample's Debye temperature decreases, and its density of states at the Fermi level increases, which is confirmed by the computational results calculated using the full-potential KKR-Green's function method. The Seebeck coefficient of $Co_{3-x}Fe_xSn_2S_2$ is negative in the measured temperature range, 2 K ~ 250 K, and the Fe-doping evidently enhances the absolute value of the Seebeck coefficient at temperatures above 120 K. Meanwhile, the thermal conductivity is notably suppressed by the Fe-doping. However, the power factor and the zT value are not enhanced by the Fe-doping because it strongly enhances the electrical resistivity at the same time. I also show how the external applied magnetic field influences the thermal transport properties of $Co_3Sn_2S_2$. Under the applied magnetic field, the Seebeck coefficient and thermal conductivity exhibit different behaviors in the different temperature ranges. However, a large single crystal may be needed to document a more evident effect of the magnetic field. Overall, I conducted detailed investigations on low-temperature magnetic and transport properties Fe-doped $Co_3Sn_2S_2$ polycrystals. I hope that this work can serve

as a reference and inspire future research on $Co_3Sn_2S_2$ and other compounds in the shandite family. This work was published in references [117, 118].

Chapter 5 Extremely Large Magnetoresistance and Quantum Oscillations in Semimetal $Ni_3In_2S_2$

5.1 Motivation

Magnetoresistance (MR) is not only a fundamental topic in condensed matter physics but is also crucial to industrial applications. Large MR materials can be used to develop magnetic field sensors, random access memories, galvanic isolators, and read heads [119]. Magnetic materials are typically the main focus of searches for materials with a high MR. In recent years, the discovery of non-magnetic topological semimetals, such as Cd_3As_2, WTe_2, and $MoTe_2$, having a MR of more than 10^3, offers a new perspective on understanding and looking for materials with a large MR. Several mechanisms, such as electron-hole compensation and linear dispersion-induced high mobility, have been proposed to account for the large MR in these materials [18, 28].

Ternary chalcogenide $Ni_3In_2S_2$ is a recently identified topological semimetal with endless Dirac-nodal lines, which displays a large transverse MR at low temperatures. In this work, I show that the transverse MR in single crystalline $Ni_3In_2S_2$ reaches a giant value of ~ 24 000% at 2 K and 14 T. In the meanwhile, a magnetic field-induced resistivity upturn behavior at low temperatures is observed, which is strongly correlated to the large MR. Moreover, below 50 K, the magnetoresistance curves show a linear magnetic field dependence under high magnetic fields. All these findings can be ascribed to the linearly dispersive electronic bands of $Ni_3In_2S_2$. I will first present the transport measurement results and then combine them with computations and de Haas–

van Alphen quantum oscillation results to explain the occurrence of the extremely large MR in $Ni_3In_2S_2$ and the crucial role of the linear dispersions.

5.2 Methods

5.2.1 Experimental Methods

Single crystal $Ni_3In_2S_2$ was synthesized by the solid-state reaction method as previously reported [120]. Stoichiometric amounts of high-purity sulfur pieces, indium shots, and nickel powder were put into an alumina crucible. The crucible was then sealed in a quartz tube under vacuum. The quartz tube was placed in the box furnace and heated to 1000 ℃ in 20 h with a dwell time of 36 h. After that, it was slowly cooled to 500 ℃ with a rate of 2 ℃/h. Then, the tube was naturally cooled down to room temperature by turning off the furnace power. The acquired crystal could be easily cleaved into smaller pieces mechanically, and the cleavage plane is silver, shining, and mirror-like. A piece of crystal was ground into powder, and its crystal structure was examined by powder X-ray diffraction using a Rigaku Ultima IV X-ray diffractometer (Cu $K\alpha$). The orientation of the cleavage plane was determined by the single-crystal X-ray diffraction measurement using the same diffractometer. The chemical compositions of the crystal were checked by energy-dispersive X-ray spectrometry (EDS).

Magnetotransport properties, heat capacity, and magnetic torque were measured in a Physical Property Measurement System (PPMS Dynacool, Quantum Design) under magnetic fields up to 14 T and temperatures down to 2 K. The torque measurements were performed on a piezoresistive cantilever mounted on the PPMS rotator sample puck. The vacuum grease was used to mount the sample onto the cantilever.

5.2.2 Computational Method

The Electronic structure calculations of $Ni_3In_2S_2$ crystal were performed using the full-potential augmented-plane-wave + local orbital (APW + LO) method in the framework of density functional theory (DFT), as implemented in the ELK code [121]. Exchange and correlation effects were treated with the revised generalized gradient approximation for solids (the Perdew-Burke-Ernzerhof functional) [82]. Spin-orbit coupling was found to have an insignificant impact on the electronic structure of $Ni_3In_2S_2$ near the Fermi level (see Figure 5.1) and was therefore excluded in the present calculations. Regular Monkhorst-Pack grids of k points, typically a 16 × 16 × 16 k-point mesh in the irreducible wedge, were used for the Brillouin-zone sampling. The lattice constants used in the calculations were $a = b = 5.37$ Å and $c = 13.56$ Å [122]. The fermiology of

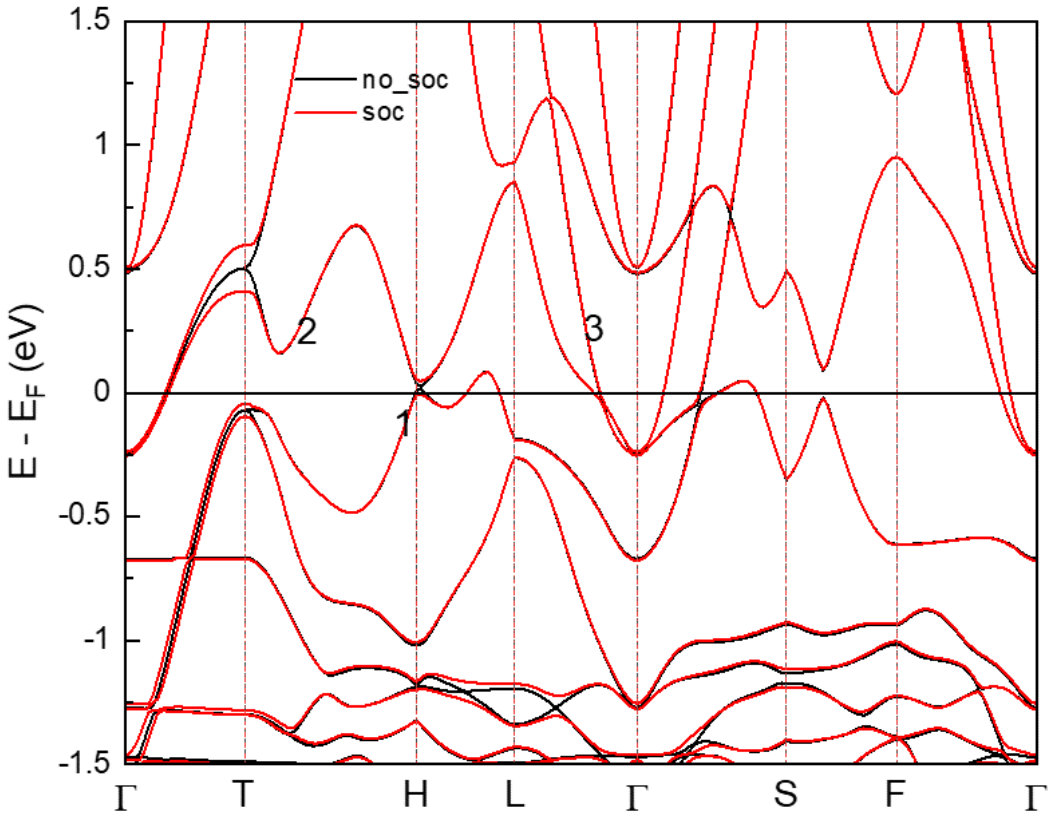

Figure 5.1: Band structure of $Ni_3In_2S_2$ with and without SOC. SOC has a negligible effect on the bands near the Fermi level, except it opens a slight gap of 0.185 eV on Band 2 at the symmetry point T.

the $Ni_3In_2S_2$ crystal was investigated using de Haas-van Alphen quantum oscillations. The quantum oscillation frequency and the effective mass of the $Ni_3In_2S_2$ crystal were extracted from the calculated Fermi surface by employing a Supercell K-space Extremal Area Finder (SKEAF) program [123]. (*The calculations were done by our collaborator, Dr. Zhongrui Li.*)

5.3 Results and Discussion

5.3.1 Crystal Structure

$Ni_3In_2S_2$ crystallizes in a hexagonal lattice shandite structure with the space group No.166 ($R\bar{3}m$). Its conventional unit cell is shown in Figure 5.2a, which is drawn using the VESTA software [54]. As seen in Figure 5.2b, Ni atoms form a 2D Kagomé lattice within Ni-In(2) layers perpendicular to the *c*-axis. Figure 5.2c plots the powder X-ray diffraction (PXRD) pattern of the powder acquired by grinding the single crystal. Compared to the PXRD pattern generated by the previously reported data_415258 in the ICSD database [124], I confirm that the sample crystallizes in the shandite structure, and no second phase is detected. The single-crystal X-ray diffraction measurement result (Figure 5.2d) indicates that the cleavage plane of the crystal used for the transport measurements is perpendicular to the *c*-axis of the hexagonal conventional unit cell. The chemical composition of the sample determined by EDS is $Ni_3In_2S_{2.1}$, demonstrating that the crystal is almost precisely stoichiometric given that the accuracy of the EDX measurement is only within a few wt%.

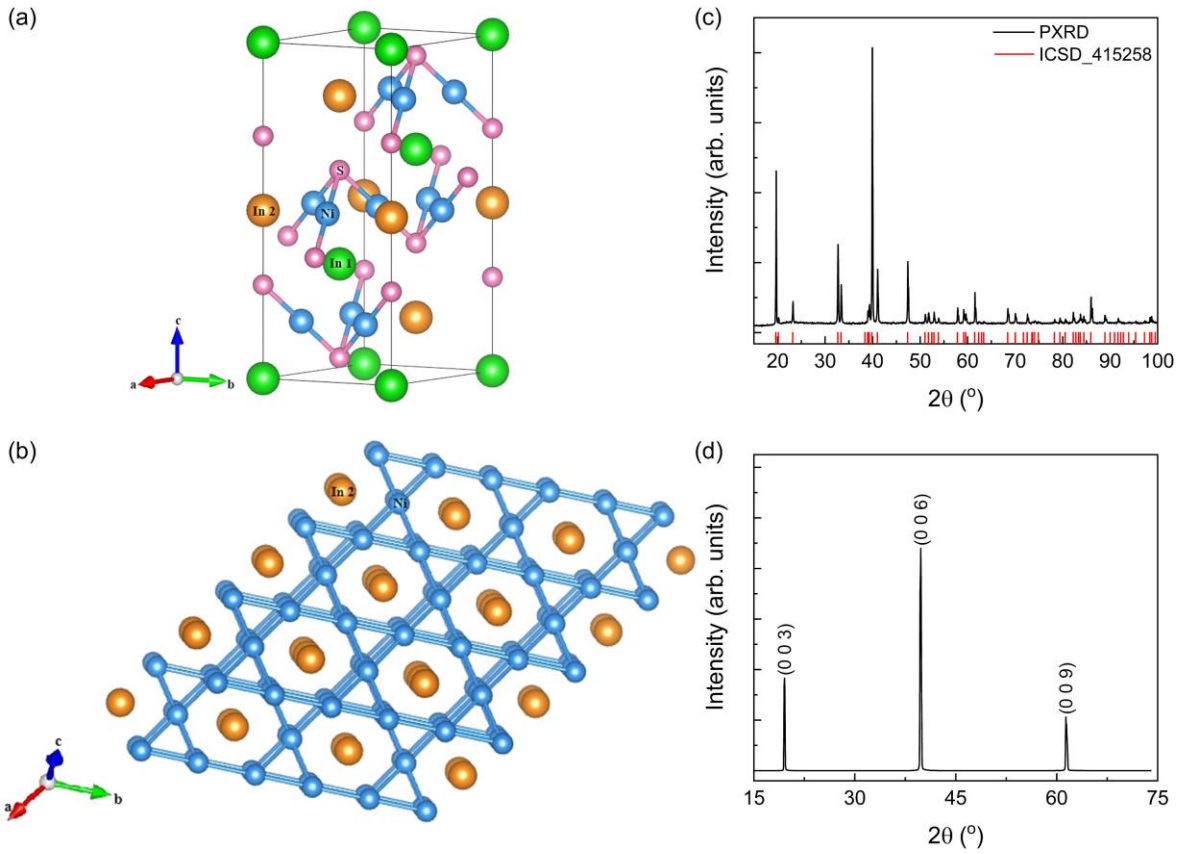

Figure 5.2: (a) Conventional unit cell of $Ni_3In_2S_2$. Green ball represents the In(1) atom siting at 3a (0, 0, 0); Orange ball represents the In(2) atom siting at 3b (0, 0, 0.5); Blue ball represents the Ni atom siting at 9d (0, 0.5, 0.5); and Pink ball represents the S atom siting at 6c (0, 0, 0.27883). (b) Kagomé lattice within Ni-In(2) layers. (c) Powder X-ray diffraction (PXRD) pattern of the ground single crystal $Ni_3In_2S_2$ (black line), and PXRD pattern generated by the previously reported data_ICSD_415258 as a comparison (red line) [124]. (d) Single-crystal X-ray diffraction pattern of $Ni_3In_2S_2$.

5.3.2 Heat Capacity

Figure 5.3a displays the temperature-dependent heat capacity c_p of $Ni_3In_2S_2$ under zero and 10 T applied magnetic fields. Both c_p curves show no signatures of any structural phase transition within the measured temperature range, and the distinction between the two curves is negligible. The inset plots c_p/T versus T^2 below 4 K under zero magnetic field, and the data are fitted with the equation $c_p/T = \gamma + \beta T^2$, where γ is the Sommerfeld coefficient connected to the electronic heat capacity, β is the coefficient of phonons associated to the lattice heat capacity, and T is the

temperature [125]. The fitting result indicates that γ has a value of 8.3 mJ mol^{-1} K^{-2}, and β has a value of 0.4 mJ mol^{-1} K^{-4}, suggesting the Debye temperature of $Ni_3In_2S_2$ is 324 K. Because per atom the Sommerfeld coefficient is 1.2 mJ mol^{-1} K^{-2} atom^{-1}, close to 1mJ mol^{-1} K^{-2} atom^{-1}, $Ni_3In_2S_2$ has a low density of states (DOS) at the Fermi level (E_F), showing the characteristic of a semimetal. This γ value also means no strong electron correlation effects in the $Ni_3In_2S_2$ system, consistent with the previous study [122].

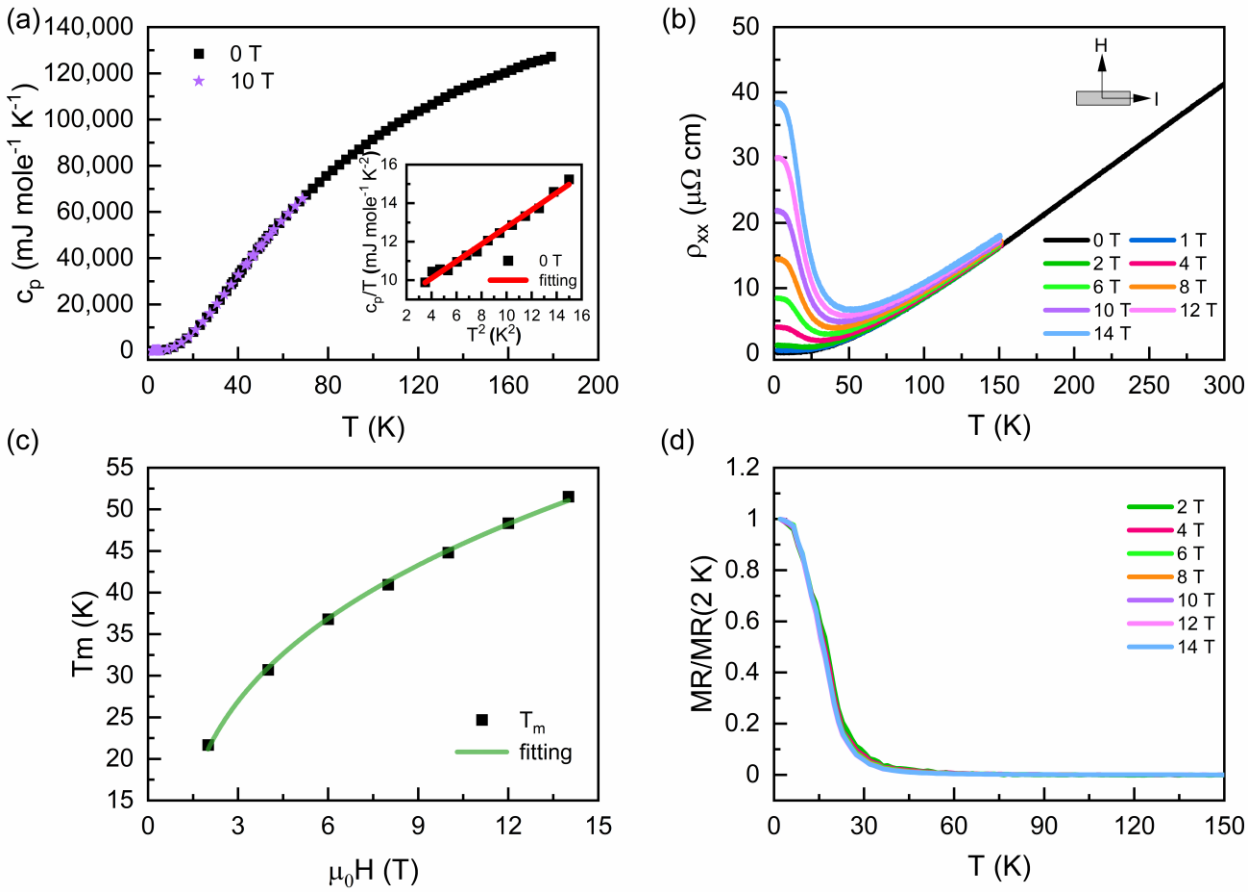

Figure 5.3: (a) Temperature-dependent heat capacity c_p of $Ni_3In_2S_2$ under zero and 10 T magnetic fields. The inset plots c_p/T versus T^2 below 4 K under zero field, and the data are fitted with the equation $c_p/T = \gamma + \beta T^2$. (b) Temperature-dependent longitudinal electrical resistivity ρ_{xx} under different magnetic fields. The magnetic field is parallel to the *c*-axis, and the current is in the *ab*-plane. (c) Minimum resistivity temperature T_m fitted by $T_m \propto (\mu_0 H - \mu_0 H_0)^{1/\nu}$. (d) Temperature-dependent normalized MR.

5.3.3 Magnetoresistance

Figure 5.3b plots the temperature-dependent longitudinal electrical resistivity ρ_{xx} of the single crystal $Ni_3In_2S_2$ under different magnetic fields, where the magnetic field is parallel to the *c*-axis, and the current is in the *ab*-plane. Without the externally applied magnetic field, ρ_{xx} decreases as the temperature drops, showing the metallic nature of $Ni_3In_2S_2$. The residual-resistivity ratio $RRR = \rho_{300\,K}/\rho_{2\,K} = 315$, indicates the high quality of the single crystal. ρ_{xx} exhibits a great dependence on the applied magnetic field in the low-temperature range, where the value of ρ_{xx} is significantly enhanced under the magnetic field. More interestingly, under the magnetic field greater than 2 T, ρ_{xx} shows an upturn at low temperatures and tends to saturate at still lower temperatures. The temperature corresponding to the minimum resistivity, T_m, increases as the magnetic field increases and can be well fitted by the relation $T_m \propto (\mu_0 H - \mu_0 H_0)^{1/\nu}$ [126] with ν = 2.95 and $\mu_0 H_0$ = 1.04 T, as shown in Figure 5.3c. This magnetic field-induced resistivity upturn behavior (also called the turn-on temperature behavior in some literature) has been reported in many other nonmagnetic semimetals. It can be ascribed to a number of different mechanisms and, usually, more than one mechanism is considered contributing simultaneously. For example, in semimetals WTe_2 [127], $HfTe_2$ [128], $PtSn_4$ [129], and $PdSn_4$ [34], this behavior is due to a high-quality sample of small residual resistivity, low charge carrier density, and high mobility, that follows the Kohler's rule in the applied magnetic field under different temperatures. In $NbSb_2$ [130], the external magnetic field breaks the time reversal invariance and modifies the Fermi surface related to the Dirac-like point. Combined with the high carrier mobility, the resistivity upturn at low temperatures is observed. The metal-insulator and reentrant insulator-metal transitions occurring due to the gap opening at the band-touching points in graphite also lead to this upturn behavior [131, 132], In LaBi [35], it can be explained by the electron-hole

compensation and the Kohler's rule. In orthorhombic phase of $MoTe_2$ [36], the upturn behavior originates from the combination of the mixed d - p orbital texture in the electron pocket and the electron-hole compensation. The temperature-dependent normalized MR, which is defined by $\mathrm{MR}(\mu_0 H, T) = (\rho_{xx}(\mu_0 H, T) - \rho_{xx}(0, T))/\rho_{xx}(0, T)$ under a fixed field, divided by the MR at 2 K under this field, i.e., $MR(\mu_0 H, T)/MR(\mu_0 H, 2\ \mathrm{K})$, is plotted in Figure 5.3d. In the case the external magnetic field induces a gap-opening at the band-touching point, the normalized MR curve displays a steeper slope under the higher field than under the lower field [36]. However, because the normalized MR curves under different magnetic fields collapse onto one curve, the metal-insulator transition is not the cause of the upturn behavior in $Ni_3In_2S_2$. Here, it is of significance to mention again that the heat capacity curve exhibits negligible discrepancies under zero and 10 T applied magnetic fields (as illustrated in Figure 5.3a) at temperatures below 70 K. This indicates that the external magnetic field has no bearing on DOS at the Fermi level (E_F), which further supports the conclusion that there is no metal-insulator transition occurring [36]. To delve deeper into the underlying factors behind this behavior, I now analyze the magnetoresistance and Hall resistivity at fixed temperatures.

The magnetic-field-dependent transverse MR at different temperatures is displayed in Figure 5.4a. Measurements were done with the applied magnetic field aligned along the *c*-axis and the current flowing within the *ab*-plane. At room temperature, the MR is very small. However, as the temperature decreases, a gradual increase in MR is observed until it becomes significantly enhanced below 50 K. As displayed in the inset, the MR at 14 T dramatically increases starting from 50 K, eventually reaching a giant value of 23 680% at 2 K. The Shubnikov–de Haas (SdH) oscillations are observed in the high field range at 2 K, exhibit diminished traceability at 4 K, and vanish entirely at higher temperatures. The oscillatory component in the resistivity at 2 K is

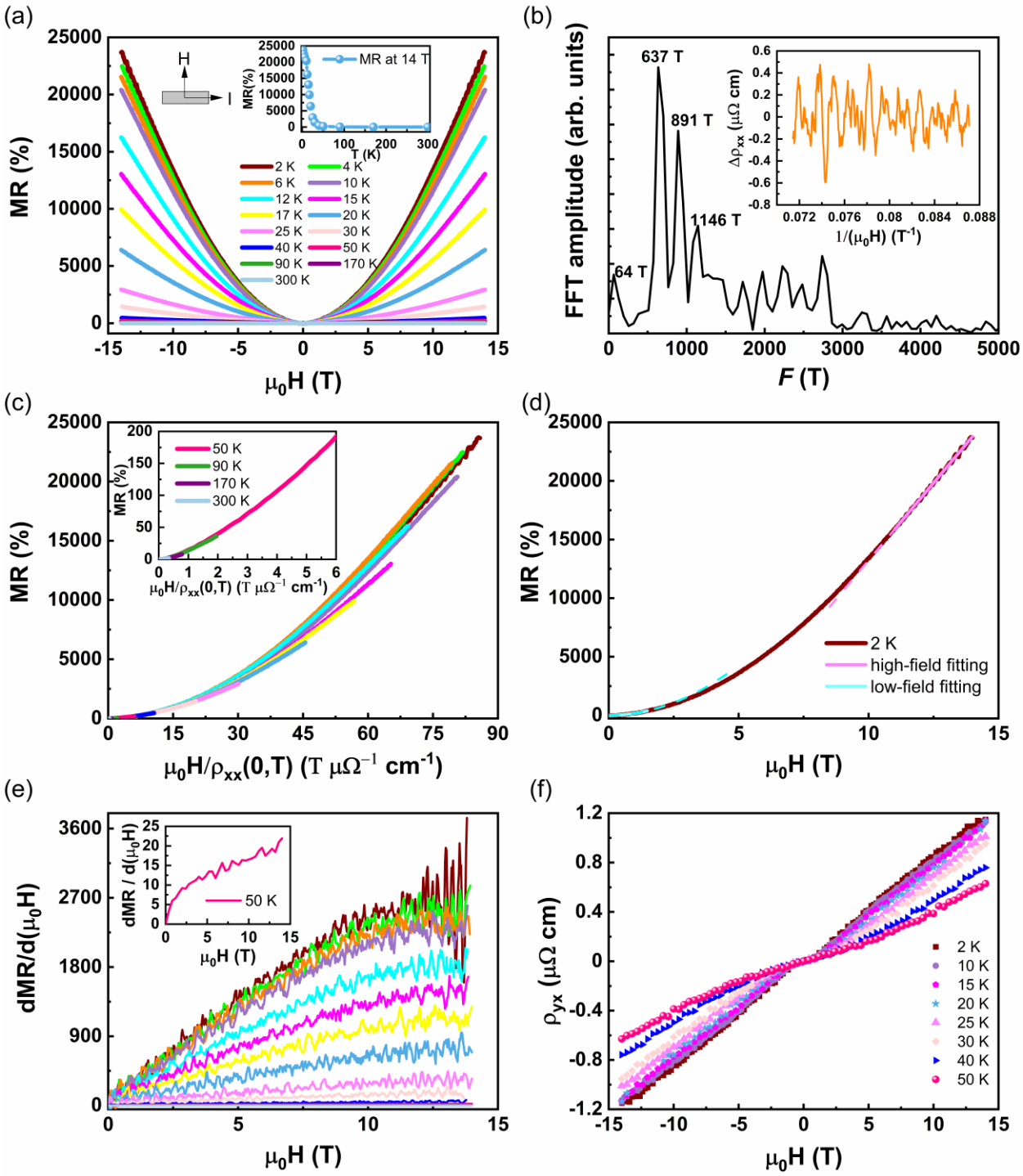

Figure 5.4: (a) Transverse MR at different temperatures. The magnetic field is along the *c*-axis and the current is in the *ab*-plane. The inset shows the MR under 14 T at different temperatures. (b) FFT spectrum of SdH oscillations. The inset plots the oscillatory component in resistivity. (c) Kohler plots. The inset enlarges the curves above 50 K. (d) Fitting of MR at 2 K. The dashed extension lines serve as a guidance for the eye. (e) First-order derivative of MR. The inset enlarges the curve at 50 K. (f) Hall resistivity ρ_{yx} at different temperatures.

acquired after subtracting the linear background from the resistivity data, and is plotted against $1/(\mu_0 H)$, as shown in the inset of Figure 5.4b. The corresponding fast Fourier transform (FFT) spectrum (Figure 5.4b) displays the oscillation frequencies of 64 T, 637 T, 891 T, and 1146 T.

The Kohler plots at different temperatures are depicted in Figure 5.4c. It is evident that the scaled MR curves do not fall onto a single curve, particularly at temperatures below 40 K and high fields. This signifies a violation of Kohler's rule, meaning that MR does not follow the same functional form of $\mu_0 H/\rho_{xx}(0,T)$ at different temperatures. The breakdown of the Kohler's rule indicates that the pattern of electron scattering varies as the temperature changes, which could be caused by variations in the mobility and/or the carrier concentration ratio of holes to electrons with temperature, and/or the effects of orbit quantization [33, 35]. Here, I can thus exclude the Kohler's rule as the origin of the resistivity upturn behavior.

It is worth pointing out that the MR curve exhibits different magnetic field dependence at a fixed temperature as the field changes. For instance, the MR curve at 2 K can be fitted by the second-order polynomial in the low-field range and the first-order polynomial in the high-field range separately, as shown in Figure 5.4d. In the field range from 0 to 1.5 T, the fitting result is $MR = 13.2\mu_0 H + 168.5(\mu_0 H)^2$. Although there is a trace of linear contribution, the quadratic term predominates in the MR. However, the MR curve deviates from this relation quickly as the magnetic field increases. In the field range of 11 T to 14 T, the MR curve is well fitted by the linear relation, showing a $\mu_0 H$ dependence. This field dependence change can be clearly seen in the first-order derivative of the MR data plotted in Figure 5.4e. At 2 K, the $dMR/d(\mu_0 H)$ curve displays a linear behavior under low fields, suggesting that MR is dominated by the quadratic dependence. As the magnetic field increases, the $dMR/d(\mu_0 H)$ curve starts to bend and eventually becomes flat, indicating a linear MR, when the SdH oscillations are ignored. This dependence change is

retained until the temperature rises to 50 K. Above 50 K, the $dMR/d(\mu_0 H)$ curve no longer tends to flatten under high fields (see the inset of Figure 5.4e).

Figure 5.4f shows the magnetic-field-dependent Hall resistivity ρ_{yx} at different temperatures. The magnetic field and the current directions are the same as when measuring the transverse MR. Below 50 K, the ρ_{yx} exhibits nonlinear behavior under low magnetic fields, which is the feature of compensated or nearly compensated semimetals, i.e., the contribution of both holes and electron to the transport properties is essential. The positive ρ_{yx} under the positive high fields suggests that holes make a greater contribution than electrons in my $Ni_3In_2S_2$ crystal [33]. In studying transport properties of semimetals, a classical two-band model is usually used to fit magnetic field-dependent ρ_{xx} and ρ_{yx} data simultaneously to get an insight into the density and mobility of holes and electrons [33, 34, 133-135]. I fitted ρ_{xx} and ρ_{yx} data to the two-band model in the low-magnetic field range from -1.2 T to 1.2 T (see Figure 5.5). The equations (3.1) and (3.2) were used for the two-band model fitting (see **section *3.1.1***). The fitting returned hole and electron carrier density n_h and n_e, and hole and electron mobility μ_h and μ_e are displayed in Figure 5.6a and b, respectively. At 2 K, $Ni_3In_2S_2$ has a hole carrier density of 1.5×10^{21} cm^{-3} and an electron carrier density of 1.3×10^{21} cm^{-3}, and high hole and electron mobilities are comparable at ~1.4×10^{4} cm^2 V^{-1} s^{-1}. Based on the hole carrier density, one can roughly estimate that the Fermi wave number $k_F = (3\pi^2 n_h)^{1/3}$ is 3.54×10^9 m^{-3}. This gives a quantum oscillation frequency of $F = \hbar {k_F}^2/2e = 4.1 \times 10^3$ T, which is consistent with the high oscillation frequency of the hole band deduced from dHvA results in **section *5.3.5*** (see Figure 5.12f). As temperature increases, both carrier density and mobility decrease. However, I want to point out the limitation of the two-band model in analyzing my $Ni_3In_2S_2$ crystal. For example, I extended the two-band model fitting result in Figure 5.5a to 14 T, as shown in Figure 5.6c and d. It is clear that the low-field fitting result

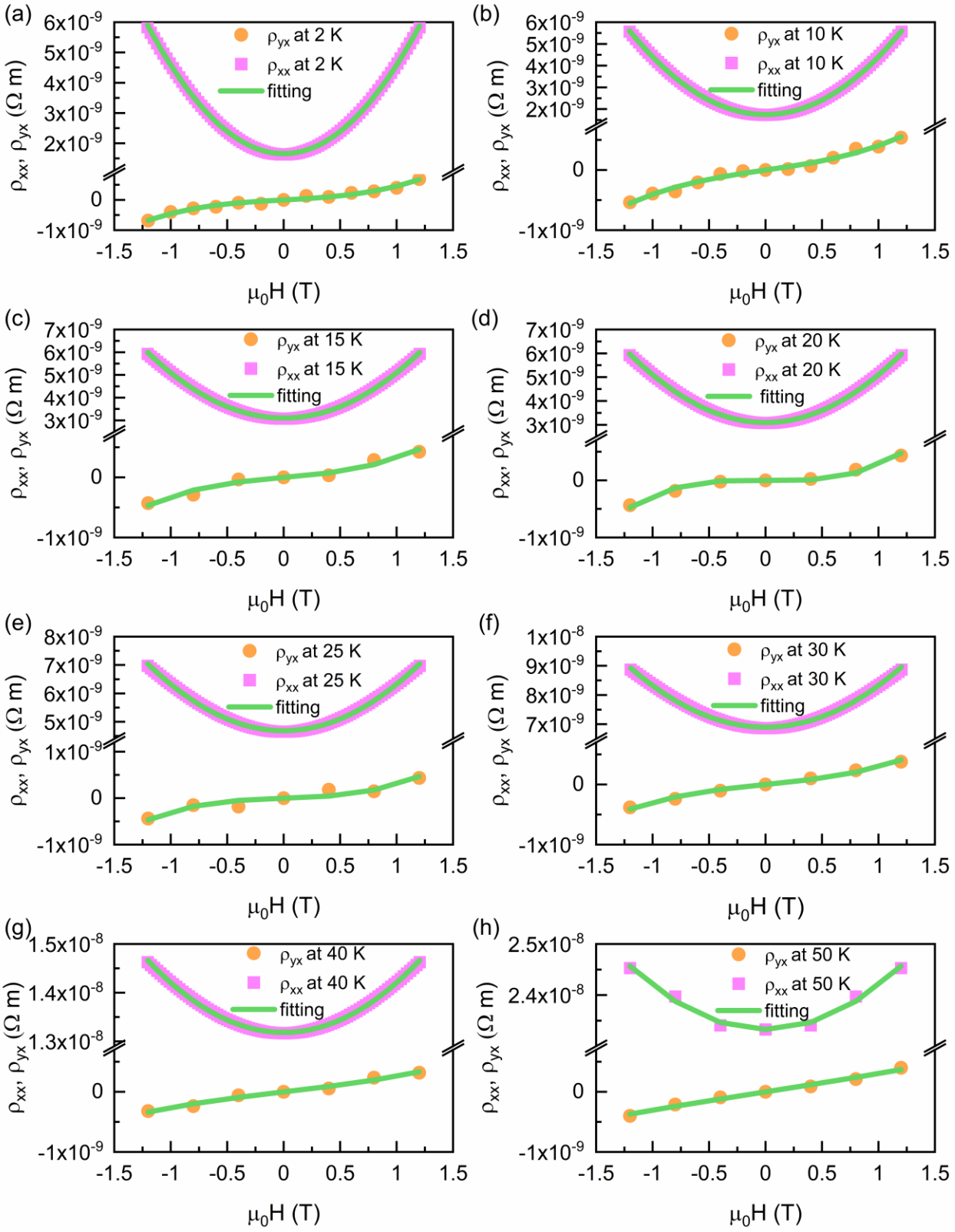

Figure 5.5: Two-band model fitting of magnetoresistivity ρ_{xx} and Hall resistivity ρ_{yx} at different temperatures in the magnetic field range from -1.2 T to 1.2 T. Solid dots are experimental data, and green lines represent fitting results.

deviates from the experimental data as the magnetic field increases. I also tried to fit 2 K ρ_{xx} and ρ_{yx} data to the two-band model in the magnetic field range from -14 T to 14 T. The best fitting result (see Figure 5.7), i.e., the Chi-square of fitting reaches minimum and the Chi-square tolerance value of 10^{-9} is reached, is still not satisfactory. The fact that the two-band model does not work well under higher magnetic fields implies that some other mechanisms, beyond the classical free-electron theory, also affect the MR of $Ni_3In_2S_2$, which will be discussed in the following section.

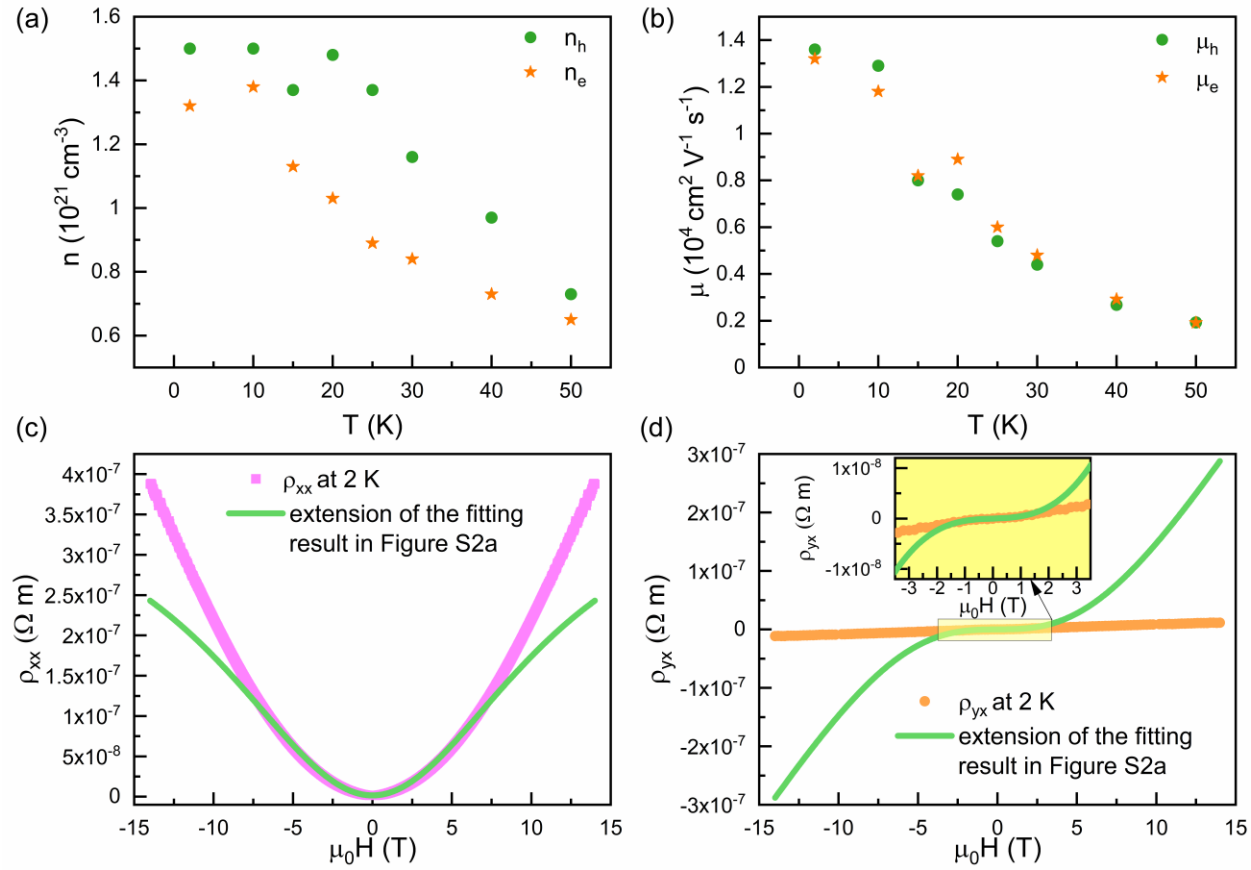

Figure 5.6: (a) Hole and electron carrier density n_h and n_e, and (b) hole and electron mobility μ_h and μ_e acquired from the two-band model fitting shown in Figure 5.5. (c) (d) Comparison between experimental data of ρ_{xx} and ρ_{yx} at 2 K and extension of the fitting result in Figure 5.5a to 14 T. The inset in (d) enlarges the curves under magnetic fields below 3.5 T.

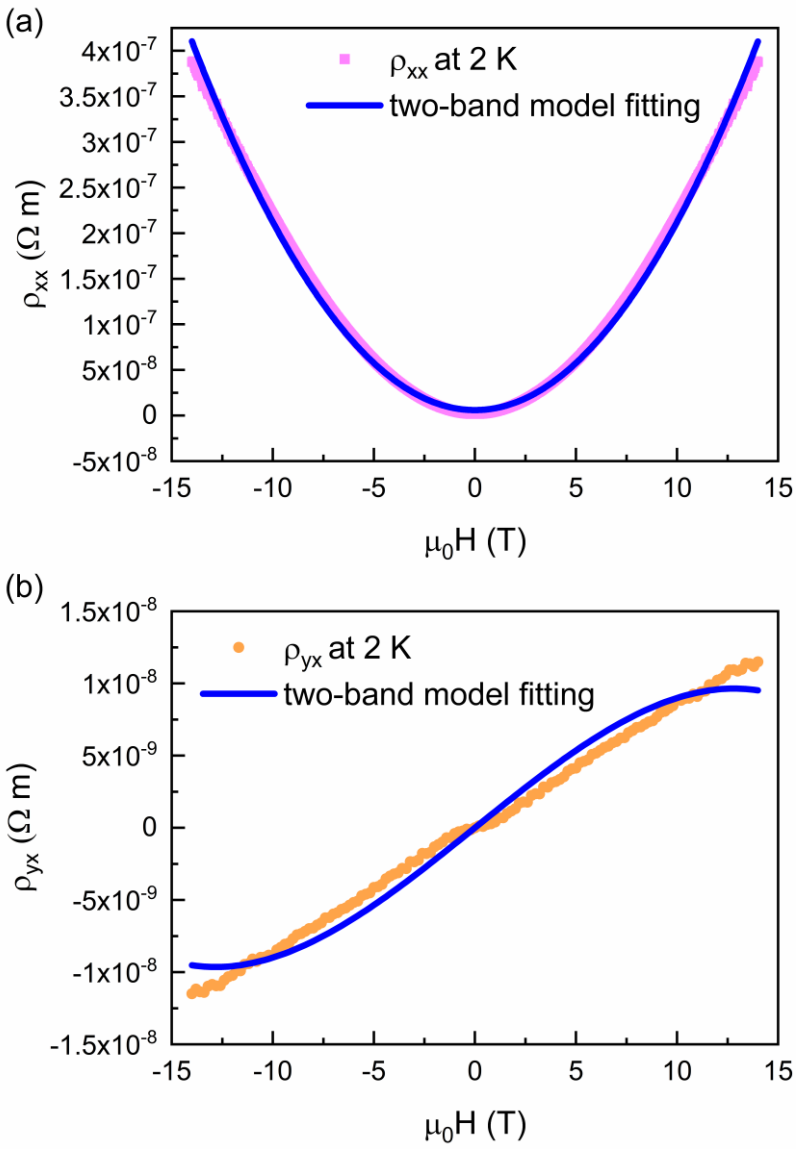

Figure 5.7: Two-band model fitting of (a) ρ_{xx} and (b) ρ_{yx} at 2 K in the magnetic field range from -14 T to 14 T. Solid dots are experimental data, and blue lines represent fitting results. The fitting suggests that hole carrier density n_h is 8.75×10^{20} cm^{-3}, electron carrier density n_e is 8.78×10^{20} cm^{-3}, hole mobility μ_h is 6879 cm^2 V^{-1} s^{-1}, and electron mobility μ_e is 4990 cm^2 V^{-1} s^{-1}. This fitting result is not satisfying. It deviates from the experimental data and does not capture the non-linear behavior of ρ_{yx} in the low-magnetic field range, an important feature of semimetal.

5.3.4 Density of states, Band structure, and Fermi Surface

Figure 5.8a shows the total density of states (DOS) of $Ni_3In_2S_2$ and element-specific partial DOS (PDOS) of Ni, In, and S atoms. The DOS near the Fermi level (E_F) is dominated by the PDOS

of Ni atoms, which is mainly contributed by the d-orbitals of Ni (see Figure 5.8b). The DOS at the E_F is 3.02 states eV^{-1} unit $cell^{-1}$, which gives the Sommerfeld coefficient of 7.1 mJ mol^{-1} K^{-2}, estimated by the formula $\gamma = \pi^2 k_B^2 n(E_F)/3$, where k_B is the Boltzmann constant, and $n(E_F)$ is the DOS at the E_F [125]. This value is close to that obtained from the fitting of the heat capacity data. Considering that the formula used here is derived from the free electron gas model, which certainly oversimplifies the situation of a real semimetal, one can say that the computation is well consistent with the experiments [100].

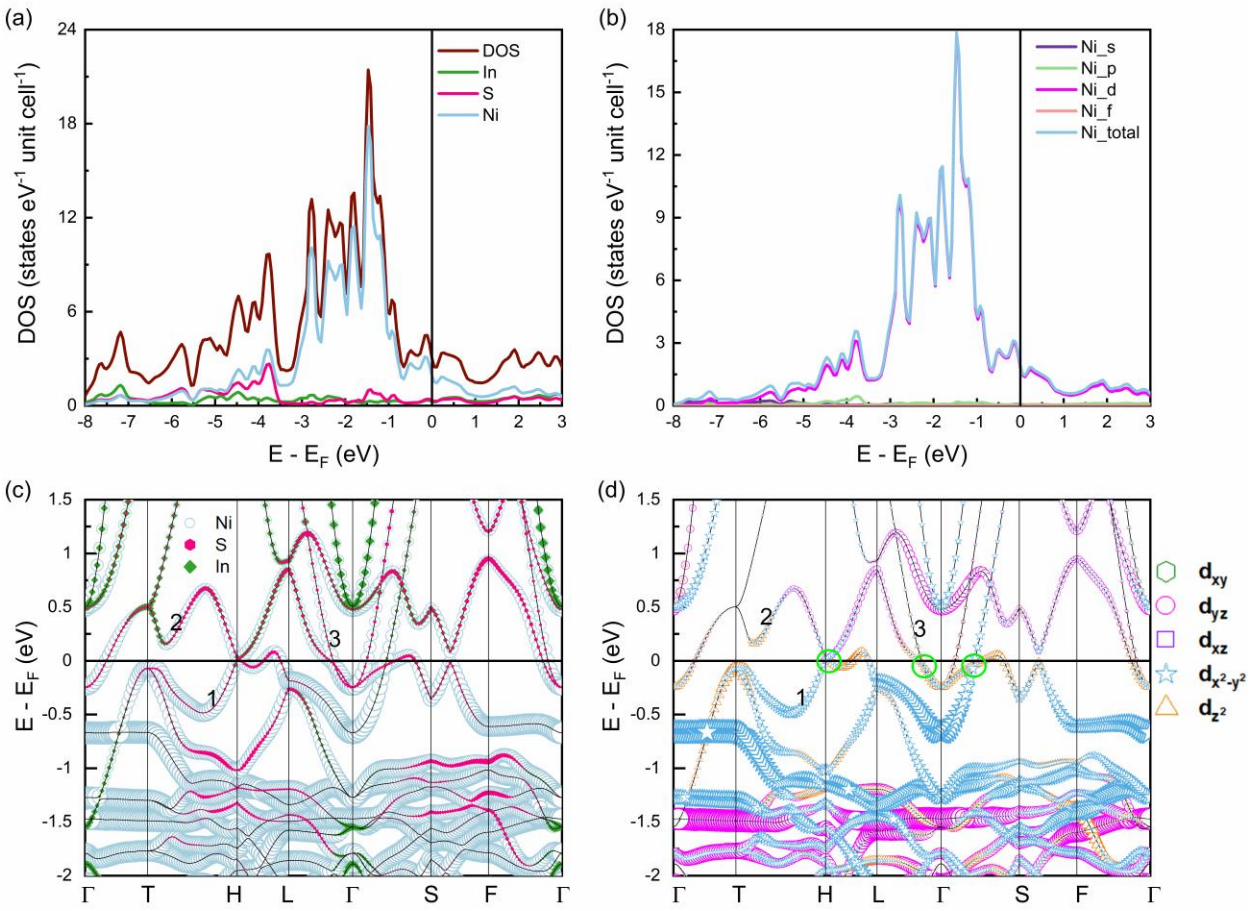

Figure 5.8: (a) DOS of $Ni_3In_2S_2$ and PDOS of Ni, In, and S atoms. (b) Orbital contributions to PDOS of Ni atoms. (c) Element resolved electronic band structure. (d) Orbital projected electronic band structure. The band crossings are marked by the green circles. The symbol size is proportional to DOS. The numbers 1,2 and 3 correspond to the bands 1, 2 and 3 on the Fermi Surface.

The band structure of $Ni_3In_2S_2$, marked with the contribution of each element to bands, is displayed in Figure 5.8c. Here, the same *k*-path as in the previous study is used, and similar results are obtained [122]. The bands near the E_F are dominated by Ni, as expected. The orbital projected band structure of $Ni_3In_2S_2$ in Figure 5.8d shows significant contributions of d_{yz}, $d_{x^2-y^2}$, and d_{z^2} orbitals to the bands near the E_F. These imply that Ni 3d orbitals dominate the transport properties of $Ni_3In_2S_2$. There are three bands crossing the Fermi level. Band 1 corresponds to the hole pockets near the H point (see Figure 5.9a and b), while bands 2 and 3 are related to the electron pockets at the Γ point (see Figure 5.9c, d, e, and f). The calculated volumes of the hole pockets in band 1 and the electron pockets in bands 2 and 3 are 0.1799 $Å^{-3}$, 0.1469 $Å^{-3}$, and 0.02787 $Å^{-3}$, respectively. The hole density of band 1 is 1.45×10^{21} cm^{-3}, and the electron density of band 2 and band 3 is 1.18×10^{21} cm^{-3} and 0.23×10^{21} cm^{-3} separately, which agrees with carrier density acquired from the two-band model fitting. The almost equal hole and electron density suggest that $Ni_3In_2S_2$ is a nearly compensated semimetal. The classical free-electron theory points out that the electron-hole compensation leads to an unsaturated quadratic MR [33] and is the origin of the extremely large MR as well as the magnetic induced-resistivity upturn behavior in some materials, as listed in **section *5.3.3***. However, the limitation of the two-band model fitting hints that the classical free-electron theory is not sufficient to explain the transport properties in $Ni_3In_2S_2$. Moreover, the MR curves exhibit a shift from the quadratic to the linear magnetic field dependence starting from a low magnetic field and the apparent violation of Kohler's rule under high magnetic fields, indicating that some other mechanisms contribute to the large MR instead of the electron-hole compensation.

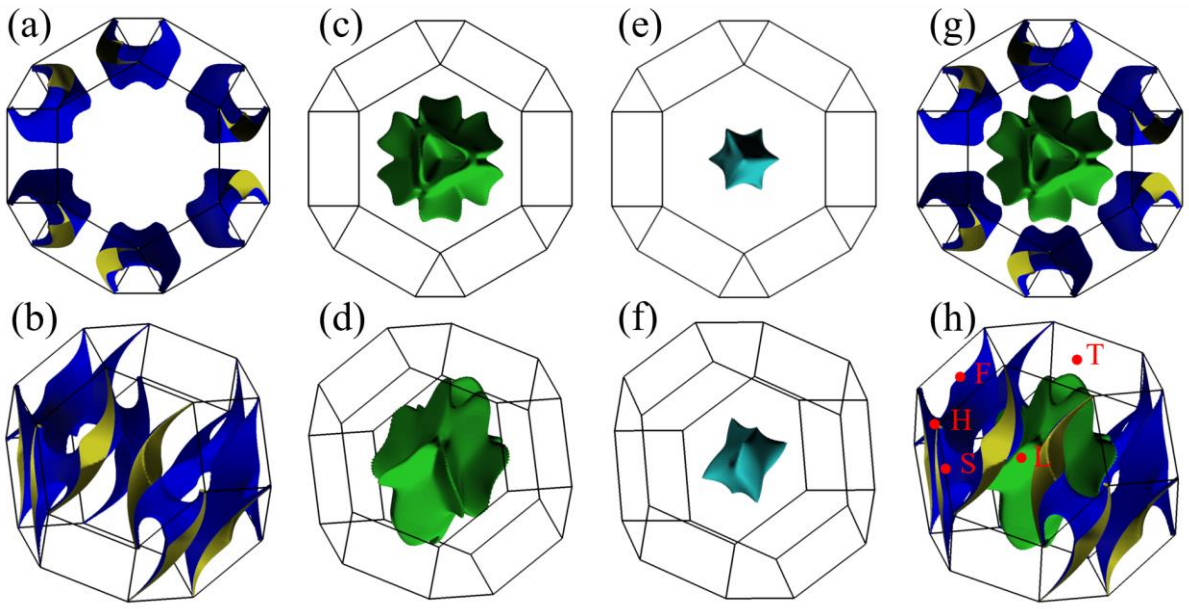

Figure 5.9: Top and side views of the calculated Fermi surface. (a)(b) Hole pockets associated to band 1. (c)(d) Electron pockets associated to band 2. (e)(f) Electron pockets associated to band 3. (g)(h) Merged graph. High symmetry points are labeled in (h). Γ point is the center of the Brillouin zone.

Marked by the green circles in Figure 5.8d, there are three band crossings within 0.04 eV from the E_F. Previous study has demonstrated that $Ni_3In_2S_2$ hosts six endless Dirac-nodal lines, and linear crossings near the E_F in the band structure were confirmed by ARPES measurements [122]. The linearly dispersive bands result in the small effective mass, which is verified by the following de Haas–van Alphen results, yielding high mobility. The high mobility is crucial to the large MR. Furthermore, the linear dispersion can also explain the linear MR observed under high magnetic fields. In Abrikosov's quantum linear MR theory, the linear MR can be caused by the interorbital transfer in the longitudinal direction in the quantum limit. This requires a linear magnetic field-dependent longitudinal transfer probability, which can be realized in materials with linear dispersion [37, 52, 53]. Although the inhomogeneous carrier density in disordered systems can also result in a linear MR, it requires that the change in magnetoresistivity ρ_{xx} is smaller than the Hall resistivity ρ_{yx} [37, 39]. Clearly, this is not the case for my $Ni_3In_2S_2$ sample. As presented

in the following section, the lowest dHvA oscillation frequency is 11 T, which is associated with band 1. The linear MR manifests evidently under a magnetic field starting right from 11 T (see Figure 5.4d). This suggests that under fields larger than 11 T, band 1 is driven to the quantum limit and, thus, leads to the large linear MR, according to Abrikosov's quantum linear MR theory.

5.3.5 de Haas–van Alphen Quantum Oscillations

As shown in Figure 5.10a, the magnetic torque $\tau = VM \times \mu_0 H$, where V is the volume, M is the magnetization, and $\mu_0 H$ is the external applied magnetic field, is measured at different temperatures at $\theta = 2^{\circ}$, where $\theta = 0^{\circ}$ and 90° correspond to the applied magnetic field oriented along the c-axis and along the a-axis, respectively. Strong de Haas–van Alphen (dHvA) quantum oscillations are observed in my $Ni_3In_2S_2$ sample. In contrast to SdH oscillations in MR, which are only observable under high magnetic fields at 2 K, dHvA oscillations start under a much lower magnetic field and are evident even at higher temperatures. This behavior is usually seen in layered materials. The dHvA oscillations are directly linked to the Landau level energy spectrum, while the SdH effect is associated with the scattering rate of charge carriers [28]. Figure 5.10b plots the oscillatory components against $1/(\mu_0 H)$, which are acquired after subtracting the background from the magnetic torque data. The corresponding FFT spectra are displayed in Figure 5.10c. At 2 K, there are several strong main peaks with many weak peaks in the FFT spectrum. The dHvA frequency F is associated with the extremal Fermi surface cross-sectional area A perpendicular to the magnetic field through the Onsager relationship: $F = (\hbar/2\pi e)A$, where $\hbar$ is the reduced Planck constant and e is the elementary charge. The large number of peaks shows the complexity of the Fermi surface, as seen in Figure 5.9. Many peaks damp out quickly as the temperature increases. For those frequencies with peaks still visible at 6 K, I plot the amplitude of each

frequency as a function of temperature in Figure 5.10d. The effective mass for each frequency band can be obtained by fitting the amplitude by the thermal damping factor in the Lifshitz-Kosevich (LK) formula, i.e., $R_T = (aT\mu/(\mu_0 H))/\sinh(aT\mu/(\mu_0 H))$, where $a = 14.69$ T/K, T is the temperature, μ is the ratio of effective cyclotron mass m^* to the free electron mass m_e, and $\mu_0 H$ is the applied magnetic field [28]. The obtained effective mass ratio μ and the corresponding frequency F are summarized in Table 5.1. Because the lowest oscillation frequency, 11 T, is far from other frequencies, and its signal is strong under low fields with no influences of other frequencies at 2 K, as shown in Figure 5.10e, it is possible to deduce the corresponding Dingle temperature. The Dingle plot (Figure 5.10f) plots $\mathrm{In}\left(\Delta\tau/\left((\mu_0 H)^{3/2} R_T\right)\right)$ as a function of $1/(\mu_0 H)$, where $\Delta\tau$ is the oscillation amplitude of frequency of 11 T at 2 K read from Figure 5.10e and R_T is the thermal damping factor at 2 K. The Dingle plot can be linearly fitted with a slope of -2.77, indicating that the Dingle temperature T_D is 0.75 K, as the slope is equal to $-aT_D\mu$, according to the field-damping factor in the LK formula [28]. Therefore, the corresponding quantum relaxation time $\tau_q = \hbar/2\pi k_B T_D$ is 1.6 ps, and the quantum mobility $\mu_q = e\tau_q/m^*$ is 1.1×10^4 cm^2 V^{-1} s^{-1}. The quantum mobility μ_q is less than the mobility acquired from the two-band model fitting. This is expected since μ_q is affected by scatterings in all directions, while the mobility introduced in the free-electron model is not influenced by small-angle scatterings [28]. The small effective mass and high quantum mobility of $Ni_3In_2S_2$ deduced from dHvA oscillations are comparable to those of semimetals with large MR [28]. I have also done the same measurement for $\theta = 85^\circ$, as shown in Figure 5.11.

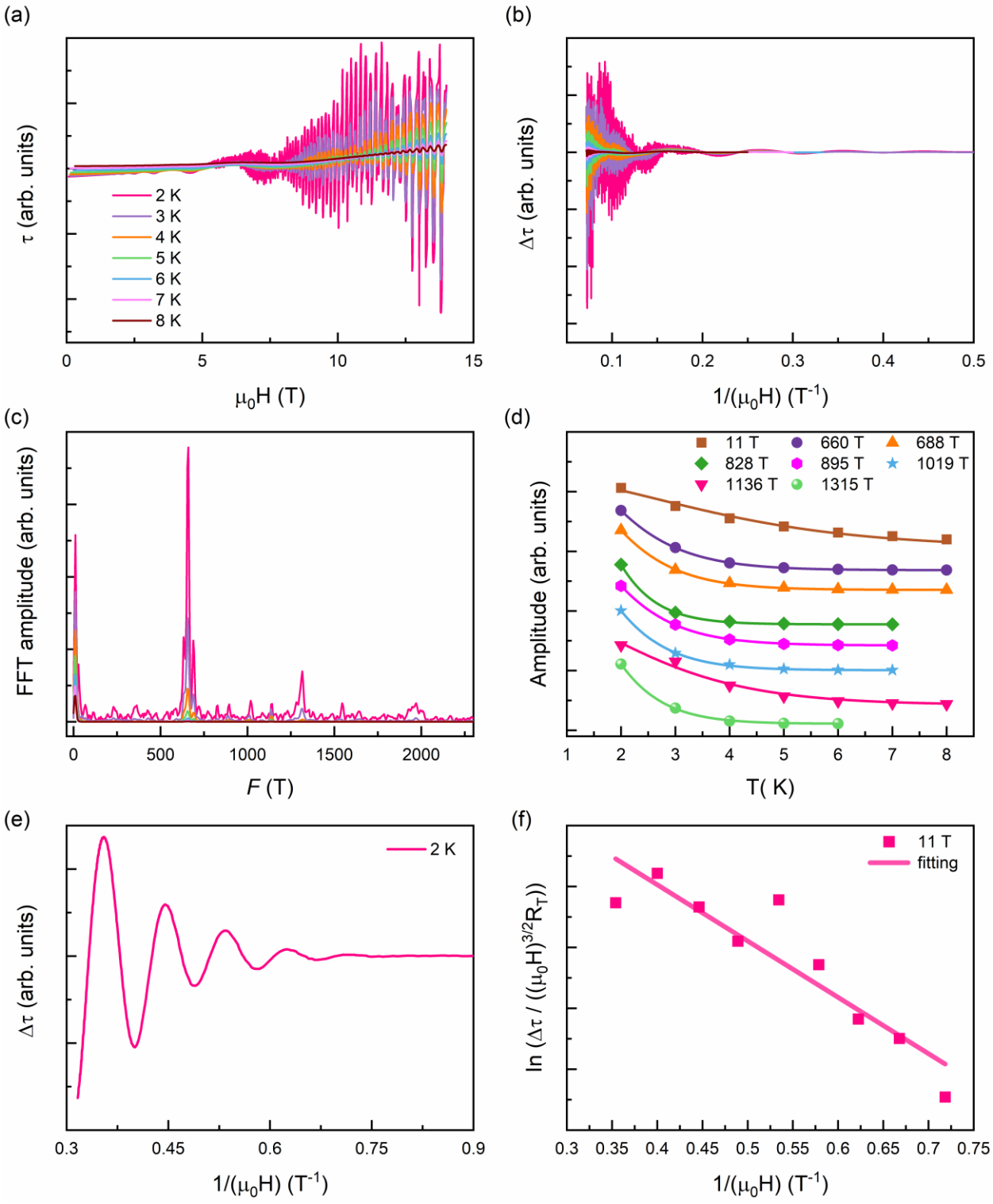

Figure 5.10: (a) Magnetic torque at $\theta = 2^{\circ}$. (b) Oscillatory components in torque signals. (c) Corresponding FFT spectra. (d) Amplitude of peaks in FFT spectra as a function of temperature. Solid lines represent fits to R_T in the LK formula. For the sake of clarity, these data points are rescaled and offset. (e) The oscillatory component in the torque signal at 2 K under low magnetic fields. (f) Dingle plot of frequency of 11 T. The solid line represents the linear fitting of the data points.

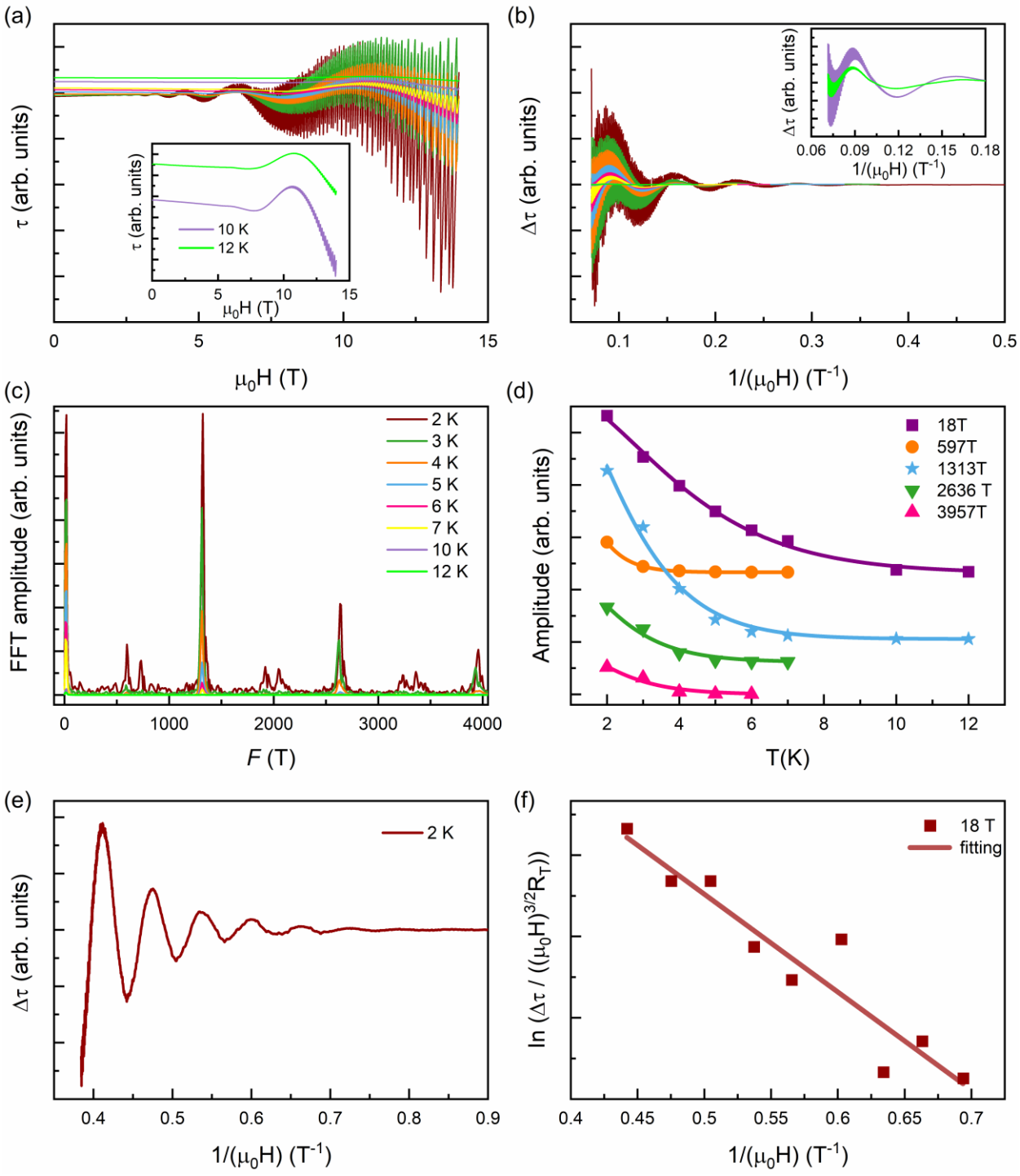

Figure 5.11: (a) Magnetic torque at $\theta = 85^{\circ}$. (b) Oscillatory component in torque. (c) Corresponding FFT spectra. (d) Amplitude of peaks in FFT spectra as a function of temperature. Solid lines represent fits to R_T in the LK formula. For the sake of clarity, these data points are rescaled and offset. (e) The oscillatory component in the torque signal at 2 K under low magnetic fields. (f) Dingle plot of frequency of 18 T. The solid line represents the linear fitting of the data points. The slope of the solid line is -3.61. Thus, the Dingle temperature T_D is 0.85 K. The corresponding quantum relaxation τ_q is 1.4 ps, and the quantum mobility μ_q is 8.7×10^3 cm^2 V^{-1} s^{-1}.

To further study the fermiology of $Ni_3In_2S_2$, I measured the angle-dependent magnetic torque from $\theta = 2^{\circ}$ to 85° at 2 K. The dHvA oscillations are observed in the entire angular range, and the corresponding FFT spectra are plotted in Figure 5.12a-e. The comparison between the calculated and experimental dHvA frequencies is presented in Figure 5.12f. Good agreements are seen between calculations and experiments for the frequency of about 1200 T (blue stars in Figure 5.12f), which is assigned to the smaller electron pockets at the Γ point linked to band 3, and for the frequency of about 10 T (green squares), which is assigned to the hole pockets associated with band 1. However, disagreements between calculations and experiments for high frequencies resulting from band 1 and band 2 are obvious. In addition, there are certain frequencies obtained from experiments (represented by pink crosses) that cannot be linked to any calculated frequencies, so that it is not possible to determine from which band they originate. The Fermi surface calculations are sensitive to the chemical potential and lattice parameters, and the complexity of the Fermi surface further complicates the analysis. For example, missing extremal cross-sectional areas and magnetic breakdown phenomena can cause significant differences between the computed and experimental results [28]. Thus, it is not surprising to see such a mismatch. The effective mass calculation draws upon the energy slope at the Fermi surface, given by $m^* = \frac{\hbar^2}{2\pi m_e}(\frac{dA}{dE})$. Frequencies with values around 1.1 kT originating from band 3 have the effective mass ranging from 0.4 m_e to 0.6 m_e. Frequencies between 2 kT and 4 kT resulting from band 2 have a much heavier effective mass ranging from 1.1 m_e to 2.8 m_e. The hole pockets linked to band 1 have complicated shapes and, thus, result in a wide distribution of frequencies from 10 T to 4.5 kT with effective mass ranging from 0.13 m_e to 5.2 m_e. I compare the calculated effective mass to that extracted from the fitting of experimental data in Table 5.1. Except for the experimental

effective mass corresponding to frequencies of 2636 T and 3957 T acquired at $\theta = 85^{\circ}$, much smaller than the calculated values, experiments and calculations show good consistency.

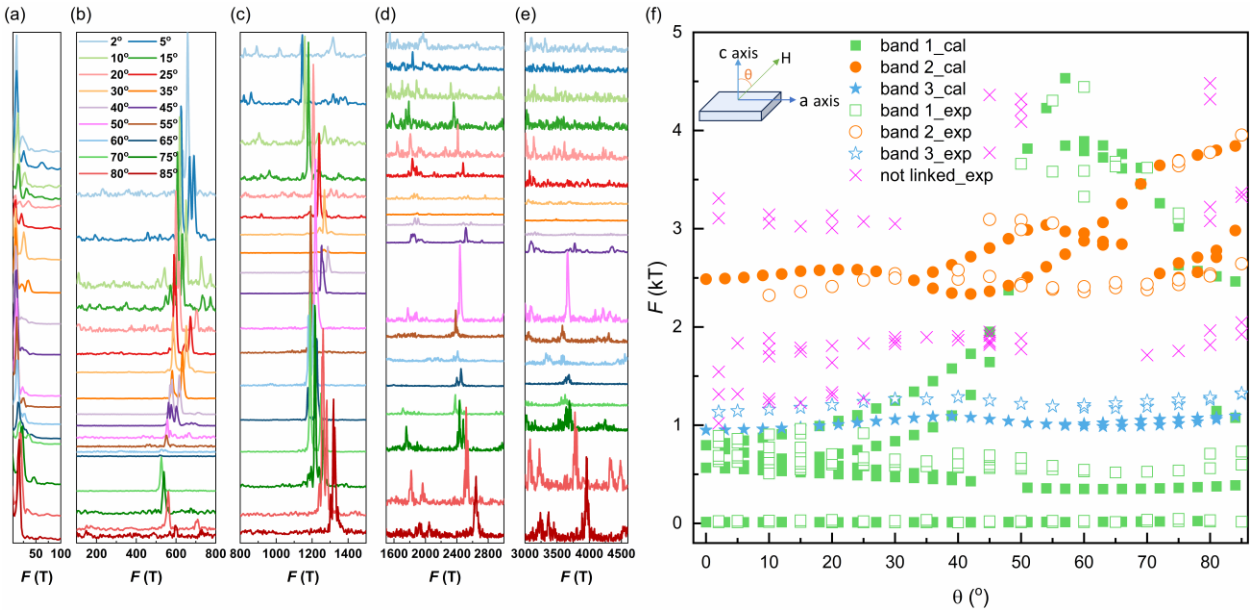

Figure 5.12: (a-e) FFT spectra of oscillatory components in torque measured at different angles θ. The definition of θ is shown in the inset of (f). For the sake of clarity, spectra are rescaled and offset. (f) The comparison between the calculated and experimental dHvA frequencies. Solid symbols represent the calculated frequencies. Open symbols represent experimental frequencies. Pink crosses represent frequencies obtained from experiments that cannot be linked to any calculated frequencies. The unit of F is in 10^3T, i.e., kT.

Table 5.1: Effective mass ratio of $Ni_3In_2S_2$ and the corresponding frequency and band. μ_{exp} is obtained from dHvA experimental results, and μ_{cal} is the calculated effective mass. The experiments-obtained frequencies, 1019 T and 1315 T, cannot be linked to any calculated frequencies, so μ_{cal} and corresponding bands are missing.

$\theta = 2^{\circ}$				$\theta = 85^{\circ}$			
F [T]	μ_{exp}	μ_{cal}	band	F [T]	μ_{exp}	μ_{cal}	band
11	0.25	0.15	1	18	0.29	0.24	1
660	0.58	0.64	1	597	1.01	0.83	1
688	0.62	0.66	1	1313	0.47	0.52	3
828	0.85	1.06	1	2636	0.56	2.13	2
895	0.62	1.10	1	3957	0.59	2.53	2
1019	0.69						
1136	0.37	0.41	3				
1315	0.75						

5.4 Conclusion

In this work, I have presented transport properties and quantum oscillations of single-crystalline semimetal $Ni_3In_2S_2$. The crystal exhibits extremely large transverse MR and magnetic field-induced resistivity upturn behavior at low temperatures. Below 50 K, the MR curves show a shift from the quadratic to the linear magnetic field dependence as the field increases. The computation results suggest that $Ni_3In_2S_2$ is a semimetal with three linear crossings near the Fermi level in the electronic band structure. The linearly dispersive bands result in small effective mass and, thus, high quantum mobility, which is affirmed by dHvA results. Moreover, the linear MR under high magnetic fields can also be explained by the linear dispersions. The high mobility and quantum linear MR resulting from the linearly dispersive bands lead to the exceptionally large transverse MR in my $Ni_3In_2S_2$ sample. Due to the very small resistivity and extremely large MR at low temperatures, an upturn behavior is observed. It is hoped that these findings can be a reference and inspiration for future research on semimetals with large MR. This work was published in reference [136].

Chapter 6 Low-Temperature Electrical and Thermal Transport in Type-II Dirac Semimetal $NiTe_2$

6.1 Motivation

Recently, several transition metal tellurides, such as $CoTe_2$ [137], $ZrTe_2$ [138], and $PdTe_2$ [139], have been identified as type-II Dirac semimetals, where the Lorentz invariance is violated and the Dirac cone is tilted. In these systems, however, the Dirac point is several hundred meV away from the Fermi level (E_F). Thus, the transport properties are dominated by those topologically trivial bands near E_F rather than the Dirac fermions.

$NiTe_2$, which shares the same crystal structure as the above mentioned tellurides, hosts a type-II Dirac point only about 80 meV above the E_F [140]. The Dirac point is located along the high-symmetry direction Γ-A (see Figure 6.6b), which is the invariant subspace of the three-fold rotation (C_3) symmetry. The symmetry analysis points out that the crossing bands have opposite rotation characters. As a result, the Dirac point is protected from perturbations respecting the C_3 symmetry [141]. The tilted type-II Dirac cone has been confirmed by ARPES experimentally [141].

Since the Dirac point of $NiTe_2$ is in the vicinity of the E_F, the corresponding Dirac fermions' contributions may very likely manifest in the transport properties. In this work, I study the electrical and thermal transport properties of $NiTe_2$ single crystal. The crystal displays a large and anisotropic magnetoresistance at low temperatures. The dHvA quantum oscillation results demonstrate its small effective mass and nontrivial Berry phase resulting from the Dirac point. The thermal conductivity of the $NiTe_2$ crystal is significantly suppressed by the applied magnetic field.

Additionally, the Lorenz number deduced from the thermal conductivity strongly deviates from the Sommerfeld value, indicating the breakdown of the Wiedemann-Franz law in $NiTe_2$.

6.2 Methods

Single crystal $NiTe_2$ was synthesized by the self-flux method. The raw materials with a molar ratio of Ni:Te = 1:11.5 were loaded into a quartz tube and sealed under vacuum. The tube was heated to 1100 ℃ and held for 24 hours before being quickly cooled to 700 ℃ and held for 2 hours. The tube was then cooled to 465 ℃ at a rate of 1 ℃/h. After that, the single crystal and excess liquid Te were separated at 465 ℃. (*This sample was provided by Dr. Genda Gu and Prof. Qiang Li at the Brookhaven National Lab.*)

The acquired crystal could be easily cleaved into smaller and thinner pieces mechanically, and the cleavage planes exhibited a shining and silver appearance. The orientation of the cleavage plane was determined via single-crystal X-ray diffraction measurement using a Rigaku Ultima IV X-ray diffractometer (Cu Kα). The chemical compositions of the crystal were confirmed by energy-dispersive X-ray spectrometry (EDS).

Electrical and thermal transport properties, heat capacity, and magnetic torque were measured in a Physical Property Measurement System (PPMS Dynacool, Quantum Design) under magnetic fields up to 14 T and temperatures down to 2 K. The torque measurements were carried out on a piezoresistive cantilever mounted on the PPMS rotator sample puck. The sample was affixed to the cantilever using vacuum grease. The thermal conductivity and Seebeck coefficient were measured using the Thermal Transport Option (TTO) of the PPMS. To correct for magnetic field-induced temperature errors resulting from the magnetoresistance (MR), the resistive thermometers were calibrated using the PPMS MR calibration wizard before the transport measurement.

6.3 Results and Discussion

6.3.1 Crystal Structure

$NiTe_2$ crystallizes in a trigonal lattice structure with the space group No.164 ($P\bar{3}m1$). Figure 6.1a and b illustrate different perspectives of its unit cell, which are drawn using the VESTA software [54]. Figure 6.1c presents the single-crystal X-ray diffraction patterns of the $NiTe_2$ crystal, which indicates that the cleavage plane is perpendicular to the c-axis of the unit cell. The sample exhibits almost precise stoichiometry, as evidenced by its chemical compositions of $NiTe_{1.95}$ determined via EDS.

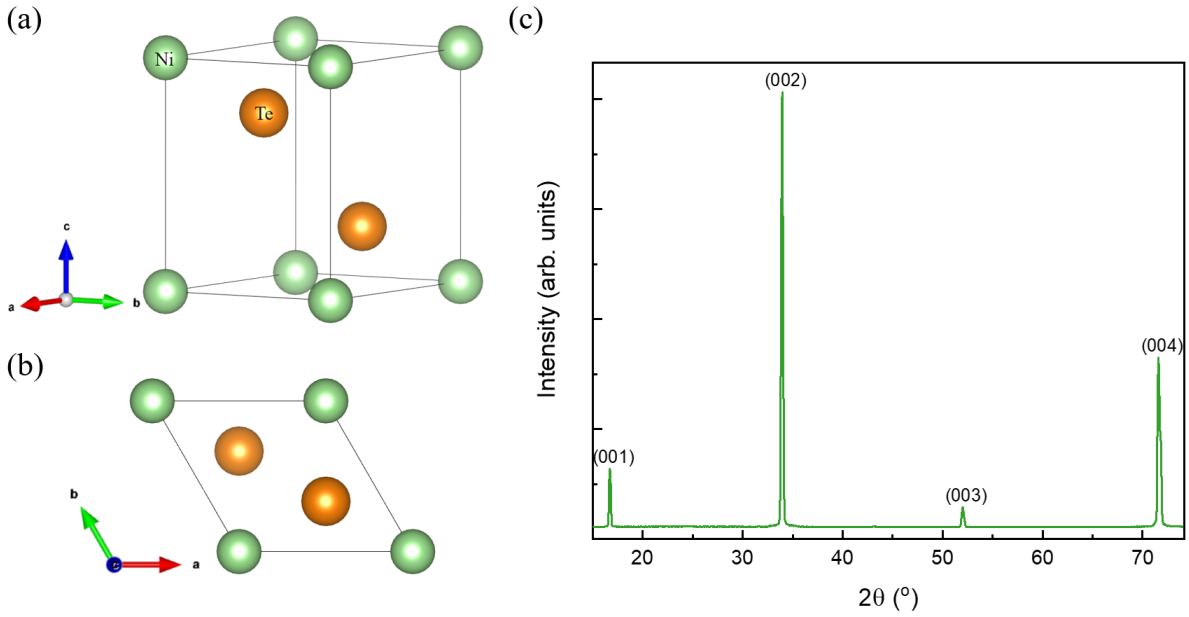

Figure 6.1: (a)(b) Different perspectives of the unit cell of $NiTe_2$. (c) Single-crystal X-ray diffraction patterns of the acquired $NiTe_2$ crystal.

6.3.2 Electrical Transport Properties

Figure 6.2a plots the temperature-dependent longitudinal electrical resistivity ρ_{xx} of the single crystal $NiTe_2$, which decreases as the temperature drops, indicating its metallic nature. The residual resistivity is 0.11 μΩ cm, and the residual-resistivity ratio RRR, defined as $\rho_{300\,K}/\rho_{2\,K}$, is 260, showing the high quality of the single crystal.

As shown in Figure 6.2b and c, $NiTe_2$ displays large transverse MR at low temperatures, which reaches about 700% at 2 K and 14 T. The transverse MR was measured with the applied magnetic field aligned along the *c*-axis and the current flowing within the *ab*-plane of the crystal. The transverse MR shows different magnetic field dependence at different temperatures. In the temperature range from 2 K to 25 K, the MR curve exhibits a cusp under low fields. As the temperature increases, this cusp is gradually wiped out and disappears at 30 K. In the temperature range from 30 K to 50 K, the MR curve shows an entirely different magnetic field dependence compared to that below 25 K. In this temperature range, the MR curve can be fitted by the second-order polynomial under fields from 0 to 4 T and the first-order polynomial under fields from 4 to 14 T separately (see the black and red lines in Figure 6.2c). These phenomena suggest that the scattering mechanisms dominating the transport change as the temperature and the applied magnetic field vary.

Figure 6.2d shows the magnetic field-dependent ρ_{xx} at 2 K with several tilt angles θ, where θ is the angle between the c-axis and the applied magnetic field (see the inset). At a fixed field weaker than 4.5 T, the ρ_{xx} decreases as θ increases. This can be clearly seen in the polar plot of the angular variation of ρ_{xx} under a field of 2 T in Figure 6.2f. The ρ_{xx} reaches its maximum when the field is perpendicular to the current ($\theta = 0^{\circ}$), while it reaches its minimum when the field is parallel to the current ($\theta = 90^{\circ}$). This is not surprising because the Lorentz force contribution to the MR becomes smaller as θ increases. However, under fields stronger than 4.5 T, albeit ρ_{xx} at

$\theta = 0^{\circ}$ is still greater than that at $\theta = 90^{\circ}$, the greatest ρ_{xx} occurs at θ of 30° or 40° depending on the field. The polar plot in Figure 6.2f exhibits a butterfly shape at 10 T with four maxima occurring when the field is along the direction in the middle between the c-axis and the current direction. Moreover, I fitted the magnetic field-dependent ρ_{xx} curves (except the one at $\theta = 90^{\circ}$) above 2 T to the equation $\rho_{xx}(B) = a + bB^{m}$, where $B = \mu_0 H$ is the applied magnetic field, and a, b, and m are fitting parameters. The curve representing the longitudinal magnetoresistivity, i.e., the curve at $\theta = 90^{\circ}$, displays a positive MR in the measured field range and does not show any signatures of the chiral anomaly-induced negative longitudinal magnetoresistance. This curve cannot be fitted by the power law; instead, it is fitted by a logarithm relation. As plotted in Figure 6.2e, the fitted index m firstly increases as θ increases, reaches the maximum at 40°, and then decreases as θ increases. The varying value of m and shape change of the polar plot indicate that the Fermi surface or the scattering patterns contributing to the transport are highly anisotropic at 2 K and are also sensitive to the strength of the applied magnetic field.

As displayed in Figure 6.3a, the Hall resistivity ρ_{yx} curves below 50 K exhibit nonlinear behaviors, which indicates the co-existence of both hole- and electron-type carriers. The positive ρ_{yx} under the positive fields suggests that hole-type carriers make a greater contribution than electron-type carriers in the $NiTe_2$ crystal. Generally, the carrier density and mobility can be obtained by fitting the magnetic field-dependent ρ_{xx} and ρ_{yx} simultaneously to the classical two-band model. However, the complex transverse MR behaviors cause the fitting of the ρ_{xx} to the two-band model (equation (3.1) in **section *3.1.1***) to fail. Instead, here I provide the Hall carrier density n at 14 T, which is calculated through the equation $n = B/(e\rho_{yx,14\,\mathrm{T}})$, where $B = \mu_0 H$ is the applied magnetic field, and $\rho_{yx,14\,\mathrm{T}}$ is the value of ρ_{yx} at 14 T. As shown in Figure 6.3b, the

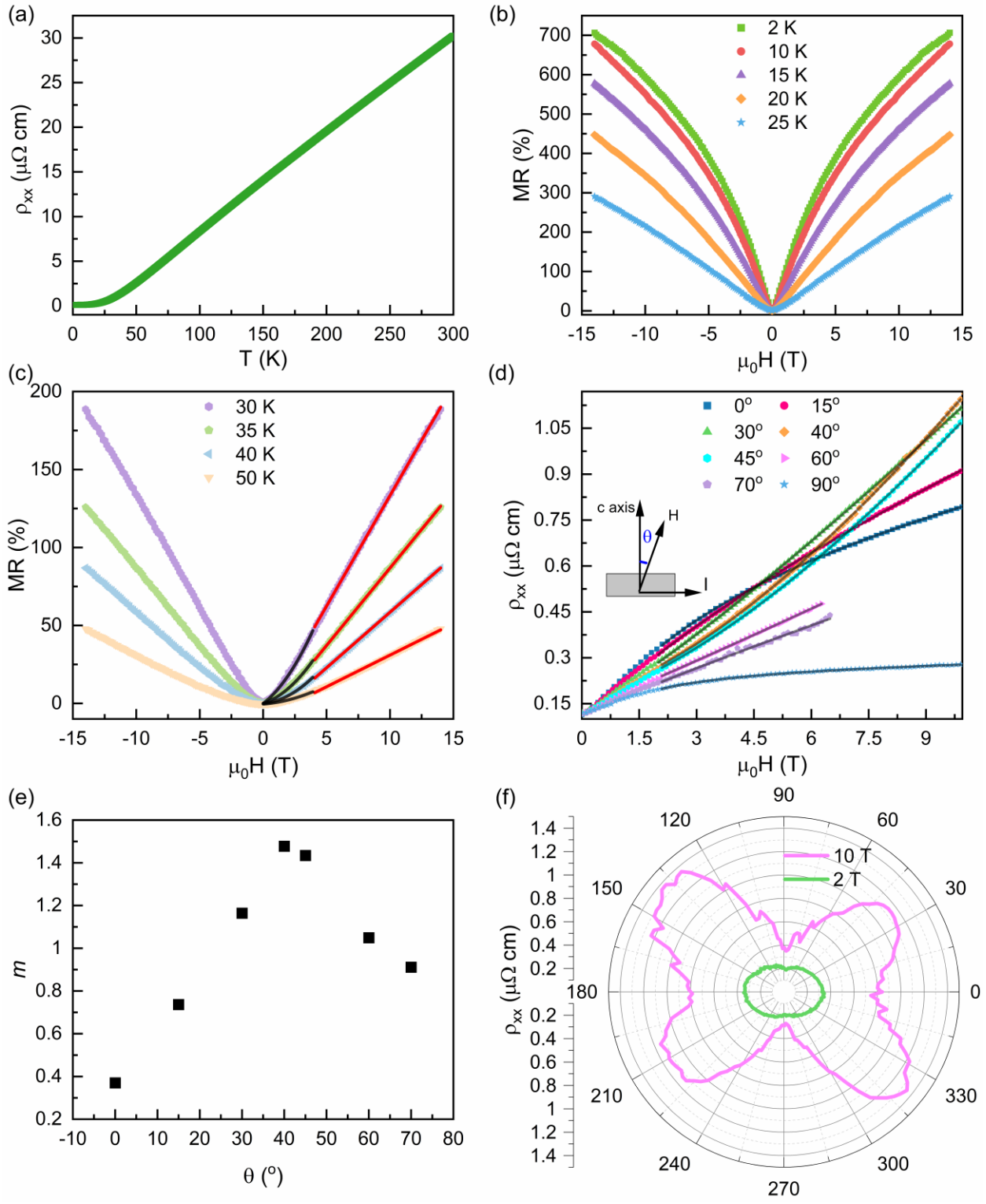

Figure 6.2: (a) Temperature-dependent longitudinal electrical resistivity ρ_{xx} of $NiTe_2$ crystal. (b) Transverse MR in the temperature range from 2 K to 25 K, where MR is defined as $MR = (\rho_{xx}(\mu_0 H) - \rho_{xx}(0))/\rho_{xx}(0)$, where $\rho_{xx}(0)$ and $\rho_{xx}(\mu_0 H)$ are the longitudinal resistivity at zero and $\mu_0 H$ fields, respectively. (c) Transverse MR in the temperature range from 30 K to 50 K. The black and red lines represent the second-order polynomial fittings and the

first-order polynomial fittings, separately. (d) Magnetic field-dependent ρ_{xx} with several tilt angle θ at 2 K. The definition of θ is shown in the inset. The grey lines represent the fittings described in the text. (e) The fitted index *m*. (f) Polar plots of the angular variation of ρ_{xx} at 2 K and under a fixed magnetic field.

Hall carrier density *n* increases as the temperature increases. It should be pointed out that the Hall carrier density is not equal to the real hole- or electron-type carrier density. It is the difference between the densities of these two types of carriers. The inset in Figure 6.3a plots the Hall conductivity σ_{xy} at 2 K. In the standard Bloch–Boltzmann transport, the reciprocal of the peak field $1/B_{max}$ is equal to the mean mobility [142] . Consequently, the mean mobility in the $NiTe_2$ crystal is about 2040 $cm^2\ V^{-1}\ s^{-1}$ at 2 K, which is comparable to the previous study [143].

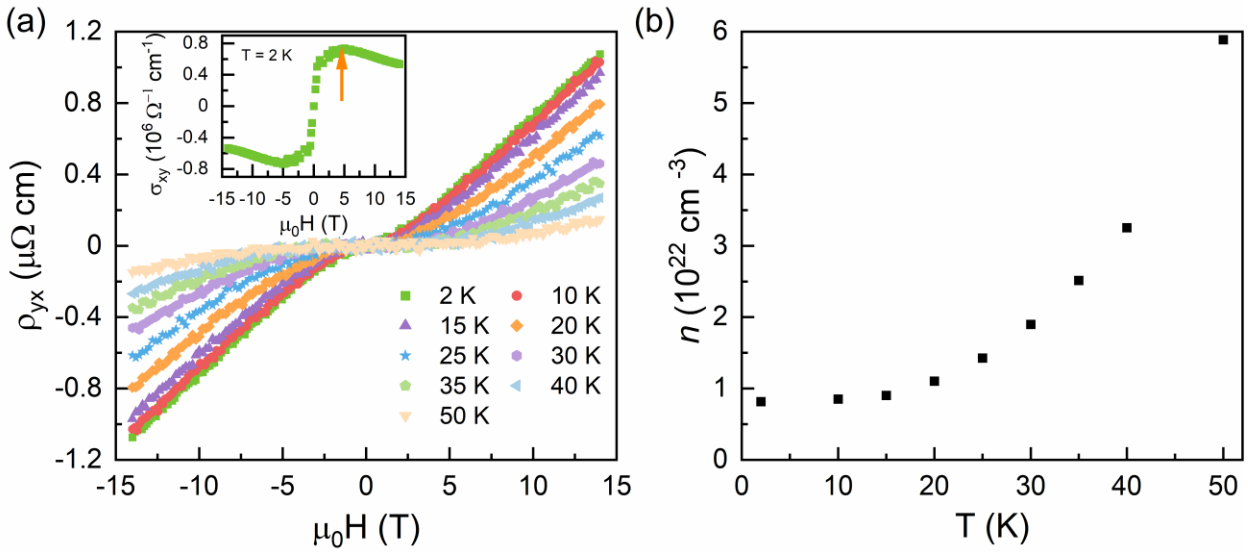

Figure 6.3: (a) Hall resistivity ρ_{yx} of $NiTe_2$ crystal at different temperatures. The inset shows the Hall conductivity σ_{xy} at 2 K. B_{max} is marked by the orange arrow. (b) Hall carrier density at 14 T.

6.3.3 de Haas–van Alphen Quantum Oscillations

The magnetic torque $\tau = VM \times \mu_0 H$, where V is the volume, M is the magnetization, and $\mu_0 H$ is the external applied magnetic field, is measured at different temperatures at $\theta = 2^{\circ}$, where

$\theta = 0^{\circ}$and 90° correspond to the applied magnetic field oriented along the c-axis and along the a-axis, respectively. Figure 6.4a plots the component of the magnetization perpendicular to the applied magnetic field $M_{\perp}$ deduced from the measured τ. Strong de Haas–van Alphen (dHvA) quantum oscillations are observed in the $NiTe_2$ sample. Figure 6.4b plots the oscillatory components in $M_{\perp}$ against $1/(\mu_0 H)$, which are acquired after subtracting the background from the $M_{\perp}$ data. The corresponding fast Fourier transform (FFT) spectra are displayed in Figure 6.4c. There are two major frequencies, 47 T and 400 T, labeled as α and β, respectively, and the peak

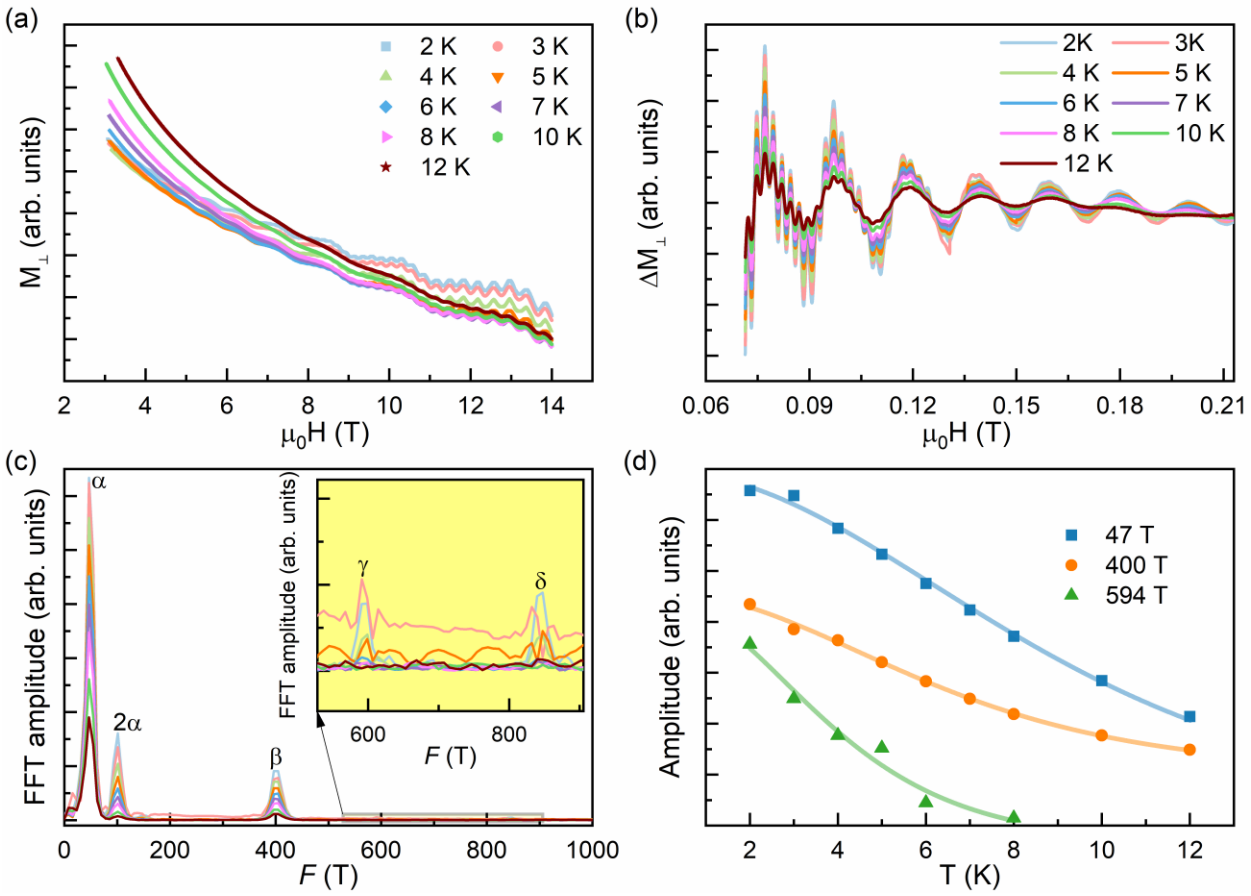

Figure 6.4: (a) $M_{\perp}$ at $\theta = 2^{\circ}$. (b) Oscillatory components in $M_{\perp}$. (c) Corresponding FFT spectra. The inset enlarges the spectra in the range from 500 T to 900 T. (d) Amplitude of peaks in FFT spectra as a function of temperature. Solid lines represent fits to R_T in the LK formula. For the sake of clarity, these data points are rescaled and offset.

corresponding to the 2nd harmonic frequency of α is evident in FFT spectra. Additionally, two weak peaks, γ and δ, located at 594 T and 847 T separately, are found in the spectra. In Figure 6.4d, I plot the FFT amplitude of frequencies, α, β, and γ as a function of temperature. The effective mass of each frequency orbit can be obtained by fitting the amplitude by the thermal damping factor (equation (3.10) in **section *3.3.2***) in the Lifshitz-Kosevich (LK) formula. The values of the obtained effective mass ratio μ, which is defined as the ratio of the effective cyclotron mass m^* to free electron mass m_0, are summarized in Table 6.1. All of these three orbits exhibit a small effective mass.

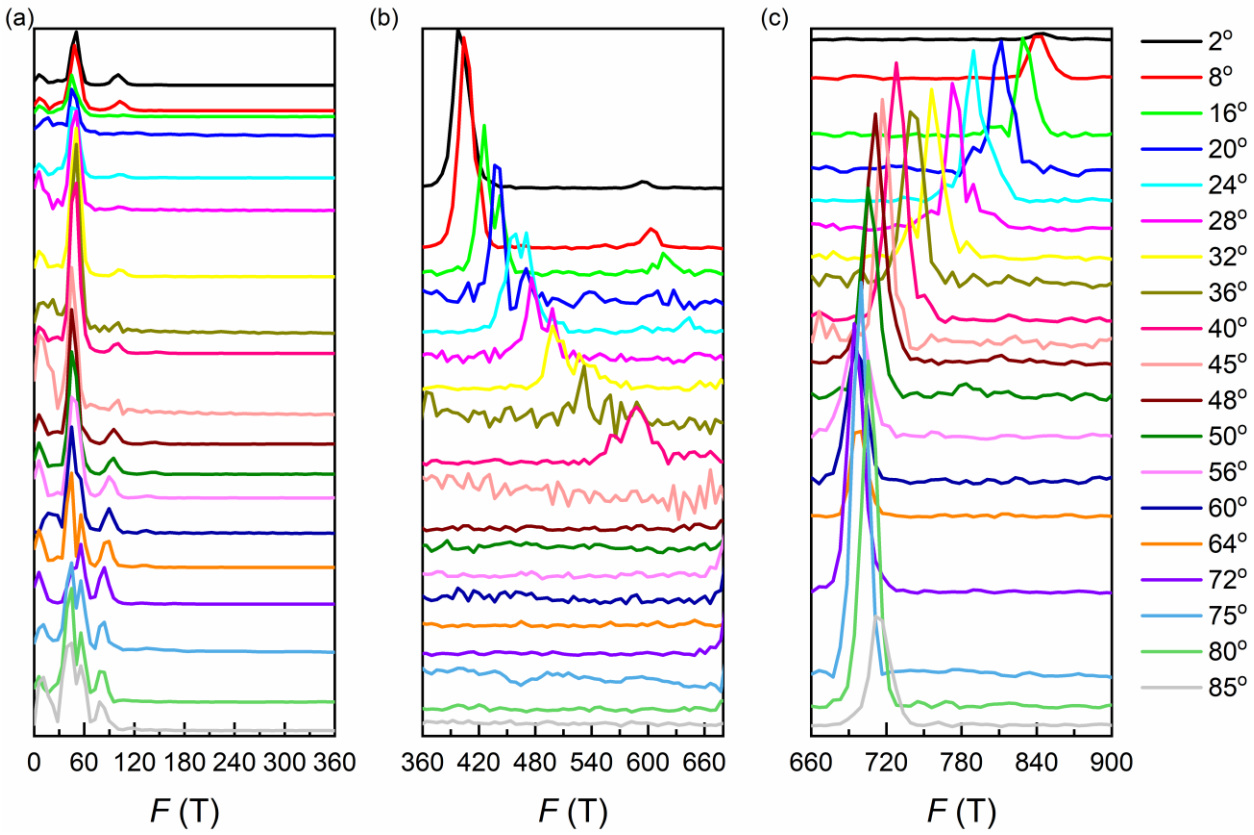

Figure 6.5: FFT spectra of oscillatory components in $M_\perp$ at different angles θ. For the sake of clarity, spectra are rescaled and offset.

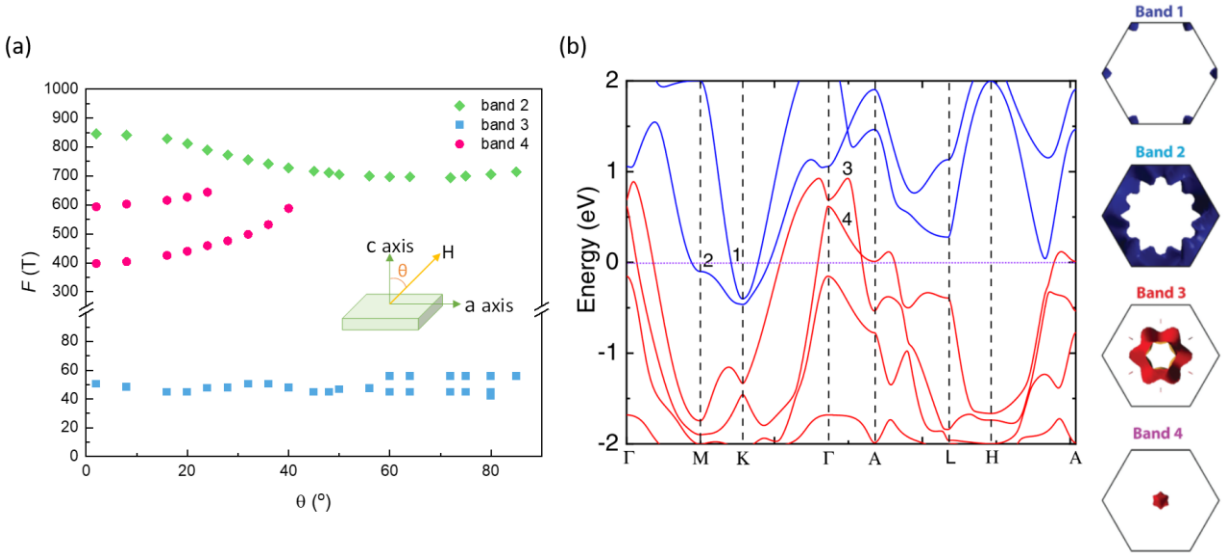

Figure 6.6: (a) dHvA frequencies as a function of θ. The definition of θ is shown in the inset. (b) Electronic band structure of $NiTe_2$ including the spin-orbit coupling (SOC). Bands crossing the E_F are labeled by numbers. The corresponding Fermi surfaces of these bands within the first Brillouin zone are shown on the right. Adapted from reference [143] with permission from the American Physical Society.

Figure 6.5 displays the FFT spectra of the oscillatory components in $M_\perp$ at 2 K and different θ. The oscillation frequencies as a function of θ are plotted in Figure 6.6a. According to the previous study, there are two hole bands and two electron bands crossing the Fermi energy (E_F) in the electronic band structure of $NiTe_2$, which are labeled by numbers in Figure 6.6b. Two hole bands, band 3 and band 4, cross at a Dirac point near the E_F in the Γ-A direction, forming a tilted type-II Dirac cone [143]. The α frequency of value around 50 T is linked to band 3 with a small Fermi surface cross-sectional area, and its value does not change evidently as θ varies. The β and γ frequencies are linked to band 4, and their corresponding peaks disappear in the FFT spectra at θ greater than 40°. The δ frequency, the highest frequency observed in my measurements, results from band 2. The values of β, γ, and δ frequencies vary obviously as θ changes, indicating the anisotropy of the Fermi surfaces of band 2 and band 3, which is consistent with the anisotropic magnetic field-dependent ρ_{xx} discussed in the previous section.

Since band 3 and band 4 are related to the Dirac point near the E_F, it would be interesting to calculate the corresponding Berry phases and quantum mobilities. By using the band filter, the oscillatory components of 47 T, 400 T, and 594 T are separated from the oscillatory signals in $M_\perp$ at 2 K and plotted in Figure 6.7a. The corresponding Landau fan diagrams of each frequency are shown in Figure 6.7b. The minima of $\Delta M_\perp$ are assigned with the Landau level index $n = l - \frac{1}{4}$, where *l* is an integer [28]. The linear fittings of n are represented by the solid lines, which intersect with the *n*-axis at 0.48, 0.35, and 0.34 for 47 T, 400 T, and 594 T orbits. Previous calculation work points out that the 400 T orbit and 594 T orbit are linked to the minimum and maximum Fermi surface cross-sectional areas of band 4, respectively [143]. Therefore, the phase shift ϕ of the 400 T orbit and 594 T orbit are $\frac{1}{8}$ and $-\frac{1}{8}$, respectively. Consequently, the Berry phase φ_B of the 400 T orbit is 0.95π, while that of the 594 T orbit is 0.43π. However, I do not have information about the phase shift of the 47 T orbit. As a result, its Berry phase would be either 0.96π, 1.21π, or 0.71π, depending on the value of the phase shift. All these orbits display a nontrivial Berry phase due to the Dirac point.

According to the field-damping factor (equation (3.11) in **section *3.3.2***) in the LK formula, the quantum relaxation time and mobility can be calculated from the Dingle temperature T_D obtained from the Dingle plot. The Dingle plot of 47 T, 400 T, and 594 T orbits are shown in Figure 6.7c. The Dingle temperature T_D of each orbit is deduced from the slope of the linear fitting of the corresponding Dingle plot. The quantum relaxation time $\tau_q = \hbar/2\pi k_B T_D$ and the quantum mobility μ_q are calculated and summarized in Table 6.1. The quantum mobility μ_q is less than the mobility acquired from the peak of Hall conductivity σ_{xy} in the previous section. This is expected since μ_q is affected by scatterings in all directions, while the transport mobility is not influenced

by small-angle scatterings. The small effective mass and high mobility related to the Dirac point are the reasons for the observed large MR.

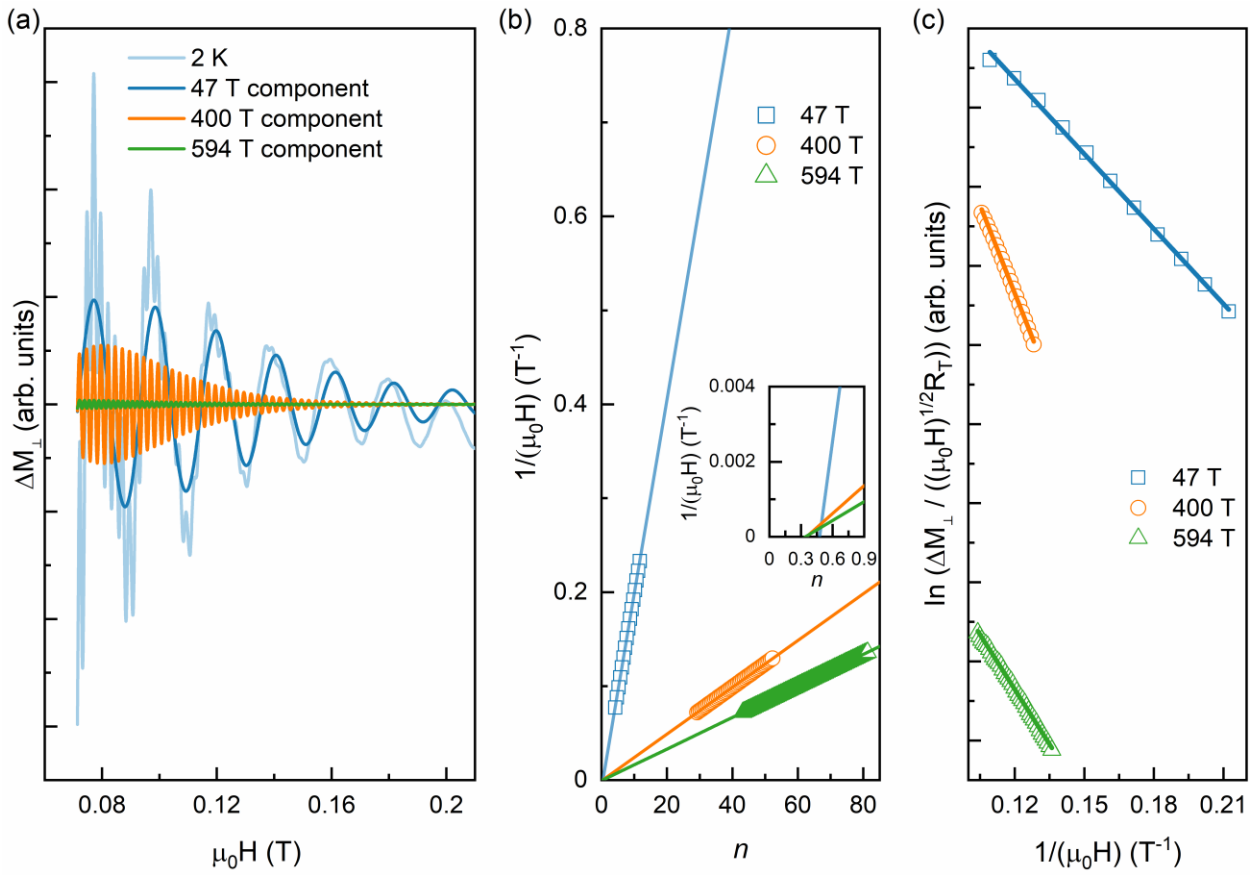

Figure 6.7: (a) The light blue line represents the oscillatory component in $M_{\perp}$ at 2 K and $\theta = 2^{\circ}$. The components related to 47 T, 400 T, and 594 T, which are separated by the band filter, are plotted by the blue, orange, and green lines respectively. (b) Landau fan diagram. The solid lines represent the linear fittings. The inset shows a closer view of the points where the fitting lines intersect with the *n*-axis. (c) Dingle plot. The solid lines are linear fittings of the data points.

Table 6.1: Effective mass ratio μ, Berry phase φ_B, Dingle temperature T_D, quantum relaxation time τ_q, and quantum mobility μ_q of 47 T, 400 T, and 594 T orbits deduced from dHvA oscillation results.

F (T)	μ	φ_B	T_D (K)	τ_q (ps)	μ_q (cm^2 V^{-1} s^{-1})
47 T (α)	0.13	0.96π, when $\phi = 0$ 1.21π, when $\phi = \frac{1}{8}$ 0.71π, when $\phi = -\frac{1}{8}$	8.18	0.149	1988
400 T (β)	0.18	0.95π	13.91	0.087	845
594 T (γ)	0.29	0.43π	5.41	0.225	1357

6.3.4 Thermal Transport Properties

Figure 6.8a plots the temperature-dependent heat capacity c_p of $NiTe_2$ under zero and 14 T applied magnetic fields. Both c_p curves show no signatures of any structural phase transition within the measured temperature range, and the distinction between the two curves is negligible. The inset plots c_p/T versus T^2 below 5 K under zero magnetic field, and the data are fitted with the equation $c_p/T = \gamma + \beta T^2$, where γ is the Sommerfeld coefficient connected to the electronic heat capacity, β is the coefficient of phonons associated with the lattice heat capacity. The fitting result indicates that γ has a value of 6.05 mJ mol^{-1} K^{-2}, and β has a value of 0.59 mJ mol^{-1} K^{-4}, suggesting that the density of states (DOS) at the E_F of $NiTe_2$ is 2.5 states eV^{-1}, and the Debye temperature is 215 K.

Seebeck coefficient S of $NiTe_2$ is shown in Figure 6.9b, which exhibits a small positive value below 4 μV K^{-1} within the measured temperature range. This is not surprising since both holes and electrons contribute to the S in a semimetal, and their contributions partially compensate for each other. The positive sign of S suggests that the contribution of holes dominates S, consistent

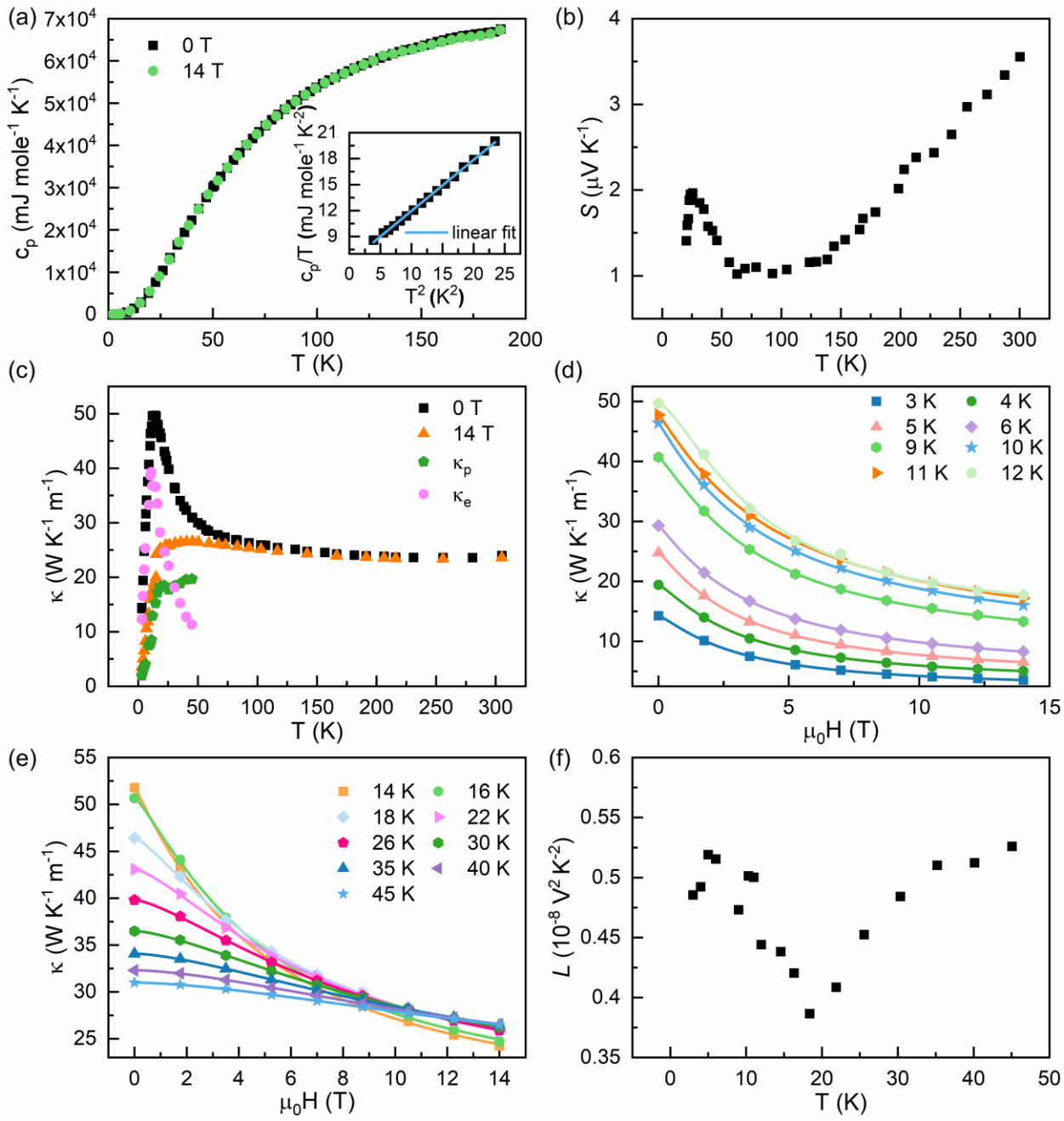

Figure 6.8: (a) Temperature-dependent heat capacity c_p of $NiTe_2$ under zero and 14 T magnetic fields. The inset plots c_p/T versus T^2 below 5 K under zero field, and the data are fitted with the equation $c_p/T = \gamma + \beta T^2$. (b) Seebeck coefficient S under zero magnetic field. (c) Black and orange symbols represent the thermal conductivity κ under zero and 14 T magnetic fields, respectively. The lattice thermal conductivity κ_p and the electronic thermal conductivity κ_e obtained from the fittings in (d) and (e) are shown by green and pink symbols separately. (d)(e) The solid symbols show the magnetic field-dependent thermal conductivity κ at different temperatures. The lines represent the fittings mentioned in the text. (f) Lorenz number L.

with the positive Hall resistivity discussed before. In the temperature range from 150 K to 300 K, *S* decreases as the temperature drops and displays a linear dependence on the temperature, indicating that diffusion is the dominant mechanism of *S*. In the temperature range of 50 K to 150 K, there is no significant variation in *S*. At temperatures below 50 K, *S* initially increases as the temperature drops, culminating in a maximum near 23 K before declining subsequently. This peak in *S* is likely attributed to the phonon-drag effect, which results from carrier-phonon scattering.

The thermal conductivity κ under zero and 14 T magnetic fields are displayed in Figure 6.8c. The zero field κ exhibits a peak at 15 K, with a value of 50 W K^{-1} m^{-1}. Under the field of 14 T, where the field is aligned along the c-axis and perpendicular to the temperature gradient in the ab-plane, the value of κ is significantly suppressed at temperatures below 50 K. In general, κ can be partitioned into two contributions: the lattice thermal conductivity κ_p and the electronic thermal conductivity κ_e. Because the electronic contribution is proportional to the electrical conductivity, and the $NiTe_2$ crystal displays a large MR at low temperatures, the suppressed κ is very likely due to the decreased κ_e caused by the large MR under the applied magnetic field. Since the heat transport by phonons is usually independent of the applied magnetic field, an empirical expression, $\kappa(\mu_0 H, T) = \kappa_p(T) + \kappa_e(T)/[1 + \eta(\mu_0 H)^s]$, can be used to estimate the values of lattice thermal conductivity, $\kappa_p(T)$, and electronic thermal conductivity, $\kappa_e(T)$, at temperature T and zero field [144]. In the expression, η is proportional to the zero-field electronic mean free path, and s is a constant related to the scattering [145]. As shown in Figure 6.8d and e, the magnetic field-dependent κ at different temperatures below 50 K are fitted to this expression. The fitting-obtained $\kappa_p(T)$ and $\kappa_e(T)$ are plotted in Figure 6.8c. Below 30 K, κ_e is larger than κ_p, and κ_e is significantly larger than κ_p as the temperature decreases to a value of 11 K, indicating that the charge carriers dominate κ at the very low temperatures in $NiTe_2$. The Lorenz number $L = \frac{\kappa_e}{\sigma T}$,

where σ is the electrical conductivity at temperature T, is shown in Figure 6.8f. The value of L is much smaller than the Sommerfeld value $L_0 = 2.44 \times 10^{-8}\ \mathrm{V^2K^{-2}}$. Even if I assume that κ is completely contributed by the electronic thermal conductivity and I ignore the lattice contribution, the calculated L is still much smaller than L_0. This suggests that the transport behaviors of charge carriers in $NiTe_2$ dramatically deviate from the free electron model. The strong violation of the Wiedemann-Franz law has also been observed in other topological semimetals, such as WP_2 [146], $NbSb_2$ [147], and $PtSn_4$ [144]. The underlying physics still needs further study.

6.4 Conclusion

In this work, I have investigated the low-temperature electrical and thermal transport properties of type-II Dirac semimetal $NiTe_2$. The single-crystalline $NiTe_2$ sample displays a large MR at low temperatures. The MR value and its magnetic-field dependence are sensitive to the field strength and the angle between the applied magnetic field and the current, indicating the anisotropic feature of the MR. The quantum oscillation results reveal the small effective mass and the nontrivial Berry phase resulting from the Dirac point. By separating the lattice and electronic contributions to the thermal conductivity, the temperature-dependent Lorenz number has been obtained, which strongly deviates from the Sommerfeld value. However, the reasons for the anisotropic and magnetic-field sensitive MR and the violation of the Wiedemann-Franz law are still unclear. Thus, the related computational work would be welcome.

Chapter 7 Conclusion and Future Work

7.1 Summary

This thesis presents analyses of the low-temperature physical properties of three distinct types of topological semimetals I investigated during my doctoral study, with a particular focus on their transport properties.

Chapter 4 discusses the effect of Fe-doping on the magnetic and transport properties of polycrystalline shandite $Co_3Sn_2S_2$. $Co_3Sn_2S_2$ is a ferromagnetic Weyl semimetal, and the Fe-doping largely suppresses its magnetic order and lowers the Curie temperature. Due to its ferromagnetism, it exhibits the anomalous Hall effect (AHE). The AHE is still evident after the Fe-doping, demonstrating the robustness of the AHE originating from the topologically protected nontrivial Berry curvature. On the other hand, the Fe-doping results in the skew-scattering contribution to the AHE and also the Kondo effect observed in the temperature-dependent resistivity, making the anomalous Hall resistivity display a complex behavior at low temperatures. In addition, a hysteresis behavior of the low-magnetic field magnetoresistance (MR) has been detected for the first time in both pure and Fe-doped $Co_3Sn_2S_2$ polycrystals. At last, the thermal spin fluctuation-induced the decrease in the absolute value of the Seebeck coefficient has been discussed.

Chapter 5 focuses on the single crystalline $Ni_3In_2S_2$, which is also a topological semimetal from the shandite family like $Co_3Sn_2S_2$. $Ni_3In_2S_2$ displays an extremely large transverse MR and a magnetic field-induced resistivity upturn behavior at low temperatures. This Chapter aims to find the origin of this giant transverse MR. At temperatures below 50 K, the transverse MR curves

show a linear magnetic field dependence under high magnetic fields, which is beyond the scope of the classical two-band model. Along with magnetotransport measurements, quantum oscillations and computation results indicate that it is the linearly dispersive bands that cause the high mobility and quantum linear MR, thus leading to the giant and linear magnetic field-dependent MR in $Ni_3In_2S_2$.

Chapter 6 presents the electrical and thermal transport properties of the type-II Dirac semimetal $NiTe_2$ single crystal. $NiTe_2$ exhibits a large magnetoresistance at low temperatures. In the temperature range from 2 K to 25 K, the transverse MR curve exhibits a cusp under low fields. At 2 K, the value and the magnetic-field dependence of MR are sensitive to the field strength and the angle between the applied magnetic field and the current. The polar plot of MR shows a butterfly shape at 10 T, which is entirely different from that at 2 T. These suggest that the Fermi surface of $NiTe_2$ is anisotropic and may be affected significantly by the applied magnetic field or the scattering patterns may be changed dramatically by the magnetic field. The dHvA quantum oscillation results reveal the small effective mass and the nontrivial Berry phase originating from the Dirac point. The thermal conductivity is dramatically suppressed by the external magnetic field at temperatures below 50 K, probably due to the large MR of $NiTe_2$. After separating the lattice and the electronic contributions to the thermal conductivity, the temperature-dependent Lorenz number is deduced from the electronic thermal conductivity, which significantly deviates from the Sommerfeld value, indicating the breakdown of the Wiedemann-Franz law.

7.2 Future Work

As pointed out in Chapter 6, there are some unclear questions about the transport properties of $NiTe_2$ that need further study. First, what are the reasons for the anisotropic and magnetic field-sensitive MR? The answers may concern the anisotropic and magnetic field-sensitive Fermi

surface or scattering mechanisms. The second one is why the Lorenz number is so much smaller compared to the Sommerfeld value. The violation of the Wiedemann-Franz law has been reported and well-studied in another topological semimetal, the Weyl semimetal WP_2 [146]. The authors of reference [146] claimed that the breakdown of the Wiedemann-Franz law in WP_2 is due to the hydrodynamic electron flow, i.e., the electron transport is thought to resemble the flow of viscous fluids at low temperatures. However, whether this theory can apply to $NiTe_2$ or if there are other mechanisms that can explain the small Lorenz number is unclear. To solve these questions, computational studies on the electrical and thermal transport in $NiTe_2$ are indispensable.

Another possible project about $NiTe_2$ is about the modulation of the Dirac point position. According to previous calculational and ARPES results, the Dirac point hosted by $NiTe_2$ is not precisely at the E_F. Tuning the E_F by chemical doping or applying pressure may induce new phenomena when the Dirac point is much closer to the E_F.

It is pertinent to note that topological semimetals have captured the attention of researchers not only in the realm of fundamental science but also in the context of industrial applications. $Co_3Sn_2S_2$ single crystal, for instance, exhibits a large AHE and anomalous Nerst effect due to the enhanced Berry curvature, making it an excellent candidate for AHE sensors and low-power thermoelectric devices [148]. My discovery of the extremely large MR in $Ni_3In_2S_2$ single crystal suggests that this material can be utilized in the development of magnetic field sensors. Future investigations can focus on how to further enhance these properties.

In the domain of fundamental scientific research, it is important to obtain materials that are as pure as possible. This enables researchers to concentrate on the desired characteristics without any extraneous influences. Consequently, numerous researchers are searching for topological

semimetals that possess Dirac/Weyl points close to or at the E_F without other topologically trivial bands in the vicinity.

However, in applied science, the aim is to improve the performance of the material/device. Therefore, the addition of impurities and greater complexity in the material can sometimes be advantageous. A case in point is the study conducted on the Fe-doped $Co_3Sn_2S_2$ single crystal, which revealed that a small amount of Fe dopant can significantly enhance the anomalous Hall conductivity and anomalous Hall angle due to the dopant-induced extrinsic contribution to the AHE [79]. Therefore, exploiting the intrinsic characteristics of topological semimetals while simultaneously introducing necessary extrinsic contributions should be a research direction for the applications of topological semimetals.

Appendix: High-Temperature Hall Effect Measurements on Thermoelectric Materials

In my doctoral study, in addition to my own projects on topological semimetals, I carried out extensive measurements of the high-temperature Hall effect (HTHE) on numerous thermoelectric (TE) materials as part of the collaboration of Prof. Uher's group with other research teams. In this appendix, I will briefly introduce the HTHE measurements.

The HTHE was measured using a homemade instrument, as shown in Figure A.1a. The Hall resistance was monitored by a Linear Research AC resistance bridge (LR-700) under a reversible magnetic field of 0.5 T generated by the Oxford superconducting magnet. The sample was prepared by cutting the bulk material into a thin cuboid that had dimensions of approximately $1\ \text{mm} \times 2\ \text{mm} \times 7\ \text{mm}$, which was then mounted to the sample holder adopting the Hall bar geometry as illustrated in Figure A.1b. To prevent the sample from oxidizing at high temperatures, the sample holder was sealed into a quartz tube and filled with Argon gas after pumping.

The performance of a TE material is characterized by its figure of merit, $zT = S^2\sigma T\kappa^{-1}$, where S is the Seebeck coefficient, σ is the electrical conductivity, T is the absolute temperature, and κ is the thermal conductivity. Since the electrical resistivity is closely linked to the carrier density and mobility, which can be derived from the Hall measurements, the HTHE measurements are essential to the study of TE materials. The instrument in Prof. Uher's lab can measure the Hall effect in the temperature range from room temperature to 500 ℃, which is the working temperature range of TE materials. The Hall carrier density P_H and mobility μ_H were calculated through equations $P_H = 1/eR_H$ and $\mu_H = \sigma R_H$, where e is the elementary charge, and R_H is the Hall coefficient extracted from the HTHE measurements.

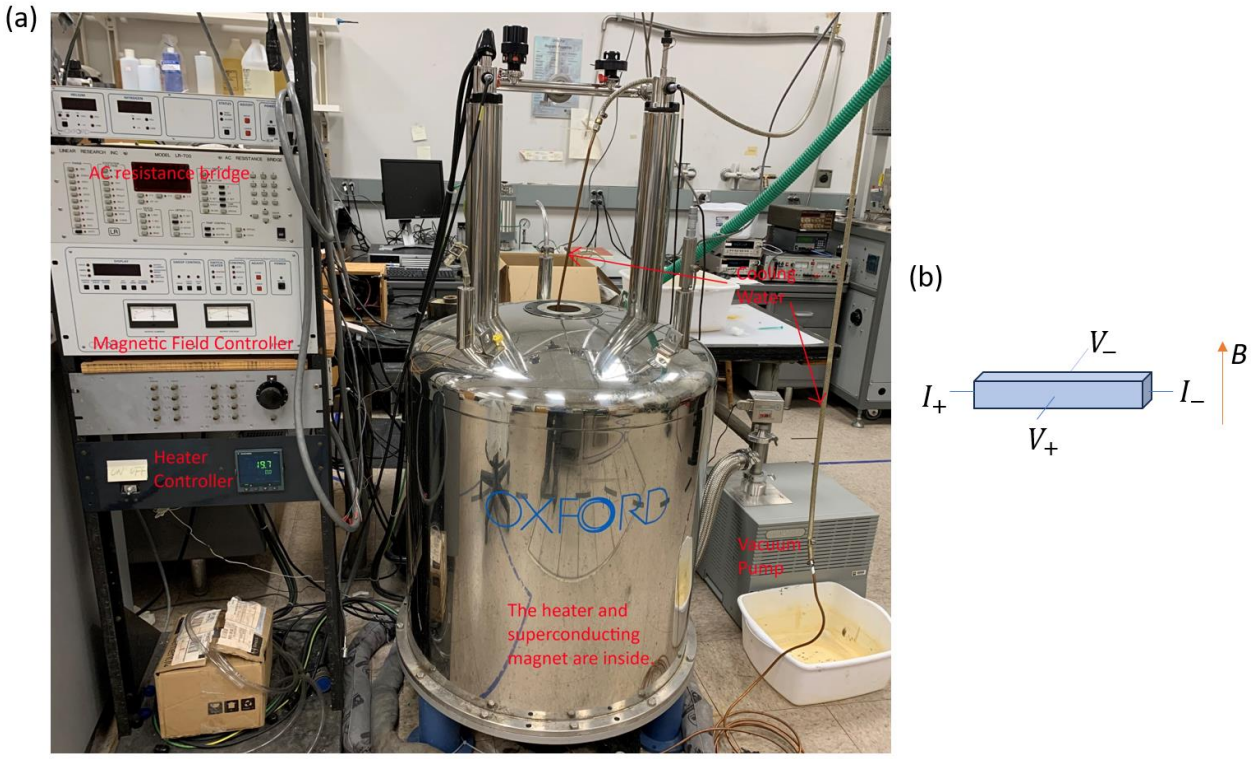

Figure A.1: (a) Photo of the instrument used for high-temperature Hall effect measurements. (b) A Hall bar: the Hall effect measurement setup.

Here, I present the temperature-dependent Hall carrier density and mobility of the $(1-x)Cu_2Se/(x)Cu_4TiSe_4$ composites obtained from the HTHE measurements, which have been published in one of my co-authored papers with Prof. Pierre Poudeu's group [149]. The $(1-x)Cu_2Se/(x)Cu_4TiSe_4$ composites with x = 0.01 and 0.02 have an average zT of 0.84 and 0.74 separately, exhibiting an increase of about 40% compared with the average zT of pristine Cu_2Se and outperform other Cu_2Se-based TE materials. Taking the following analysis as an example, I will show how the HTHE measurements play a key role in studying the underlying physics of electrical transport properties of TE materials.

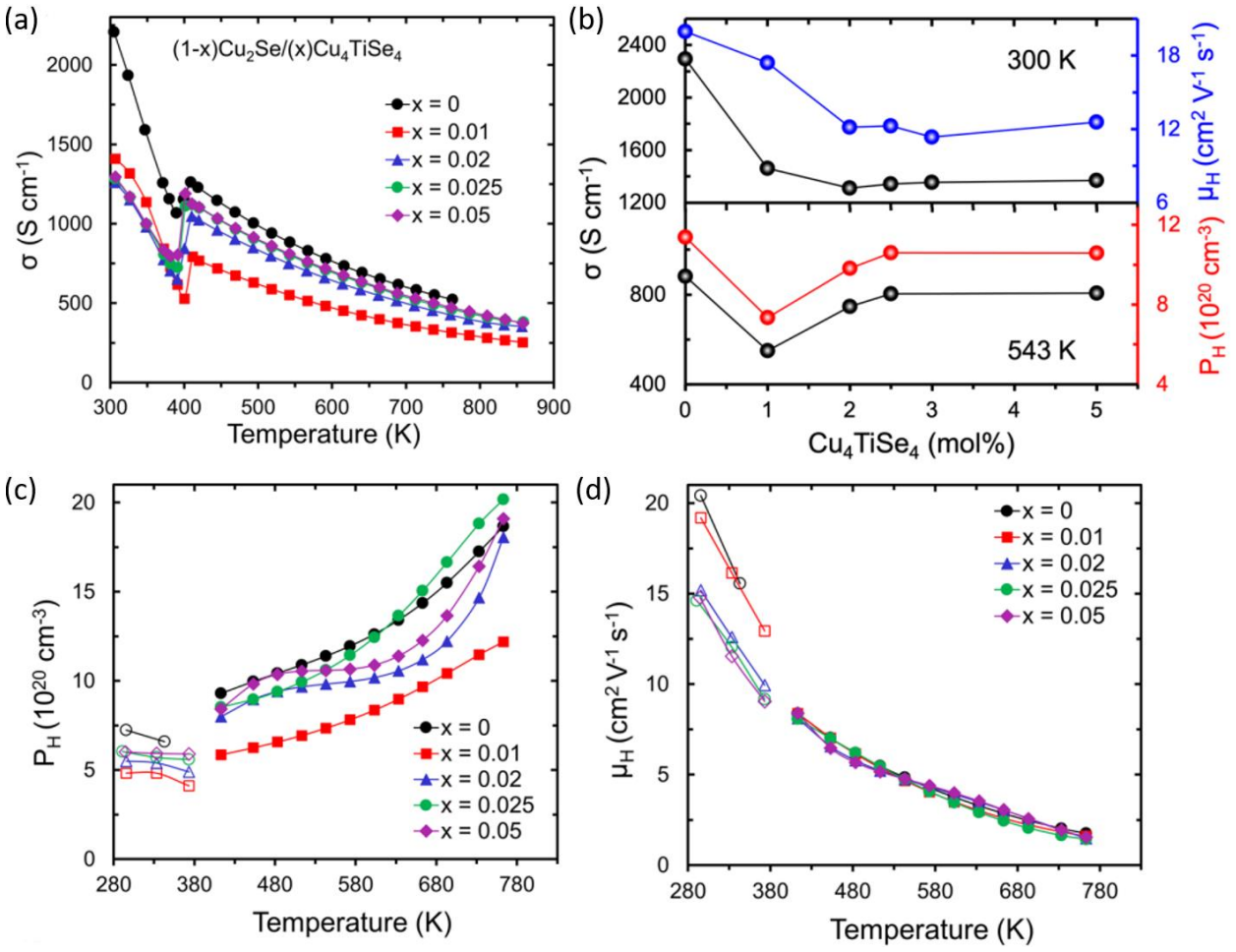

Figure A.2: Electrical transport properties of the $(1-x)Cu_2Se/(x)Cu_4TiSe_4$ composites. (a)Temperature-dependent electrical conductivity. (b) Change in the electrical conductivity, carrier mobility (300 K), and carrier concentration (543 K) with the content of Cu_4TiSe_4. (c) carrier concentration, and (d) carrier mobility. The empty and solid symbols in (c) and (d) denote the data before and after the phase transition. Adapted with permission from reference [149]. Copyright 2024 American Chemical Society.

Figure A.2a displays the temperature-dependent electrical conductivity of the $(1-x)Cu_2Se/(x)Cu_4TiSe_4$ composites. The sharp drop at ~400 K corresponds to the phase transition of Cu_2Se, i.e., from monoclinic α-Cu_2Se to cubic β-Cu_2Se. Figure A.2b demonstrates that the carrier mobility dominates the trend in the electrical conductivity at 300 K when α-Cu_2Se is the sample matrix, while the carrier concentration takes over the variation in the electrical conductivity at 543 K when β-Cu_2Se is coexisting with Cu_4TiSe_4. As shown in Figure A.2c and d, near room

temperature, for the sample with $x = 0.01$, the mobility is almost not influenced by the addition of Ti. However, the carrier density is evidently decreased by the addition of Ti. This is consistent with the XRD and EDS results of the sample, indicating that the added Ti atoms occupied the interstitial sites in the α-Cu_2Se lattice, which have a large amount of cation vacancies, and serve as electron donors. With higher Ti concentration, the addition of Ti introduces the cubic Cu_4TiSe_4 phase and results in distorted phase boundaries due to the lattice mismatch with the monoclinic α-Cu_2Se, leading to a drop in mobility. At the same time, the formation of the Cu_4TiSe_4 phase decreases the solubility of Ti atoms in the α-Cu_2Se lattice, thus decreases the number of electron donors and increases the hole-type carrier density.

At temperatures above 400 K, the α-Cu_2Se transited into the β-Cu_2Se. Because of the intimate lattice coherency between the cubic β-Cu_2Se and cubic Cu_4TiSe_4 phases, the mobility is independent of the Ti concentration. However, the carrier density is still obviously affected by the Ti concentration. This reveals that introducing a secondary phase with similar lattice parameters and structure can modulate the carrier density without decreasing the mobility, which offers an instructive approach to improving the performance of TE materials.

The above analysis is based on the results of HTHE measurements, which highlights the necessity and importance of such measurements when investigating electrical transport and its connection to the lattice structures of TE materials.

Bibliography

[1] K.v. Klitzing, G. Dorda, M. Pepper, New Method for High-Accuracy Determination of the Fine-Structure Constant Based on Quantized Hall Resistance, Physical Review Letters 45 (1980) 494-497.
[2] R.B. Laughlin, Quantized Hall conductivity in two dimensions, Physical Review B 23 (1981) 5632-5633.
[3] D.C. Tsui, H.L. Stormer, A.C. Gossard, Two-Dimensional Magnetotransport in the Extreme Quantum Limit, Physical Review Letters 48 (1982) 1559-1562.
[4] R.B. Laughlin, Anomalous Quantum Hall Effect: An Incompressible Quantum Fluid with Fractionally Charged Excitations, Physical Review Letters 50 (1983) 1395-1398.
[5] L. Fu, C.L. Kane, Topological insulators with inversion symmetry, Physical Review B 76 (2007) 045302.
[6] L. Fu, C.L. Kane, E.J. Mele, Topological Insulators in Three Dimensions, Physical Review Letters 98 (2007) 106803.
[7] D. Hsieh, D. Qian, L. Wray, Y. Xia, Y.S. Hor, R.J. Cava, M.Z. Hasan, A topological Dirac insulator in a quantum spin Hall phase, Nature 452 (2008) 970-974.
[8] J.E. Moore, The birth of topological insulators, Nature 464 (2010) 194-198.
[9] X. Wan, A.M. Turner, A. Vishwanath, S.Y. Savrasov, Topological semimetal and Fermi-arc surface states in the electronic structure of pyrochlore iridates, Physical Review B 83 (2011) 205101.
[10] Z. Wang, Y. Sun, X.-Q. Chen, C. Franchini, G. Xu, H. Weng, X. Dai, Z. Fang, Dirac semimetal and topological phase transitions in A_3Bi (A =Na, K, Rb), Physical Review B 85 (2012) 195320.
[11] B.Q. Lv, T. Qian, H. Ding, Experimental perspective on three-dimensional topological semimetals, Reviews of Modern Physics 93 (2021) 025002.
[12] S.-Y. Xu, C. Liu, S.K. Kushwaha, R. Sankar, J.W. Krizan, I. Belopolski, M. Neupane, G. Bian, N. Alidoust, T.-R. Chang, H.-T. Jeng, C.-Y. Huang, W.-F. Tsai, H. Lin, P.P. Shibayev, F.-C. Chou, R.J. Cava, M.Z. Hasan, Observation of Fermi arc surface states in a topological metal, Science 347 (2015) 294-298.
[13] A.C. Potter, I. Kimchi, A. Vishwanath, Quantum oscillations from surface Fermi arcs in Weyl and Dirac semimetals, Nature Communications 5 (2014) 5161.
[14] H. Li, H.-W. Wang, H. He, J. Wang, S.-Q. Shen, Giant anisotropic magnetoresistance and planar Hall effect in the Dirac semimetal Cd_3As_2, Physical Review B 97 (2018) 201110.
[15] X. Huang, L. Zhao, Y. Long, P. Wang, D. Chen, Z. Yang, H. Liang, M. Xue, H. Weng, Z. Fang, X. Dai, G. Chen, Observation of the Chiral-Anomaly-Induced Negative Magnetoresistance in 3D Weyl Semimetal TaAs, Physical Review X 5 (2015) 031023.
[16] A.A. Burkov, Anomalous Hall Effect in Weyl Metals, Physical Review Letters 113 (2014) 187202.

[17] M. Ikhlas, T. Tomita, T. Koretsune, M.-T. Suzuki, D. Nishio-Hamane, R. Arita, Y. Otani, S. Nakatsuji, Large anomalous Nernst effect at room temperature in a chiral antiferromagnet, Nature Physics 13 (2017) 1085-1090.
[18] R. Zivieri, S. Lumetti, J. Létang, High-Mobility Topological Semimetals as Novel Materials for Huge Magnetoresistance Effect and New Type of Quantum Hall Effect, Materials 16 (2023) 7579.
[19] M. König, S. Wiedmann, C. Brüne, A. Roth, H. Buhmann, L.W. Molenkamp, X.-L. Qi, S.-C. Zhang, Quantum Spin Hall Insulator State in HgTe Quantum Wells, Science 318 (2007) 766-770.
[20] C.-Z. Chang, J. Zhang, X. Feng, J. Shen, Z. Zhang, M. Guo, K. Li, Y. Ou, P. Wei, L.-L. Wang, Z.-Q. Ji, Y. Feng, S. Ji, X. Chen, J. Jia, X. Dai, Z. Fang, S.-C. Zhang, K. He, Y. Wang, L. Lu, X.-C. Ma, Q.-K. Xue, Experimental Observation of the Quantum Anomalous Hall Effect in a Magnetic Topological Insulator, Science 340 (2013) 167-170.
[21] A.H. Castro Neto, F. Guinea, N.M.R. Peres, K.S. Novoselov, A.K. Geim, The electronic properties of graphene, Reviews of Modern Physics 81 (2009) 109-162.
[22] H. Huang, K.-H. Jin, F. Liu, Black-hole horizon in the Dirac semimetal $Zn_2In_2S_5$, Physical Review B 98 (2018) 121110.
[23] Z.K. Liu, B. Zhou, Y. Zhang, Z.J. Wang, H.M. Weng, D. Prabhakaran, S.-K. Mo, Z.X. Shen, Z. Fang, X. Dai, Z. Hussain, Y.L. Chen, Discovery of a Three-Dimensional Topological Dirac Semimetal, Na_3Bi, Science 343 (2014) 864-867.
[24] S.M. Young, S. Zaheer, J.C.Y. Teo, C.L. Kane, E.J. Mele, A.M. Rappe, Dirac Semimetal in Three Dimensions, Physical Review Letters 108 (2012) 140405.
[25] B. Yan, C. Felser, Topological Materials: Weyl Semimetals, Annual Review of Condensed Matter Physics 8 (2017) 337-354.
[26] B.Q. Lv, H.M. Weng, B.B. Fu, X.P. Wang, H. Miao, J. Ma, P. Richard, X.C. Huang, L.X. Zhao, G.F. Chen, Z. Fang, X. Dai, T. Qian, H. Ding, Experimental Discovery of Weyl Semimetal TaAs, Physical Review X 5 (2015) 031013.
[27] L.X. Yang, Z.K. Liu, Y. Sun, H. Peng, H.F. Yang, T. Zhang, B. Zhou, Y. Zhang, Y.F. Guo, M. Rahn, D. Prabhakaran, Z. Hussain, S.K. Mo, C. Felser, B. Yan, Y.L. Chen, Weyl semimetal phase in the non-centrosymmetric compound TaAs, Nature Physics 11 (2015) 728-732.
[28] J. Hu, S.-Y. Xu, N. Ni, Z. Mao, Transport of Topological Semimetals, Annual Review of Materials Research 49 (2019) 207-252.
[29] Y. Kim, B.J. Wieder, C.L. Kane, A.M. Rappe, Dirac Line Nodes in Inversion-Symmetric Crystals, Physical Review Letters 115 (2015) 036806.
[30] G. Xu, H. Weng, Z. Wang, X. Dai, Z. Fang, Chern Semimetal and the Quantized Anomalous Hall Effect in $HgCr_2Se_4$, Physical Review Letters 107 (2011) 186806.
[31] Y. Chen, Y.-M. Lu, H.-Y. Kee, Topological crystalline metal in orthorhombic perovskite iridates, Nature Communications 6 (2015) 6593.
[32] Q.-F. Liang, J. Zhou, R. Yu, Z. Wang, H. Weng, Node-surface and node-line fermions from nonsymmorphic lattice symmetries, Physical Review B 93 (2016) 085427.
[33] A.B. Pippard, Magnetoresistance in Metals, Cambridge University Press1989.
[34] N.H. Jo, Y. Wu, L.-L. Wang, P.P. Orth, S.S. Downing, S. Manni, D. Mou, D.D. Johnson, A. Kaminski, S.L. Bud'ko, P.C. Canfield, Extremely large magnetoresistance and Kohler's rule in $PdSn_4$: A complete study of thermodynamic, transport, and band-structure properties, Physical Review B 96 (2017) 165145.

[35] S. Sun, Q. Wang, P.-J. Guo, K. Liu, H. Lei, Large magnetoresistance in LaBi: origin of field-induced resistivity upturn and plateau in compensated semimetals, New Journal of Physics 18 (2016) 082002.
[36] F.C. Chen, H.Y. Lv, X. Luo, W.J. Lu, Q.L. Pei, G.T. Lin, Y.Y. Han, X.B. Zhu, W.H. Song, Y.P. Sun, Extremely large magnetoresistance in the type-II Weyl semimetal $MoTe_2$, Physical Review B 94 (2016) 235154.
[37] J. Yang, Z.-Y. Song, L. Guo, H. Gao, Z. Dong, Q. Yu, R.-K. Zheng, T.-T. Kang, K. Zhang, Nontrivial Giant Linear Magnetoresistance in Nodal-Line Semimetal ZrGeSe 2D Layers, Nano Letters 21 (2021) 10139-10145.
[38] S. Zhang, Y. Wang, Q. Zeng, J. Shen, X. Zheng, J. Yang, Z. Wang, C. Xi, B. Wang, M. Zhou, R. Huang, H. Wei, Y. Yao, S. Wang, S.S.P. Parkin, C. Felser, E. Liu, B. Shen, Scaling of Berry-curvature monopole dominated large linear positive magnetoresistance, Proceedings of the National Academy of Sciences 119 (2022) e2208505119.
[39] A.A. Abrikosov, Quantum magnetoresistance, Physical Review B 58 (1998) 2788-2794.
[40] J. Xiong, S.K. Kushwaha, T. Liang, J.W. Krizan, M. Hirschberger, W. Wang, R.J. Cava, N.P. Ong, Evidence for the chiral anomaly in the Dirac semimetal Na_3Bi, Science 350 (2015) 413-416.
[41] E.H. Hall, On a New Action of the Magnet on Electric Currents, American Journal of Mathematics 2 (1879) 287-292.
[42] N. Nagaosa, J. Sinova, S. Onoda, A.H. MacDonald, N.P. Ong, Anomalous Hall effect, Reviews of Modern Physics 82 (2010) 1539-1592.
[43] R. Karplus, J.M. Luttinger, Hall Effect in Ferromagnetics, Physical Review 95 (1954) 1154-1160.
[44] Q. Wang, Y. Xu, R. Lou, Z. Liu, M. Li, Y. Huang, D. Shen, H. Weng, S. Wang, H. Lei, Large intrinsic anomalous Hall effect in half-metallic ferromagnet $Co_3Sn_2S_2$ with magnetic Weyl fermions, Nature Communications 9 (2018) 3681.
[45] P. Li, J. Koo, W. Ning, J. Li, L. Miao, L. Min, Y. Zhu, Y. Wang, N. Alem, C.-X. Liu, Z. Mao, B. Yan, Giant room temperature anomalous Hall effect and tunable topology in a ferromagnetic topological semimetal Co_2MnAl, Nature Communications 11 (2020) 3476.
[46] S. Nakatsuji, N. Kiyohara, T. Higo, Large anomalous Hall effect in a non-collinear antiferromagnet at room temperature, Nature 527 (2015) 212-215.
[47] J. Smit, The spontaneous hall effect in ferromagnetics I, Physica 21 (1955) 877-887.
[48] J. Smit, The spontaneous hall effect in ferromagnetics II, Physica 24 (1958) 39-51.
[49] L. Berger, Influence of spin-orbit interaction on the transport processes in ferromagnetic nickel alloys, in the presence of a degeneracy of the 3d band, Physica 30 (1964) 1141-1159.
[50] M. Matusiak, J.R. Cooper, D. Kaczorowski, Thermoelectric quantum oscillations in ZrSiS, Nature Communications 8 (2017) 15219.
[51] P.J.W. Moll, A.C. Potter, N.L. Nair, B.J. Ramshaw, K.A. Modic, S. Riggs, B. Zeng, N.J. Ghimire, E.D. Bauer, R. Kealhofer, F. Ronning, J.G. Analytis, Magnetic torque anomaly in the quantum limit of Weyl semimetals, Nature Communications 7 (2016) 12492.
[52] A.A. Abrikosov, Quantum linear magnetoresistance, Europhysics Letters 49 (2000) 789.
[53] A.A. Abrikosov, Quantum magnetoresistance of layered semimetals, Physical Review B 60 (1999) 4231-4234.
[54] K. Momma, F. Izumi, VESTA 3 for three-dimensional visualization of crystal, volumetric and morphology data, Journal of Applied Crystallography 44 (2011) 1272-1276.

[55] S. Natarajan, G.V.S. Rao, R. Baskaran, T.S. Radhakrishnan, Synthesis and electrical properties of shandite-parkerite phases, $A_2M_3Ch_2$, Journal of the Less Common Metals 138 (1988) 215-224.
[56] P. Vaqueiro, G.G. Sobany, A powder neutron diffraction study of the metallic ferromagnet $Co_3Sn_2S_2$, Solid State Sciences 11 (2009) 513-518.
[57] D.F. Liu, A.J. Liang, E.K. Liu, Q.N. Xu, Y.W. Li, C. Chen, D. Pei, W.J. Shi, S.K. Mo, P. Dudin, T. Kim, C. Cacho, G. Li, Y. Sun, L.X. Yang, Z.K. Liu, S.S.P. Parkin, C. Felser, Y.L. Chen, Magnetic Weyl semimetal phase in a Kagomé crystal, Science 365 (2019) 1282-1285.
[58] M.N. Ali, J. Xiong, S. Flynn, J. Tao, Q.D. Gibson, L.M. Schoop, T. Liang, N. Haldolaarachchige, M. Hirschberger, N.P. Ong, R.J. Cava, Large, non-saturating magnetoresistance in WTe_2, Nature 514 (2014) 205-208.
[59] C. Shekhar, A.K. Nayak, Y. Sun, M. Schmidt, M. Nicklas, I. Leermakers, U. Zeitler, Y. Skourski, J. Wosnitza, Z. Liu, Y. Chen, W. Schnelle, H. Borrmann, Y. Grin, C. Felser, B. Yan, Extremely large magnetoresistance and ultrahigh mobility in the topological Weyl semimetal candidate NbP, Nature Physics 11 (2015) 645-649.
[60] R. Niu, W.K. Zhu, Materials and possible mechanisms of extremely large magnetoresistance: a review, Journal of Physics: Condensed Matter 34 (2021) 113001.
[61] E. Liu, Y. Sun, N. Kumar, L. Müchler, A. Sun, L. Jiao, S.Y. Yang, D. Liu, A. Liang, Q. Xu, J. Kroder, V. Süß, H. Borrmann, C. Shekhar, Z. Wang, C. Xi, W. Wang, W. Schnelle, S. Wirth, Y. Chen, S.T.B. Goennenwein, C. Felser, Giant anomalous Hall effect in a ferromagnetic Kagomé-lattice semimetal, Nat Phys 14 (2018) 1125-1131.
[62] S. Nakatsuji, R. Arita, Topological Magnets: Functions Based on Berry Phase and Multipoles, Annual Review of Condensed Matter Physics 13 (2022) 119-142.
[63] D.F. Liu, E.K. Liu, Q.N. Xu, J.L. Shen, Y.W. Li, D. Pei, A.J. Liang, P. Dudin, T.K. Kim, C. Cacho, Y.F. Xu, Y. Sun, L.X. Yang, Z.K. Liu, C. Felser, S.S.P. Parkin, Y.L. Chen, Direct observation of the spin–orbit coupling effect in magnetic Weyl semimetal $Co_3Sn_2S_2$, npj Quantum Materials 7 (2022) 11.
[64] S. Howard, L. Jiao, Z. Wang, N. Morali, R. Batabyal, P. Kumar-Nag, N. Avraham, H. Beidenkopf, P. Vir, E. Liu, C. Shekhar, C. Felser, T. Hughes, V. Madhavan, Evidence for one-dimensional chiral edge states in a magnetic Weyl semimetal $Co_3Sn_2S_2$, Nature Communications 12 (2021) 4269.
[65] M. Holder, Y.S. Dedkov, A. Kade, H. Rosner, W. Schnelle, A. Leithe-Jasper, R. Weihrich, S.L. Molodtsov, Photoemission study of electronic structure of the half-metallic ferromagnet $Co_3Sn_2S_2$, Physical Review B 79 (2009) 205116.
[66] L. Jiao, Q. Xu, Y. Cheon, Y. Sun, C. Felser, E. Liu, S. Wirth, Signatures for half-metallicity and nontrivial surface states in the kagome lattice Weyl semimetal $Co_3Sn_2S_2$, Physical Review B 99 (2019) 245158.
[67] S. Rathod, M. Malasi, A. Lakhani, D. Kumar, Electron-magnon scattering in an anisotropic half-metallic ferromagnetic Weyl semimetal $Co_3Sn_2S_2$, Physical Review Materials 6 (2022) 084202.
[68] J. Corps, P. Vaqueiro, A.V. Powell, $Co_3M_2S_2$ (M = Sn, In) shandites as tellurium-free thermoelectrics, Journal of Materials Chemistry A 1 (2013) 6553-6557.
[69] P. Mangelis, P. Vaqueiro, J.C. Jumas, I. da Silva, R.I. Smith, A.V. Powell, The effect of electron and hole doping on the thermoelectric properties of shandite-type $Co_3Sn_2S_2$, J. Solid State Chem. 251 (2017) 204-210.

[70] M. Fujioka, T. Shibuya, J. Nakai, K. Yoshiyasu, Y. Sakai, Y. Takano, Y. Kamihara, M. Matoba, The effect of simultaneous substitution on the electronic band structure and thermoelectric properties of Se-doped Co_3SnInS_2 with the Kagome lattice, Solid State Communications 199 (2014) 56-60.
[71] J. Corps, P. Vaqueiro, A. Aziz, R. Grau-Crespo, W. Kockelmann, J.-C. Jumas, A.V. Powell, Interplay of Metal-Atom Ordering, Fermi Level Tuning, and Thermoelectric Properties in Cobalt Shandites $Co_3M_2S_2$ (M = Sn, In), Chemistry of Materials 27 (2015) 3946-3956.
[72] P. Mangelis, P. Vaqueiro, A.V. Powell, Improved Thermoelectric Performance through Double Substitution in Shandite-Type Mixed-Metal Sulfides, ACS Appl Energy Mater 3 (2020) 2168-2174.
[73] Y. Zhao, Y. Zhu, F. Jiang, Y. Li, Y. Meng, Y. Guo, Q. Li, Z. Huang, S. Zhang, R. Zhang, J.C. Ho, Q. Zhang, W. Liu, C. Zhi, Vacancy Modulating $Co_3Sn_2S_2$ Topological Semimetal for Aqueous Zinc-Ion Batteries, Angewandte Chemie 134 (2022) e202111826.
[74] R. Xie, T. Zhang, H. Weng, G.-L. Chai, Progress, Advantages, and Challenges of Topological Material Catalysts, Small Science (2022) 2100106.
[75] M. Yan, Y. Jin, X. Hou, Y. Guo, A. Tsaturyan, A. Makarova, D. Smirnov, Y. Dedkov, E. Voloshina, Topological Quasi-2D Semimetal $Co_3Sn_2S_2$: Insights into Electronic Structure from NEXAFS and Resonant Photoelectron Spectroscopy, The Journal of Physical Chemistry Letters 12 (2021) 9807-9811.
[76] K. Takasan, T. Morimoto, J. Orenstein, J.E. Moore, Current-induced second harmonic generation in inversion-symmetric Dirac and Weyl semimetals, Physical Review B 104 (2021) L161202.
[77] M.A. Kassem, Y. Tabata, T. Waki, H. Nakamura, Structure and magnetic properties of flux grown single crystals of $Co_{3-x}Fe_xSn_2S_2$ shandites, J. Solid State Chem. 233 (2016) 8-13.
[78] Y. Sakai, R. Tanakadate, M. Matoba, I. Yamada, N. Nishiyama, T. Irifune, K. Funakoshi, T. Kunimoto, Y. Higo, Y. Kamihara, Magnetic Properties of Shandite-Phase $Co_{3-x}Fe_xSn_2S_2$ (x = 0–1.0) Obtained with High Pressure Synthesis, Journal of the Physical Society of Japan 84 (2015) 044705.
[79] J. Shen, Q. Zeng, S. Zhang, H. Sun, Q. Yao, X. Xi, W. Wang, G. Wu, B. Shen, Q. Liu, E. Liu, 33% Giant Anomalous Hall Current Driven by Both Intrinsic and Extrinsic Contributions in Magnetic Weyl Semimetal $Co_3Sn_2S_2$, Advanced Functional Materials 30 (2020) 2000830.
[80] G.S. Thakur, P. Vir, S.N. Guin, C. Shekhar, R. Weihrich, Y. Sun, N. Kumar, C. Felser, Intrinsic Anomalous Hall Effect in Ni-Substituted Magnetic Weyl Semimetal $Co_3Sn_2S_2$, Chem. Mat. 32 (2020) 1612-1617.
[81] H. Ebert, D. Ködderitzsch, J. Minár, Calculating condensed matter properties using the KKR-Green's function method—recent developments and applications, Reports on Progress in Physics 74 (2011) 096501.
[82] J.P. Perdew, K. Burke, M. Ernzerhof, Generalized Gradient Approximation Made Simple, Physical Review Letters 77 (1996) 3865-3868.
[83] D. Ködderitzsch, H. Ebert, D.A. Rowlands, A. Ernst, Relativistic formulation of the Korringa–Kohn–Rostoker nonlocal coherent-potential approximation, New Journal of Physics 9 (2007) 81-81.
[84] J. Minár, L. Chioncel, A. Perlov, H. Ebert, M.I. Katsnelson, A.I. Lichtenstein, Multiple-scattering formalism for correlated systems: A KKR-DMFT approach, Physical Review B 72 (2005) 045125.

[85] F. Pielnhofer, A.S. Tragl, J. Rothballer, R. Weihrich, In Search for Novel $Sn_2Co_3S_2$-based Half-metal Ferromagnets, Zeitschrift für Naturforschung B 69 (2014) 55-61.
[86] H.C. Wu, P.J. Sun, D.J. Hsieh, H.J. Chen, D.C. Kakarla, L.Z. Deng, C.W. Chu, H.D. Yang, Observation of skyrmion-like magnetism in magnetic Weyl semimetal $Co_3Sn_2S_2$, Materials Today Physics 12 (2020) 100189.
[87] J. Shen, Q. Zeng, S. Zhang, W. Tong, L. Ling, C. Xi, Z. Wang, E. Liu, W. Wang, G. Wu, B. Shen, On the anisotropies of magnetization and electronic transport of magnetic Weyl semimetal $Co_3Sn_2S_2$, Appl. Phys. Lett. 115 (2019) 212403.
[88] M.A. Kassem, Y. Tabata, T. Waki, H. Nakamura, Low-field anomalous magnetic phase in the kagome-lattice shandite $Co_3Sn_2S_2$, Physical Review B 96 (2017) 014429.
[89] J. Hu, X. Kan, Z. Chen, G. Zheng, Y. Ma, The magnetic, thermal transport properties, magnetothermal effect and critical behavior of Co3Sn2S2 single crystal, Journal of the American Ceramic Society n/a (2021).
[90] Z. Guguchia, J.A.T. Verezhak, D.J. Gawryluk, S.S. Tsirkin, J.X. Yin, I. Belopolski, H. Zhou, G. Simutis, S.S. Zhang, T.A. Cochran, G. Chang, E. Pomjakushina, L. Keller, Z. Skrzeczkowska, Q. Wang, H.C. Lei, R. Khasanov, A. Amato, S. Jia, T. Neupert, H. Luetkens, M.Z. Hasan, Tunable anomalous Hall conductivity through volume-wise magnetic competition in a topological kagome magnet, Nature Communications 11 (2020) 559.
[91] D. Khadka, T.R. Thapaliya, S.H. Parra, X. Han, J. Wen, R.F. Need, P. Khanal, W. Wang, J. Zang, J.M. Kikkawa, L. Wu, S.X. Huang, Kondo physics in antiferromagnetic Weyl semimetal $Mn_{3+x}Sn_{1-x}$ films, Science Advances 6 (2020) eabc1977.
[92] A.C. Hewson, The Kondo Problem to Heavy Fermions, Cambridge University Press, Cambridge, 1993.
[93] S.Y. Yang, S.S.P. Parkin, I. Mertig, V.Z. Han, In Search of Extraordinary Hall Effects in Topological Semimetals, Martin-Luther-Universität Halle-Wittenberg2020.
[94] K. Ueda, Effect of magnetic field on spin fluctuations in weakly ferromagnetic metals, Solid State Communications 19 (1976) 965-968.
[95] M. Tanaka, Y. Fujishiro, M. Mogi, Y. Kaneko, T. Yokosawa, N. Kanazawa, S. Minami, T. Koretsune, R. Arita, S. Tarucha, M. Yamamoto, Y. Tokura, Topological Kagome Magnet $Co_3Sn_2S_2$ Thin Flakes with High Electron Mobility and Large Anomalous Hall Effect, Nano Letters 20 (2020) 7476-7481.
[96] K. Geishendorf, R. Schlitz, P. Vir, C. Shekhar, C. Felser, K. Nielsch, S.T.B. Goennenwein, A. Thomas, Magnetoresistance and anomalous Hall effect in micro-ribbons of the magnetic Weyl semimetal $Co_3Sn_2S_2$, Appl. Phys. Lett. 114 (2019) 5.
[97] A.A. Burkov, Topological semimetals, Nature Materials 15 (2016) 1145-1148.
[98] Shama, R.K. Gopal, Y. Singh, Observation of planar Hall effect in the ferromagnetic Weyl semimetal $Co_3Sn_2S_2$, J. Magn. Magn. Mater. 502 (2020) 5.
[99] A.E. Musikhin, M.A. Bespyatov, V.N. Shlegel, O.E. Safonova, Low-temperature properties of $BaWO_4$ based on experimental heat capacity in the range 5.7–304 K, Journal of Alloys and Compounds 802 (2019) 235-243.
[100] E.S.R. Gopal, Specific Heats at Low Temperatures, Springer New York, NY1966.
[101] W. Schnelle, A. Leithe-Jasper, H. Rosner, F.M. Schappacher, R. Pöttgen, F. Pielnhofer, R. Weihrich, Ferromagnetic ordering and half-metallic state of $Sn_2Co_3S_2$ with the shandite-type structure, Physical Review B 88 (2013) 144404.

[102] C. Li, Z. Wang, 9 - Computational modelling and ab initio calculations in MAX phases – I, in: I.M. Low (Ed.), Advances in Science and Technology of $M_{n+1}AX_n$ Phases, Woodhead Publishing2012, pp. 197-222.
[103] W. Ma, X. Zhang, K. Takahashi, Electrical properties and reduced Debye temperature of polycrystalline thin gold films, Journal of Physics D: Applied Physics 43 (2010) 465301.
[104] M.I. Naher, S.H. Naqib, An ab-initio study on structural, elastic, electronic, bonding, thermal, and optical properties of topological Weyl semimetal TaX (X = P, As), Scientific Reports 11 (2021) 5592.
[105] A. Saadi, L.e.H. Omari, A. Boudali, Sn replacement influence on magnetic, electronic, thermodynamic, thermoelectric and transport properties in shandite compounds of $Co_3In_{2-x}Sn_xS_2$, The European Physical Journal B 93 (2020) 180.
[106] K. Geishendorf, P. Vir, C. Shekhar, C. Felser, J.I. Facio, J. van den Brink, K. Nielsch, A. Thomas, S.T.B. Goennenwein, Signatures of the Magnetic Entropy in the Thermopower Signals in Nanoribbons of the Magnetic Weyl Semimetal $Co_3Sn_2S_2$, Nano Letters 20 (2020) 300-305.
[107] B. Skinner, L. Fu, Large, nonsaturating thermopower in a quantizing magnetic field, Science Advances 4 (2018) eaat2621.
[108] R. Lundgren, P. Laurell, G.A. Fiete, Thermoelectric properties of Weyl and Dirac semimetals, Physical Review B 90 (2014) 165115.
[109] G. Sharma, P. Goswami, S. Tewari, Nernst and magnetothermal conductivity in a lattice model of Weyl fermions, Physical Review B 93 (2016) 035116.
[110] P. Sun, K.R. Kumar, M. Lyu, Z. Wang, J. Xiang, W. Zhang, Generic Seebeck effect from spin entropy, The Innovation 2 (2021) 100101.
[111] T. Takabatake, E. Matsuoka, S. Narazu, K. Hayashi, S. Morimoto, T. Sasakawa, K. Umeo, M. Sera, Roles of spin fluctuations and rattling in magnetic and thermoelectric properties of AT4Sb12 (A=Ca, Sr, Ba, La; T=Fe, Ru, Os), Physica B: Condensed Matter 383 (2006) 93-102.
[112] N. Tsujii, A. Nishide, J. Hayakawa, T. Mori, Observation of enhanced thermopower due to spin fluctuation in weak itinerant ferromagnet, Science Advances 5 (2019) eaat5935.
[113] K. Behnia, Conductivity, Thermal, in: F. Bassani, G.L. Liedl, P. Wyder (Eds.), Encyclopedia of Condensed Matter Physics, Elsevier, Oxford, 2005, pp. 225-229.
[114] M. Kanagaraj, J. Ning, L. He, Topological Co3Sn2S2 magnetic Weyl semimetal: From fundamental understanding to diverse fields of study, Reviews in Physics 8 (2022) 100072.
[115] D. Ködderitzsch, S. Lowitzer, J.B. Staunton, H. Ebert, Electronic and transport properties of disordered transition-metal alloys, physica status solidi (b) 248 (2011) 2248-2265.
[116] O. Šipr, S. Wimmer, S. Mankovsky, H. Ebert, Transport properties of doped permalloy via ab initio calculations: Effect of host disorder, Physical Review B 101 (2020) 085109.
[117] Y. Zhang, Z. Li, C. Uher, Low-temperature thermal properties of Fe-doped $Co_3Sn_2S_2$, Materials Today Communications 34 (2023) 105100.
[118] Y. Zhang, C. Uher, Magnetic and transport properties of Fe-doped Weyl semimetal $Co_3Sn_2S_2$ Journal of Alloys and Compounds 911 (2022) 165089.
[119] J.M. Daughton, GMR applications, J. Magn. Magn. Mater. 192 (1999) 334-342.
[120] H. Fang, M. Lyu, H. Su, J. Yuan, Y. Li, L. Xu, S. Liu, L. Wei, X. Liu, H. Yang, Q. Yao, M. Wang, Y. Guo, W. Shi, Y. Chen, E. Liu, Z. Liu, Record-high mobility and extreme magnetoresistance on kagome-lattice in compensated semimetal $Ni_3In_2S_2$, Science China Materials (2023).
[121] https://elk.sourceforge.io/.

[122] T. Zhang, T. Yilmaz, E. Vescovo, H.X. Li, R.G. Moore, H.N. Lee, H. Miao, S. Murakami, M.A. McGuire, Endless Dirac nodal lines in kagome-metal $Ni_3In_2S_2$, npj Computational Materials 8 (2022) 155.
[123] P.M.C. Rourke, S.R. Julian, Numerical extraction of de Haas–van Alphen frequencies from calculated band energies, Computer Physics Communications 183 (2012) 324-332.
[124] R. Weihrich, I. Anusca, M. Zabel, Halbantiperowskite: Zur Struktur der Shandite $M_{3/2}AS$ (M = Co, Ni; A = In, Sn) und ihren Typ-Antitypbeziehungen, Zeitschrift für anorganische und allgemeine Chemie 631 (2005) 1463-1470.
[125] N.W. Ashcroft, N.D. Mermin, Solid State Physics, Cengage Learning2011.
[126] R. Singha, A.K. Pariari, B. Satpati, P. Mandal, Large nonsaturating magnetoresistance and signature of nondegenerate Dirac nodes in ZrSiS, Proceedings of the National Academy of Sciences 114 (2017) 2468-2473.
[127] Y.L. Wang, L.R. Thoutam, Z.L. Xiao, J. Hu, S. Das, Z.Q. Mao, J. Wei, R. Divan, A. Luican-Mayer, G.W. Crabtree, W.K. Kwok, Origin of the turn-on temperature behavior in WTe_2, Physical Review B 92 (2015) 180402.
[128] Q. Li, B. Wang, N. Tang, C. Li, E. Yi, B. Shen, D. Guo, D. Zhong, H. Wang, Signatures of Temperature-Driven Lifshitz Transition in Semimetal Hafnium Ditelluride, Chinese Physics Letters 40 (2023) 067101.
[129] E. Mun, H. Ko, G.J. Miller, G.D. Samolyuk, S.L. Bud'ko, P.C. Canfield, Magnetic field effects on transport properties of $PtSn_4$, Physical Review B 85 (2012) 035135.
[130] K. Wang, D. Graf, L. Li, L. Wang, C. Petrovic, Anisotropic giant magnetoresistance in $NbSb_2$, Scientific Reports 4 (2014) 7328.
[131] Y. Kopelevich, J.C.M. Pantoja, R.R. da Silva, S. Moehlecke, Universal magnetic-field-driven metal-insulator-metal transformations in graphite and bismuth, Physical Review B 73 (2006) 165128.
[132] Y. Kopelevich, J.H.S. Torres, R.R. da Silva, F. Mrowka, H. Kempa, P. Esquinazi, Reentrant Metallic Behavior of Graphite in the Quantum Limit, Physical Review Letters 90 (2003) 156402.
[133] J. Xu, F. Han, T.-T. Wang, L.R. Thoutam, S.E. Pate, M. Li, X. Zhang, Y.-L. Wang, R. Fotovat, U. Welp, X. Zhou, W.-K. Kwok, D.Y. Chung, M.G. Kanatzidis, Z.-L. Xiao, Extended Kohler's Rule of Magnetoresistance, Physical Review X 11 (2021) 041029.
[134] Q. Chen, Z. Lou, S. Zhang, B. Xu, Y. Zhou, H. Chen, S. Chen, J. Du, H. Wang, J. Yang, Q. Wu, O.V. Yazyev, M. Fang, Large magnetoresistance and nonzero Berry phase in the nodal-line semimetal MoO_2, Physical Review B 102 (2020) 165133.
[135] Y. Zhou, Z. Lou, S. Zhang, H. Chen, Q. Chen, B. Xu, J. Du, J. Yang, H. Wang, C. Xi, L. Pi, Q. Wu, O.V. Yazyev, M. Fang, Linear and quadratic magnetoresistance in the semimetal SiP_2, Physical Review B 102 (2020) 115145.
[136] Y. Zhang, Z. Li, K.-W. Chen, L. Li, C. Uher, Extremely large magnetoresistance and quantum oscillations in semimetal Ni3In2S2, Materials Today Physics 40 (2024) 101318.
[137] A. Chakraborty, J. Fujii, C.-N. Kuo, C.S. Lue, A. Politano, I. Vobornik, A. Agarwal, Observation of highly anisotropic bulk dispersion and spin-polarized topological surface states in $CoTe_2$, Physical Review B 107 (2023) 085406.
[138] T. Nguyen, N. Aryal, B.K. Pokharel, L. Harnagea, D. Mierstchin, D. Popović, D.E. Graf, K. Shrestha, Fermiology of the Dirac type-II semimetal candidates (Ni,Zr)Te_2 using de Haas--van Alphen oscillations, Physical Review B 106 (2022) 075154.

[139] F. Fei, X. Bo, R. Wang, B. Wu, J. Jiang, D. Fu, M. Gao, H. Zheng, Y. Chen, X. Wang, H. Bu, F. Song, X. Wan, B. Wang, G. Wang, Nontrivial Berry phase and type-II Dirac transport in the layered material $PdTe_2$, Physical Review B 96 (2017) 041201.
[140] C. Xu, B. Li, W. Jiao, W. Zhou, B. Qian, R. Sankar, N.D. Zhigadlo, Y. Qi, D. Qian, F.-C. Chou, X. Xu, Topological Type-II Dirac Fermions Approaching the Fermi Level in a Transition Metal Dichalcogenide $NiTe_2$, Chem. Mat. 30 (2018) 4823-4830.
[141] B. Ghosh, D. Mondal, C.-N. Kuo, C.S. Lue, J. Nayak, J. Fujii, I. Vobornik, A. Politano, A. Agarwal, Observation of bulk states and spin-polarized topological surface states in transition metal dichalcogenide Dirac semimetal candidate $NiTe_2$, Physical Review B 100 (2019) 195134.
[142] T. Liang, Q. Gibson, M.N. Ali, M. Liu, R.J. Cava, N.P. Ong, Ultrahigh mobility and giant magnetoresistance in the Dirac semimetal Cd_3As_2, Nature Materials 14 (2015) 280-284.
[143] W. Zheng, R. Schönemann, S. Mozaffari, Y.-C. Chiu, Z.B. Goraum, N. Aryal, E. Manousakis, T.M. Siegrist, K. Wei, L. Balicas, Bulk Fermi surfaces of the Dirac type-II semimetallic candidate $NiTe_2$, Physical Review B 102 (2020) 125103.
[144] C. Fu, S.N. Guin, T. Scaffidi, Y. Sun, R. Saha, S.J. Watzman, A.K. Srivastava, G. Li, W. Schnelle, S.S.P. Parkin, C. Felser, J. Gooth, Largely Suppressed Magneto-Thermal Conductivity and Enhanced Magneto-Thermoelectric Properties in $PtSn_4$, Research 2020 (2020) 4643507.
[145] R. Ocaña, P. Esquinazi, Thermal conductivity tensor in $YBa_2Cu_3O_{7-x}$: Effects of a planar magnetic field, Physical Review B 66 (2002) 064525.
[146] J. Gooth, F. Menges, N. Kumar, V. Süβ, C. Shekhar, Y. Sun, U. Drechsler, R. Zierold, C. Felser, B. Gotsmann, Thermal and electrical signatures of a hydrodynamic electron fluid in tungsten diphosphide, Nature Communications 9 (2018) 4093.
[147] P. Li, P. Qiu, Q. Xu, J. Luo, Y. Xiong, J. Xiao, N. Aryal, Q. Li, L. Chen, X. Shi, Colossal Nernst power factor in topological semimetal $NbSb_2$, Nature Communications 13 (2022) 7612.
[148] S.N. Guin, P. Vir, Y. Zhang, N. Kumar, S.J. Watzman, C. Fu, E. Liu, K. Manna, W. Schnelle, J. Gooth, C. Shekhar, Y. Sun, C. Felser, Zero-Field Nernst Effect in a Ferromagnetic Kagome-Lattice Weyl-Semimetal $Co_3Sn_2S_2$, Advanced Materials 31 (2019) 1806622.
[149] Y. Chen, Y. Zhang, C. Uher, P.F.P. Poudeu, Carrier Mobility Modulation in Cu_2Se Composites Using Coherent Cu_4TiSe_4 Inclusions Leads to Enhanced Thermoelectric Performance, ACS Applied Materials & Interfaces 14 (2022) 56817-56826.